Pressure Development due to Viscous Fluid Flow through a Converging Gap

By

Ahmed Imhamed BSc. Eng (Chemical)

A Thesis Submitted In Fulfillment of the Requirements for the Degree of Master of Engineering (M.Eng)

School of Mechanical and Manufacturing Engineering

Faculty of Engineering and Computing

Dublin City University

2004

DECLARATION

I hereby certify that this material, which I now submit for assessment on the program of study leading to the award of Master of engineering is my own work and has not been taken from the work of others save and to the extend that such work has been cited and acknowledged within the text of my work.

Ahmed Imhamed
ID No: 51172950
Date: 16-09-2004

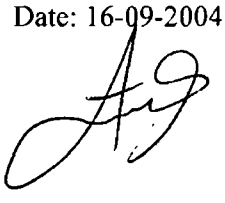

To my beloved Parents

Acknowledgements

First of all I wish to express my heartiest gratitude and profound indebt to my supervisor *Prof. M. S. J. Hashmi*, who kept me patiently, focused on my work, and made my deep steps into the beautiful field of fluid mechanics and Materials behaviour study. My researches under his thoughtful guidance have been extremely successful and personally satisfying. I will always be deeply grateful to him, who had so much importance for developing my knowledge in this field.

I also would like to offer my honest appreciation to the staff in School of Mechanical& Manufacturing Engineering department, *especially Mr. Keith Hickey, Mr. Michael Tyrrell, Mr. Alan Meehan, Mr. Michael May* and *Mr. Liam Domican* for their time, effort and cooperative support. Special thanks to *Ms Sarah Jane Shannon* and *Ms Kathleen Donohoe* for their co-operation.

I am indebted a lot to all my dear friends for their advice and support that assisted me to keep up my spirits, my sincere thanks to all of them. My special appreciation goes to my dear friends *Dr. Amr Arisha, Mr. Mohamed Krer and Mr. Tariq Mujber* for their caring and kindness advices. I also can not forget any of my companions in Dublin City University who were always supportive.
Individual thank to *Ms Christine Magee* for her admirable notices and truthful help.

Many thanks to my family; my beloved mother, my father, my sisters and brothers for their generous love and support. My apologize to them for the enormous load I made them bear over the years of my study. Without their love and support, this work would not have taken place.

Abstract

The behaviour of fluid flow in industrial processes is essential for numerous applications and there have been vast amount of work on the hydrodynamic pressure generated due to the flow of viscous fluid. One major manifestation of hydrodynamic pressure application is the wire coating/drawing process, where the wire is pulled through a unit either conical or cylindrical bore filled with a polymer melt that gives rise to the hydrodynamic pressure inside the unit. The hydrodynamic pressure distribution may change during the process due to various factors such as the pulling speed, process temperature, fluid viscosity, and geometrical shape of the unit (die). This work presents the process of designing a new plasto-hydrodynamic pressure die based on a tapered-stepped-parallel bore shape; the device consists of a fixed hollow outer cylinder and an inner rotating shaft, where the hollow cylinder represents a pressure chamber and the rotating shaft represents the moving surface of the wire. The geometrical shape of the bore is provided by different shaped inserts to set various gap ratios, and the complex geometry of the gap between the shaft and the pressure chamber is filled with viscous fluid materials. The device allows the possibility of determining changes in the hydrodynamic pressure as the shaft speed is altered while different fluid viscosity during the process is considered.

A number of experimental procedures and methods have been carried out to determine the effects of various shaft speeds by using Glycerine at 1 to18 °C and two different types of silicone oil fluids at 1 to 25 °C on the hydrodynamic pressure and shear rate. Viscosities of the viscous fluids were obtained at atmospheric pressure by using a Cone-plate Brookfield viscometer at low shear rate ranges.

Moreover, Computational fluid dynamics (CFD) was used to develop and analyze computational simulation models that demonstrate the pressure units, which studies the drawing process involving viscous fluids in a rotating system. A finite volume technique was used to observe the change in fluid viscosity during the process based on non-Newtonian characteristics at high shear rate ranges. The maximum shaft speed used in these models was $1.5 m.sec^{-1}$. Results from experimental and Computational models were presented graphically and discussed.

Contents

List of figures

CHAPTER ONE

CHPTER TWO

CHPTER THREE

CHAPTER FOUR

APPENDIX

List of tables

Chapter one

Introduction and literature review

1.1. Introduction

1.1.1 Conception of Hydrodynamic Pressure

Traditionally, hydrodynamic phenomenon was defined by the Rheological society as means of fluid dynamics under certain flow condition. It can be clarified by considering two surfaces, one fixed and the other moves relative to the fixed one. The gap between the two surfaces is filled with a viscous fluid. The action of the moving surface gives rise to the pressure in the fluid film. This observable fact is known as a hydrodynamic pressure. A general circumstance is when the fluid flows through a converging gap as a journal bearing (ball and roller bearings), where the mechanism of moving surface drags the viscous fluid through the gap formed between it and the fixed surface and the relative motion between the two surfaces gives rise to the pressure.

The magnitudes of the developed hydrodynamic pressure are dependent on various parameters, such as the geometrical shape of the surfaces, the relative speed of the movement as well as the viscosity of the fluid [1].

In general, the developed pressure is not so high if the fluid used is an oil, but it grows to be many times greater if the fluid is polymer solution. Accordingly, studying the growth of the hydrodynamic pressure in manufacturing operations such as plastic processing, mineral processing and food industries could be a noteworthy design factor, which may possibly be a beneficial cause to study the behaviour of either polymer solutions or viscous fluids in rheological rotating device to determine their properties at higher pressure rather than atmospheric pressure, as well as to employ their act in drawing and coating technique of wires and strips process.

1.1.2 Rheology

Rheology describes the scientific study of fluid flow behaviour and the critical study of elasticity, which is of particular importance for polymer processing and solid/ fluid mixtures. [2]. Word of rheology originates from the Greek word "rhein" which means "to flow", and it was officially coined in the late 1920s [3], and the express development of the subject began 20 years later, when the American Society of rheology was founded. The first official meeting of the Society of Rheology was held at the National Bureau of Standards on December 19, 1929 at which a formal committee was appointed on definitions and action was taken for securing an improved absolute viscosity standard; the journal of Rheology was also started as a quarterly. The name "rheology" was proposed to describe the flow and deformation of all forms of matter" by E.C. Bingham and M. Reiner; Heraclitus quote "παντα ρει" or "everything flows" was taken to be the motto of the subject [4].

The logic of rheology includes typical fluid mechanics and elasticity, which treat the flow of Newtonian fluids such as water, and small deformations of solids materials, such as wood and steel. Applying the special term of "rheology" for these cases alone is not justified, although they have been widely considered for more than 170 years and is an appreciative part of the program in most academic research.

The meaning of Rheology generally, refers to the flow and deformation of non-classical materials such as lubricants, asphalt, rubber, molten plastics, polymer solutions, slurries and pastes, electro-rheological fluids, blood, muscle, composites, soils, and paints. These materials can display different and unusual rheological properties that classical fluid mechanics and elasticity cannot describe.

Rheological studies involve activities and understanding from chemical and mechanical engineering, materials science, engineering mechanics, chemistry, mathematics, computer science, electronics, biophysics, physics, and medicine among others. The branch of rheology nature is invented from the variety of materials investigated and so many questions that need to be answered.

In ordinary mechanics, material properties are determined if viscosity or elastic modulus are given; the basic constitutive equations leading the behaviour of each small material component are known. Supplementary investigation often involves these equations, with the momentum conservation equation, to increasingly complicated flows or deformations. Nevertheless, the constitutive equations for most materials are unknown, and normally involve unknown functions; the form of the equations for visco-elastic materials is very different from the classical forms, which need to unite continuum mechanics with molecular theory and analyze the predictions with measurements from various flows or deformations. The molecular theory requires statistical modelling with computer analysis. The measurements require instruments for determining nonlinear viscoelastic properties, stress distributions and elastic recoil.

The rheological properties of materials are essentially important, whether for molten plastics, polymer solutions or viscous fluids, understanding these properties develop the optimization in processing technology.

Nowadays, the rheology of polymer is the widest and most effective research field in rheological science. Significant improvement has been made in developing special equipment for testing theoretical predictions in the laboratory to solve more complicated flow problems to assist the design of polymer processing equipment [4]. Therefore, a new term has been invented based on the rheological instruments, which known as a Rheometry. The word rheometry is defined as one of the mainly significant analytical services supplied through impact analytical, as well as the physical and mechanical characterization of materials. Typically, there are two types of rheometers used in industrial labs; Capillary viscometer and Rotational viscometer. The Capillary viscometer has been in use for along time; in fact, the earliest attempts to measure the flow properties of fluids were done mainly with the principles of Capillary viscometry.

The main concentration activity of rheometry focuses on the area of polymeric materials (plastics, rubbers) and polymer composites, as well as testing a large variety of materials, which include ceramics, metals, organic and inorganic fibres,

and pharmaceuticals [5]. Accordingly, rheology involves a proposes a remarkable number of possibilities on an advanced level relating to realistic purposes in a wide range of industrial applications which include processing of oil, paints, adhesives, plastics, rubber, textiles, paper and foodstuffs.

Many manufacturing applications dealing with rheology for various types of materials and fluids can be listed as following:

1. Pumping slurries - materials transport.
2. Thickening and de-watering of mineral slurries.
3. Filtration - more viscous, less speed.
4. Forming materials e.g. brick & ceramic products.
5. Paint manufacture, e.g. non-drip paints.
6. Reactions involving mineral slurries e.g. gold extraction.
7. Food chemistry and manufacture - texture of ice-cream, pasta, desserts and processed meats.
8. Cosmetics chemistry.
9. Drilling mud for the petroleum industry.
10. Polymer chemistry - solutions and melts.
11. Soil chemistry e.g. effect of clay rheology on soil friability and structure
12. Plasto-hydrodynamic wire drawing and coating which requires a good surface finish of wire.

1.1.3 Polymers

Generally, there are numerous polymer types existing in a wide range of natural and synthetic polymers. Natural polymer types exist in plants and animals, which include starch, proteins, lignin, cellulose, collagen, silk and natural rubber. The Synthetic polymers types are usually derived from oil-based products which include polyethylene, nylon, epoxies, Phenolics, synthetic 'natural rubber' and styrene butadiene rubber. Polymers form the basis of plastics, rubbers, fibers, adhesives and paints.

The basic concepts of the polymer terms are: linear and network polymers, thermoplastic, thermosetting and cross-linked polymers; amorphous and incompletely crystalline conditions; molecular mobility in the rubbery and glassy states. These significant terms could explain the general behaviour of various polymer types and make a distinction for various polymer properties as well as the different properties of variants of a given polymer types; also provide a foundation to recognize the relations between polymer properties and manufacturing processing [6].

1.1.4 Manufacturing Processes involving Polymers

Normally, Polymers are organic materials which are lightweight, and have good thermal and electrical insulator. In addition, they present good corrosion and chemical resistance. They could be involved either with supplementary materials or by themselves to raise their mechanical properties. However, polymers are used to produce lightweight, corrosion-resistant materials of low to medium strength, electrical insulation and insulators, thermal insulation, acoustic foam insulation, flexible packaging foam and packing materials, adhesives, coatings, and replacement parts for automotive applications such as fenders and panels. With suitable additional materials, their properties could be enhanced to equal or exceed to other materials.

Several common processes are used to produce many polymer products such as; simple casting, blow moulding, compression moulding, transfer moulding, injection moulding, extrusion, vacuum forming, cold forming, filament winding, calendaring, and foaming.. Table 1.1 shows several of common polymers and their characteristics which are used in some manufacturing applications [7]

Table 1. 1: Common polymers characteristics in manufacturing applications

Common Polymer	Characteristics
Acrylonitrile-Butadiene-Stryene	Lightweight, good strength, excellent toughness
Acrylic	Excellent optical quality, high impact,

	flexural, tensile and dielectric strengths
Cellulose acetate	Good insulator, easily formed, high moisture absorption, low chemical resistance
Cellulose acetate butyrate	Similar to cellulose acetate, but withstands more severe conditions
Epoxies	Good toughness, elasticity, chemical resistance and dimensional stability; used in coatings, adhesive and cements, electrical components, and tooling
Ethyl cellulose	High electrical resistance, high impact strength, remains propertied at low temperatures, low tear strength
Fluorocarbons	Inert to most chemicals, high temperature resistance, low friction coefficient: Teflon used for self-lubricating products and non-stick coatings
Melamine	Excellent resistance to heat, water, and chemicals, excellent arc resistance; used in tableware and to treat water-repellant paper and cloth
Phenolics	Hard, relatively strong, inexpensive, easily-formed, generally opaque; wide variety of variable shapes and uses
Polycarbonates	High strength and toughness; used in safety glasses and shields
Polyethylene	High toughness, high electrical resistance; used in bottles, caps, unbreakable utensils, and wire insulation
Polypropylene	Lightest weight, used in many of the same applications as polyethylene, but is harder
Polystyrene	High dimensional stability, low moisture absorption. Excellent dielectric. Burns readily, low resistance to chemicals; used for the familiar beads and insulation
Silicone	Heat-resistant, low moisture absorption, high dielectric strength; used in caulks, sealants, and adhesives
Urea Formaldehyde	Similar to Phenolics, but used in interior applications
Vinyl	Tear-resistant, ages well, good dimensional stability, good moisture resistance; used in wall and floor

1.1.5 Rheology of polymer melt

1.1.5.1 Preface

The flow of fluid occurs when the molecules pass each other. A simple flow is dependent on the mobility of chains in the molecules and their force while holding the molecules together. Most current rheological studies are concerned directly with polymer processes because they exhibit such unusual, interesting, and difficult-to-describe behaviour. The simple and usual linear engineering models are, "Newton's law for flow" and "Hook's law for elasticity". Not only are the elastic and viscous properties of polymer melts and solutions usually nonlinear, but also they show a combination of viscous and elastic response [8]. The flow characteristics of the fluid as a polymer melt and viscous fluid are affected by some factors, which are described below in relation with this work.

1.1.5.2 Viscosity

One of the most important physical properties for many fluid products is viscosity, which includes both liquids and gases. The viscosity of material expresses its resistance to flow under a mechanical stress. It is defined quantitatively in terms of two basic parameters, the shear stress and shear rate [8], while the fundamental concept of viscosity is the same for liquids and gases, changes in temperature and pressure affect the viscosity of liquids and gases in different ways.

Viscosity has an essential function in various engineering calculations because both mass transfer and fluid flow are based on this property.

Physical systems and applications such as flow of fluids, whether flow in porous media or in wells or pipes, the flow of blood, lubrication of engine parts, the dynamics of rain drops, volcanic eruptions, planetary and stellar magnetic field generation are controlled to some degree by fluid viscosity. The viscosity of a fluid is very important because it determines the settling rates of particles within the solution during crystallization processes, and heat transfer rates in heat exchange

equipment required for heating or cooling the solution in many processes. Not only in crystallization but also in filtration and diffusion processes viscosity is fundamental. The measurements of viscosity have extensive sensible importance in the field of lubrication; the change of viscosity with pressure is a critical parameter in determining the metal-metal contact [9]. Understanding on viscosity of polymer solutions is extremely important for many processes involving polymer formation and solution processing. The viscosity of polymer solutions depends on the nature of the polymer and the solvent, concentration of the polymer, molecular weight and the molecular weight distribution of the polymer, temperature, pressure and the shear rate.

Temperature and pressure are known to be two of the most powerful variables in the viscosity of polymer melt. It has long been realized in practice that the flow behaviour of molten polymer is vastly dependent on these two variables.

1.1.5.3 Stress strain dependence viscosity

In general; the plot of shear stress-shear rate relation for Newtonian fluids is a straight line at a given temperature when it is under shear stress condition. The plot shows a straight line with a constant slope as shown in Figure 1.1. The viscosity of the Newtonian fluid is independent of shear rate and depends only on temperature and, to a much lesser extent, on pressure. Figure 1.2 shows the impact of shear rate on viscosity for Newtonian fluids.

A shear rate independent viscosity is a property of only some liquids. Naturally, all gases are Newtonian, the familiar liquids such as water and glycerine are also Newtonian as are low-molecular-weight liquids and solution of low molecular weight substances in liquids [10,11]. On the other hand, high-molecular-weight liquids including slurries, suspension and solutions of high-molecular-weight polymers in low-molecular-weight solvents are often non-Newtonian, in which the viscosity is a function of shear rate, where it changes while the shear rate altered. For the non-Newtonian shear thinning fluids as psuedoplastic fluids (Polymer solution), the viscosity decreases with the increase of the shear rate, whilst, for

shear thickening fluids, the shear rate- shear stress relation shows opposite rheological effect to shear thinning and it behaves as dilatants fluid [12].

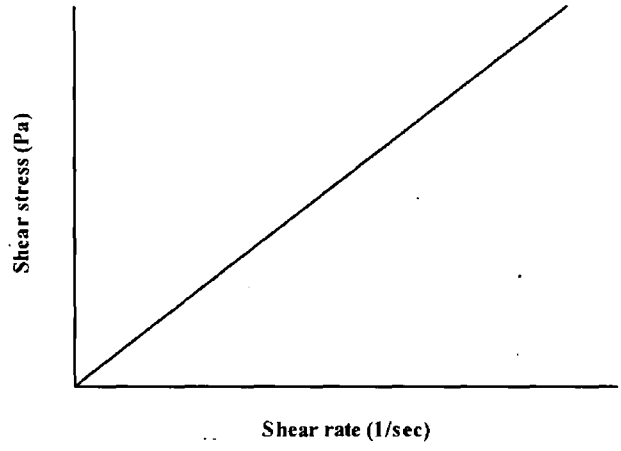

Figure 1. 1: Shear rate versus shear stress for Newtonian fluids

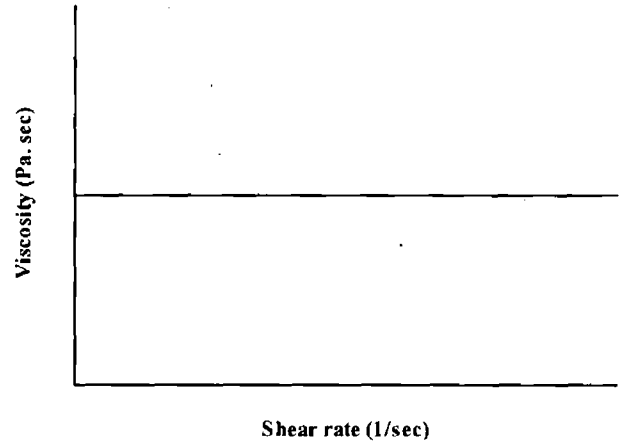

Figure 1. 2: Impact of shear rate on viscosity for Newtonian fluids

The relation between the viscosity and shear rate in a polymeric system that can be obtained over an enormously wide range of shear rates are shown in Figure 1.3 and 1.4. The figures illustrate constant values of viscosity at low and high shear-rate ranges which are sometimes referred to as upper and lower Newtonian regions, respectively. The profile of the curve in Figure 1.3 is typically for data of polymer

solutions. However, the experimental difficulties at lesser and greater shear rates often prevent measurements of upper and lower limiting values [13].

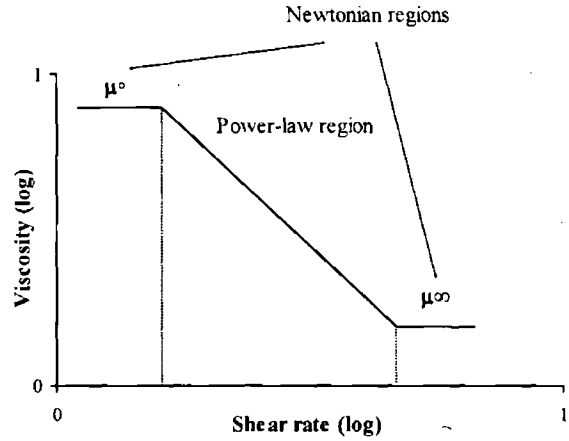

Figure 1. 3: Shear rate versus viscosity for polymeric system

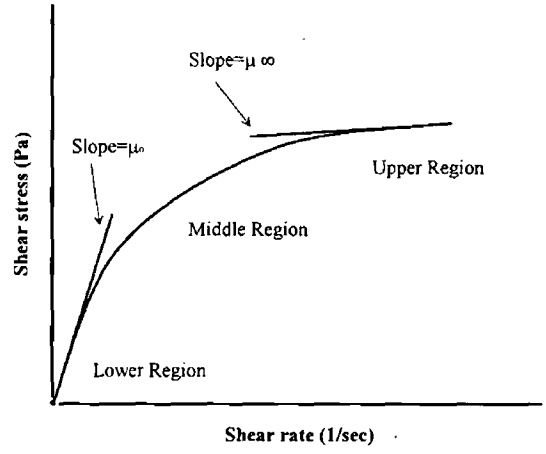

Figure 1. 4: Relation of shear rate versus shear stress for polymeric system

Conventionally, the observation of non-Newtonian fluid mechanics uses Newtonian fluid mechanics as a starting point in all cases. The viscosity is a decreasing function with temperature for the liquids, and in some cases the temperature dependency is extremely strong [10].

The range of viscosities for some familiar materials is shown in Table 1.2, where special instruments are required to evaluate the viscosity over this wide-range [14], as well the shear rate corresponding to numerous industrial processes could also vary over a wide range as shown in Table 1.3 [13].

Table 1. 2: Viscosity of some familiar materials at room temperature *[after Barnes et al]*

liquid	Approximate viscosity (Pa.sec)
Glass	10^{40}
Asphalt	10^{8}
Molten polymers	10^{3}
Heavy syrup	10^{2}
Honey	10^{1}
Glycerine	10^{0}
Olive oil	10^{-1}
Light oil	10^{-2}
Water	10^{-3}
Air	10^{-5}

Table 1. 3: Range of shear rates of some familiar materials in several industrial process applications

Process	Range of Shear rates(s^{-1})	Application
Sedimentation of fine powders in a suspending liquid	10^{-6}-10^{-4}	Medicines, paints, spices in salad dressing
Leveling due to surface tension	10^{-2}-10^{-1}	Frosting, paints, printing inks
Draining under gravity	10^{-1}-10^{1}	Painting, coating
Extrusion	10^{0}-10^{2}	Polymer melts, tooth paste, pasta, dough
Chewing and swallowing	10^{1}-10^{2}	Foods
Dip coating	10^{1}-10^{2}	Paints, confectionery
Mixing and stirring	10^{1}-10^{3}	Manufacturing liquids
Pipe flow	10^{0}-10^{3}	Pumping, food processing, blood flow
Spraying and brushing	10^{3}-10^{4}	Fuel atomization, painting

Rubbing	10^4-10^5	Application of creams and lotions to the skin
Injection mould gate	10^4-10^5	Polymer melts
Spraying	10^3-10^5	Spray drying, spray painting, fuel atomization
High speed coating	10^4-10^6	Paper
Lubrication	10^3-10^7	Bearing, Gasoline engines

In general, the relation of shear rate viscosity can be expressed by the simplest constitutive equation of Newtonian law [15].

$$\tau = \mu \dot{\gamma} \tag{1.1}$$

Where, τ is shear stress, μ is Newtonian viscosity and $\dot{\gamma}$ is the shear rate.
This equation takes another two forms to express the relation of shear stress-shear rate for different types of fluids; the first equation is the power law equation which is given by;

$$\tau = K\left(\frac{dU}{dy}\right)^n \tag{1.2}$$

where, τ is the shear stress, n is the power law index, K is the viscosity coefficient and $\left(\frac{dU}{dy}\right)$ is the shear rate. The power law index has different values, which equals to 1 for Newtonian fluids, less than 1 for psuedoplastic fluids and greater than 1 for dilatants fluids. That makes the equation applicable for the most common types of fluids.

The second form of the equation is an empirical equation which relates the shear stress with the shear rate, it was suggested by Rabinowitsch [16] in the form of;

$$\tau + K\tau^3 = \mu\left(\frac{dU}{dy}\right) \tag{1.3}$$

where τ is the shear stress, $\left(\frac{dU}{dy}\right)$ is the shear rate, K is the non-Newtonian factor, and μ is the polymer melt viscosity.

Based on these equations, a number of experimental works were carried out by Parvinmehr [17] by using different type of polymer melts and the relation of viscosity versus shear rate was obtained. The flow charts in Figure 1.5 and 1.6 show the effect of shear rate on viscosity for Alkathene WVG23 and Polypropylene KM61 respectively. These curves where obtained by extruding the polymer melt through an extrusion rheometer. The viscosity of the polymer melt can be obtained at any known shear rate by measuring the slop of the curve.

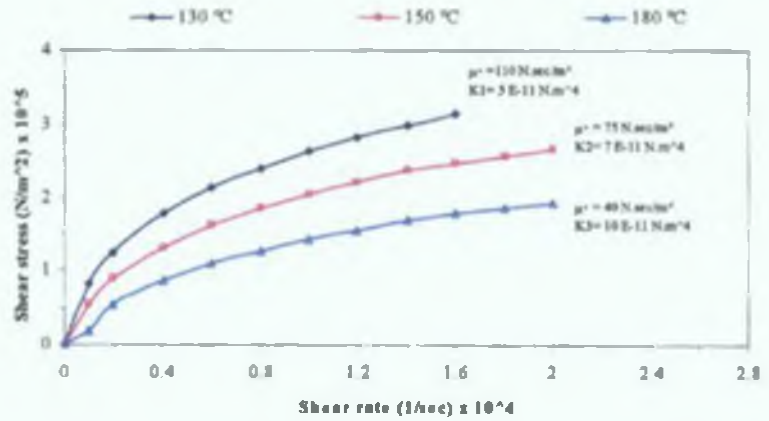

Figure 1. 5: Shear rate- shear stress relation for Alkathene WVG 23 *(after Parvinmehr, H)*

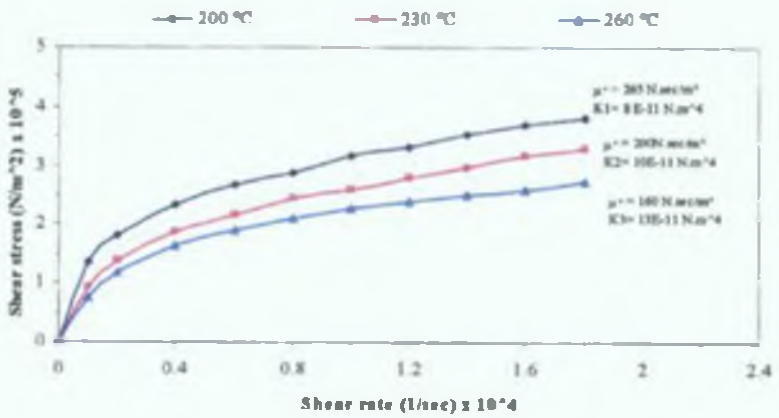

Figure 1. 6: Shear rate- shear stress relation for Polypropylene KM 61 *(after Parvinmehr, H)*

1.1.5.4 Temperature dependence viscosity

The relationship between the temperature and viscosity for Newtonian fluids may be expressed through Arrhenius type relationships in terms of flow activation energy.

$$\mu = Ae^{E/RT} \tag{1.4}$$

Or

$$\frac{\partial \ln \mu}{\partial (1/T)} = E/R \tag{1.5}$$

Where μ is the viscosity of the fluid, A is a constant, E is the activation energy, T is the absolute temperature, and R is the universal gas constant.

Generally, Polymer melt shows non-Newtonian performance except for very low shear rates [18]. A different form of equation is often used,

$$\mu = ae^{-bT} \tag{1.6}$$

Where a and b are constants.

The higher value of the activation energy represents the higher sensitivity of viscosity to temperature.

Many challenges have been made to find an essential explanation for the variation in temperature dependence of viscosity among various polymers. The theory of "free volume" is at present the most effective application to successfully describe the concept. The free volume theory in polymer science is well known. Generally, the free volume (f) can be considered as the volume of a given system at the temperature of study minus the volume of the same system at zero temperature, where the free volume is contributed by all the species present in the system [19].

The theory advises that, at temperature T_0 *(which suggested being about 52 °C below the glass transition temperature T_g)* there is no "free volume" between the molecules. This free volume is assumed to rise linearly with temperature that makes the fractional free volume have a value of (f_g) at glass transition temperature (T_g), The expansion coefficient α_f is defined as following;

$$f = f_g + \alpha_f (T - T_g) \tag{1.7}$$

Where f_g has the general value of 0.025 and α_f a general value of 4.8×10^{-4}. William et al. [20] have deduced from this that the viscosity μ of a polymer at temperature T may be associated to its viscosity μ_a at an arbitrary reference temperature T_a by the equation

$$\log \frac{\mu}{\mu_a} = -\frac{C_1^a (T - T_a)}{C_2^a + T - T_a} \tag{1.8}$$

If T_g represented as arbitrary temperature then the Equation (1.7) becomes;

$$\log \frac{\mu}{\mu_g} = -\frac{C_1^g (T - T_g)}{C_2^g + T - T_g} \tag{1.9}$$

where C_1^g and C_2^g proposed as general constants as following

$$C_1^g = \frac{1}{2.303 f_g} = 17.44$$

and

$$C_2^g = \frac{1}{2.303 C_1^g \alpha_f} = 51.6$$

These equations are known as the *WLF* equations. With an increase in temperature, the molecular arrangements in the polymer change to more random patterns; thus it

becomes easier for polymer to flow at higher temperature [21]. Figures 1.7a and 1.7b show the viscosity-temperature relation at zero shear rate for Alkathene and Polypropylene respectively, the figures do not represent the whole behaviour of polymer characteristics while viscosity is affected by pressure, shear rate and temperature. The results obtained by Parvinmehr [17] showed that the change in the temperature of the process affects the viscosity of the polymer melts, as Figure 1.8 and 1.9 illustrate.

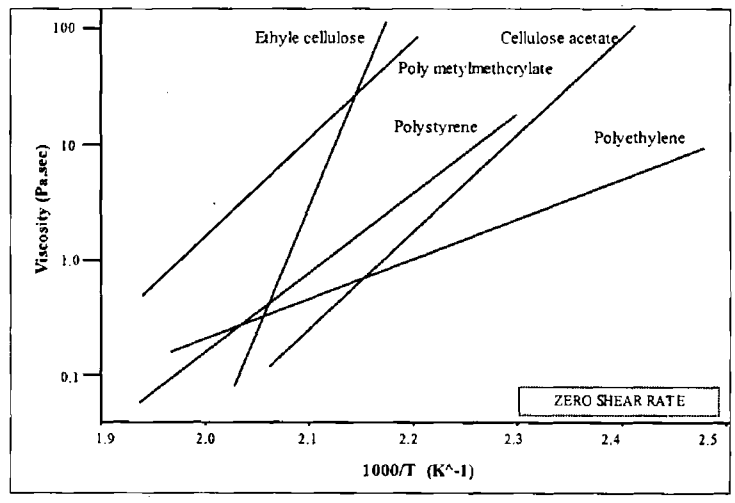

(a)

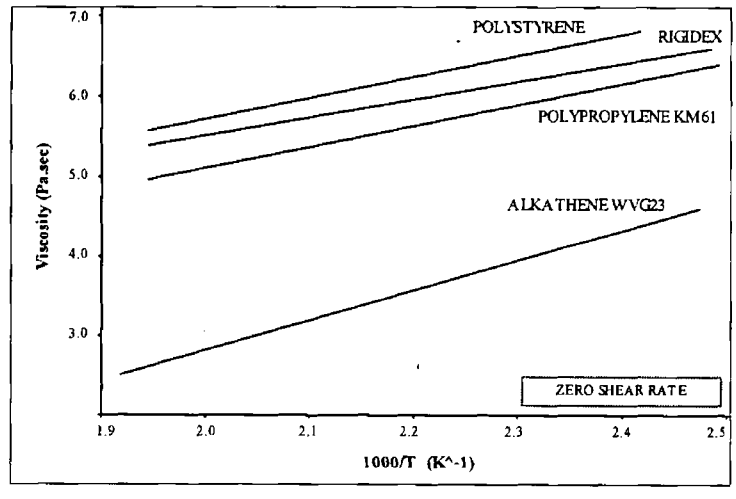

(b)

Figure 1. 7: Effect of temperature on viscosity for different types of polymers at zero shear rate

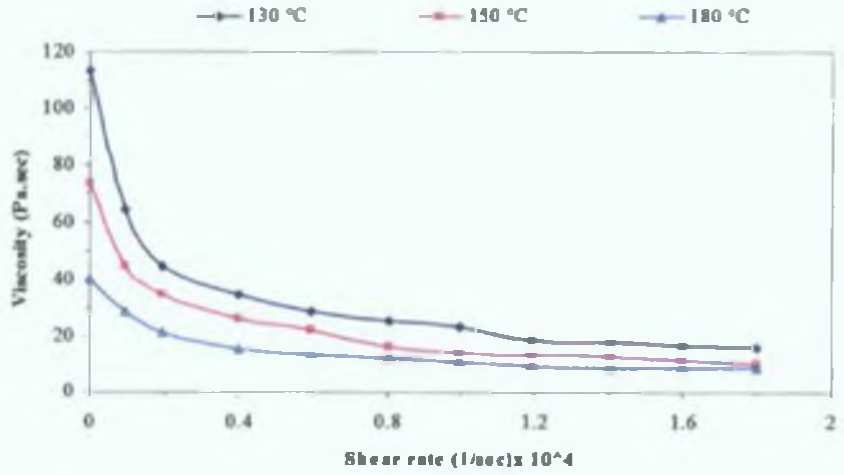

Figure 1. 8: Shear rate versus viscosity for Alkathene WVG 23 *(after Parvinmehr, H)*

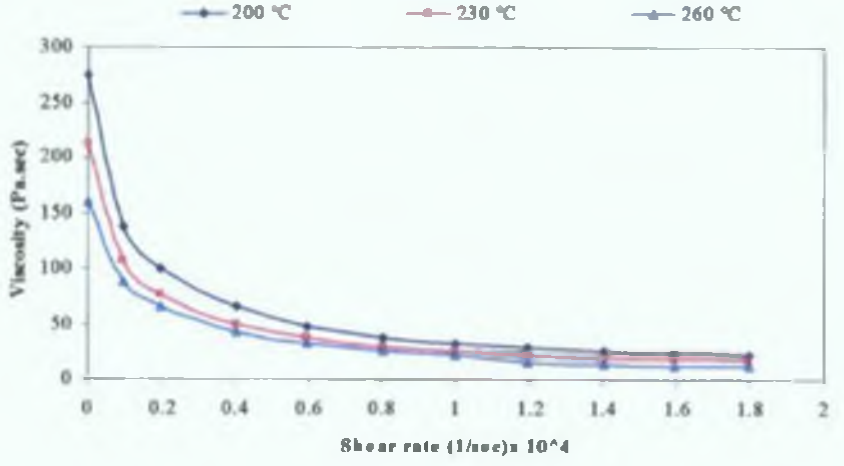

Figure 1. 9: Shear rate versus viscosity for Polypropylene KM 61 *(after Parvinmehr, H)*

1.1.5.5 Critical shear stress (CSS)

A very common situation by means of fluid flow involving polymer melt or polymer solution is known as *The Critical shear stress*, which is defined as the stress at which the flow consistencies of the polymer melt ceases to exist. A good

agreement was found by Rheological society which achieved that; certain flow defects are related to polymer melts at critical shear stress. The flows shown to take irregular behaviour of different forms such as; spiral, ripple, bamboo, zigzag or helix for various types of polymers.

The value of the critical stress depends mainly on the size and density of the polymer particles as well as on their shape, their packing, and the cohesive forces acting between particles [22].

Conventionally, three different terms have been used to describe this impact, known as *"Melt fracture"*, *"Elastic turbulence"* and *"Flow distortion"*. On the other hand, there is a common conformity in some points that can describe this phenomenon, as following:

1- The critical shear stress values were obtained at the range 0.1- 1.0 MN/m^2 for most polymers.
2- The critical shear stress is independent of the die length and diameter.
3- The critical shear stress does not diverge widely with the change in temperature.
4- A discontinuity in the viscosity shear stress profiles occurs.
5- The flow defects always take place when non-Newtonian fluids types are involved.
6- The critical shear stress was shown by cinematography method to take place in the die.

Many researchers considered this phenomenon in the polymeric systems; Benbow and lamb [23], who used a coloured polymer within a transparent die; they found that the slip condition occurs on the wall of the die when the shear stress reaches its critical amount. Additionally, they carried out more experiments by using two different types of die materials to study the effect of the change in die material on the critical shear stress. They employed brass and silver steel dies and

found that; the critical shear stress was affected by the materials type of the die when different flow characteristics were observed. Their results showed that, for brass die there was a change in the slope curve at the start of the flow deformation, while the silver steel die showed a smooth flow curve.

Additionally, more appreciated observations were achieved by Westover [24], who studied the slip condition for polymer melt on an ultra high molecular weight linear polyethylene integrating hydrostatic pressure, and found; the flow rate above the critical shear stress increased rather than decreased as for most of the polymers, as well the critical shear stress occurred at lower shear rate as the hydrostatic pressure upon the melt increased.

1.1.5.6 Pressure dependence viscosity

The wide-ranging viscosity of fluids is a physically powerful function of pressure. The effect of pressure on some rheometrical properties, such as normal-stress differences and extensional viscosity is not well known. The property of high pressures is involved in many industrial processes as the polymer industry, which includes processes such as injection moulding, which can involve pressures up to 100 MPa; the pressures generated in gears lubricants can often exceed 1 GPa; whilst oil-well drilling muds have to operate at depths where the pressure can reach 20 MPa [25]. Therefore, there is an obvious requirement to study the viscoelastic properties of industrial fluids and how it varies with pressure.

Studying the effect of pressure on the shear viscosity of polymer melts were initiated in the late 1950s by Maxwell and Jung [26], who investigated the effect of hydrostatic pressure on the apparent viscosity of high molecular weight polyethylene and polystyrene by using opposed-barrel capillary rheometer with length/diameter ratio of 20. It consists of two barrels in series separated by a die; two pistons acting in opposite directions are used to apply equal pressure to each barrel and pistons which causes the melt to flow through the die. There was consequently a pressure drop between the reservoirs, from which, with knowledge

of the capillary dimensions, the shear rate and shear stress may be calculated. They made no improvement for entrance effects, which were assumed to be negligible. The apparent viscosity of polyethylene increased as the mean pressure was increased from atmospheric to 168 MPa, whilst polystyrene showed a remarkable increase over the range 0-126 MPa. Following their work, a comprehensive study was undertaken later by Westover [27], who developed a capillary rheometer, based on Maxwell's proposal to study the effect of pressure on the rheology of polyethylene, which was capable for operating system at pressures up to 170 MPa with a large variety of temperatures. The same as the case of Maxwell's instrument, pressure drops were considered by calculating a force balance on the pistons. Through this technique, Westover measured the apparent viscosity of high- and low-density polyethylene over a respectable range of shear rates at numerous levels of main pressure between 14 MPa and 170 MPa. Furthermore, Westover measured the effect of pressure on entrance flow, and mentioned that, for a capillary die with the length/diameter ratio of 20, this effect could be 25-50% of the total pressure loss, depending on die size, polymer type, temperature, flow rate and pressure.

Further investigation based on capillary's technique was carried out in the late 1960s by Choi [28], who developed a capillary device from an extrusion rheometer that consisted of a barrel and capillary in series. Several different capillaries with various L/D ratios were used to alter the mean pressure from circumambient up to 175 MPa, and the barrel was used as the main capillary tube for viscosity determination. He found that the viscosity of polyethylene which tested at 190 °C and shear rate of 7.12 s^{-1}, was increased nearly over the full range of pressure. By colouring the layers of the melt with tracers, he studied the flow pattern in the barrel and found regular laminar flow but, this method was not satisfied because of its limitation at low shear rates of range less than 10 s^{-1}. Consequently, more investigation was carried out by Choi and Nakajima [29], where they considered another method to study the higher shear rates up to 500 s^{-1}. Their technique involved the study of the non-linearity of Bagley-type plots at high pressure (*making refined calculations from the non-linearity in plots of pressure drop versus*

length of die). The earlier capillary techniques had disadvantage, that the shear stress is determined by the same force which gives rise to pressure. However, this disadvantage was overcame later through the "pressurized Couette-Hatschek viscometer" which firstly was used by Semjonov [30], then by Cogswell and McGowan [31] who carried out an investigation to study the effect of temperature on the viscosities of polymer fluids. Later on by using the same device, Cogswell [32] studied the effect of the pressure on the apparent viscosity of polypropylene. He found that, the increase of pressure in the process equivalent to the decrease in the temperature, and explained that as; if the viscosity of the polymer was responsive to the change in temperature, at that time alike sensitivity to the change in the pressure could be expected. Studying the impact of pressure on viscoelastic properties was also done by Ellis [33], who used an ultrasonic technique to measure the viscoelastic relaxation for polymer solutions in the high frequency range at high pressures, and found that the shear modulus of all the liquids tested increased linearly with pressure at ambient temperature.

Furthermore, investigation carried out to study the effect of the pressure on the viscosity of the fluid by D.M. Binding, et al. [34] used a capillary viscometer to measure the pressure drops that associated with the capillary and entry flows for a number of polymers with high and low density. They studied the behaviour of the polymer with range of shear rate between 50 and 2500 s^{-1}, at pressure rang from atmospheric up to 70 MPa, and found that, the shear rate and extensional viscosity curves for all of the tested polymers are exhibited an exponentional pressure dependence that can be characterized by pressure coefficients which was found to be independent of temperature.

1.2 Literature review

1.2.1 An overview of lubrication in wire drawing

In wire drawing process, the requirement for high-quality wire is a desirable target. Selecting the proper lubricant is a key factor for higher quality wire drawing. It also provides efficiency, better surface finish, good heat dissipation and reduction in

production time during the process. As for production time reduction, more factors have to be considered:

- *Reducing drawing time*
- *Elimination of Redrawing time*
- *Reductions of number of inter- pass heat treatment*
- *Reducing die setup time (e.g. replacement or maintenance)*

In general, wire drawing processes involve the drawing of a wire through either, an incessantly conical or cylindrical die. The main idea of the wire drawing process is to reduce the diameter of the wire to a particular size and to obtain a good surface finish including required metallurgical properties and repeatability. Metal to metal contact takes place in the wire drawing process which causes friction between the die surface and the wire which reduces the die-life because of wear and the drawing load. Because of this, lubricant is essential to minimize friction, reduce die wear, keep the die cool and produce a good quality of wire surface finish. In general, two types of lubrications are used; the first is "wet drawing method", where the wire is dipped in a bath of lubricant fluid. This mode produces a high quality of a wire surface finish. The second is "dry drawing method", where the wire passes through a container of soap powder before entering the die. This mode is used when the surface finish is not so significant or when lubricant is wanted for supplementary processing.

Overall, friction through metal-to-metal contact occurs in both methods of the wet and dry drawing even if the lubricant is present. To increase the die life and to obtain a good surface finish, hydrodynamic lubrication technique is applied, where hydrodynamic pressure develops because of the viscous action between the wire surface and the lubricant.

Several attempts have been made to create the use of the hydrodynamic action in the drawing process. Various models for analyzing wire drawing/coating process have been developed based on lubrication techniques for various die features and

different types of fluids to improve the need for better wire drawing development. The earliest achievement was considered by using oil as a lubrication fluid, it was studied by Christopherson and Naylor [35] who designed a long tube attached to the front end of a conventional die, as shown in the Figure 1.10. In this case the wire was pulled through the die, it pressurized the oil by means of viscous action and fed into the inlet die, the pressurized oil completely separates the wire from the die avoiding metal to metal contact. The results presented by their experimental work proved that the deformation of the wire occurred in the tube before entering the die. The wire industries found their system was very difficult to be set into a real practice because of the pressure nozzle, which was in a vertical position and had such a length. However, the technique showed that hydrodynamic pressure was achieved in the design conditions.

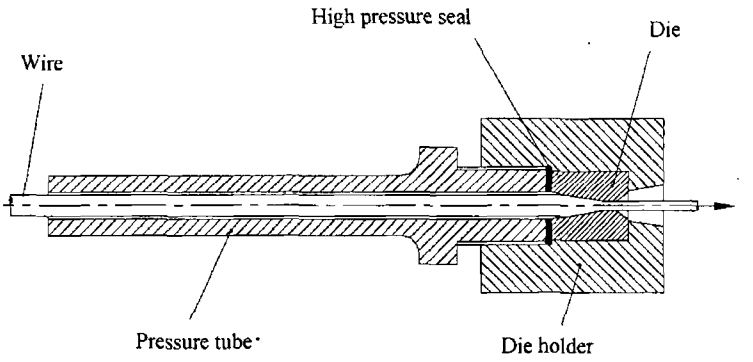

Figure 1. 10: Schematic diagram of long tube die used by Christopherson and Naylor

Following their work Wistreich [36] applied dry soap for lubricating to study a forced lubrication and used a system of pressure tube; the soap powder he used was applied in a short nozzle *(2 inch in length)* attached to the entry-side of the die. Figure 1.11 shows a schematic diagram of the short nozzle that he used. He found that the temperature, speed and the geometrical configuration of the gap affect the

properties of the produced film thickness directly. And he also noticed that using soap as lubricant produces a thinner film than using oil.

Tattersal [37] presented a detailed analysis publication of plasto-hydrodynamic lubrication action in wire drawing by considering a number of rheological and metallurgical properties of the process in account. The experimental results and theory showed a logical agreement. Following this work, Chu [38] used the results obtained by Tattersal, and presented a chart for the inlet tube he designed. After that, Bedi [39] established an analysis which intended for wire drawing technique by assuming absolute hydrodynamic lubrication.

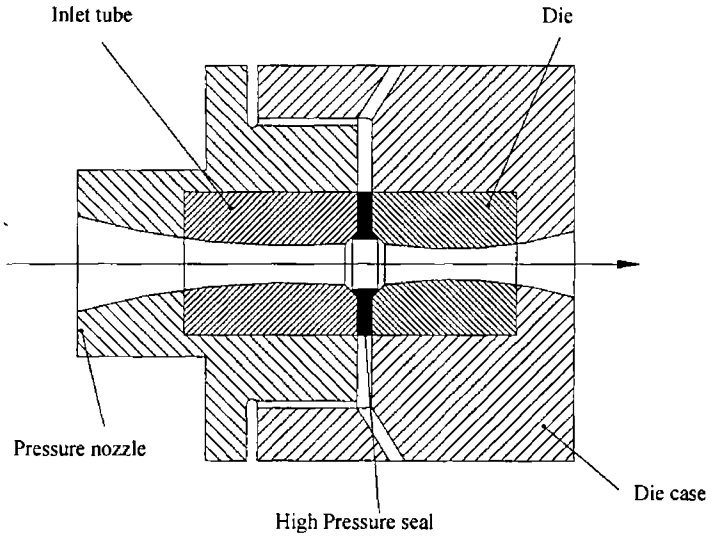

Figure 1. 11: Schematic diagram of short nozzle used by Wistreich

Middlemiss [40] enhanced the earlier use of drawing unit and applied an externally pressurized lubrication arrangement. Subsequently, by using soap powder as a lubricant in the tube sinking technique under hydrodynamic action, Kalmogrov and Selishchev [41] experimented a similar wire drawing device, in which there was no seal set between the nozzle and the die, that was because the lubrication process being much lower in the tube sinking system. Following their work, an analytical study has been achieved by Bloor et al. [42], where a theoretical analysis was obtained for elasto-plasto hydrodynamic lubrication action

in conjunction with strip drawing within wedge shaped dies. They studied account of elastic component in the strip at both entry and exit of the die and the pressure and viscosity characteristics of the lubricant. Their results showed that, by comparing the magnitude of the predicted lubricant film thickness the hydrodynamic lubrication could be achieved at some stage in the process.

Subsequently, Orlov et al. [43] developed a double die arrangement approach of externally pressurized oil, where the lubrication fluid was transported though the exit cone chamber of the pressure die and entry part of the drawing die, and hydrodynamic lubrication was provided by the pressurized oil during the drawing process. Figure 1.12 shows a schematic diagram of the pressure nozzle die they used.

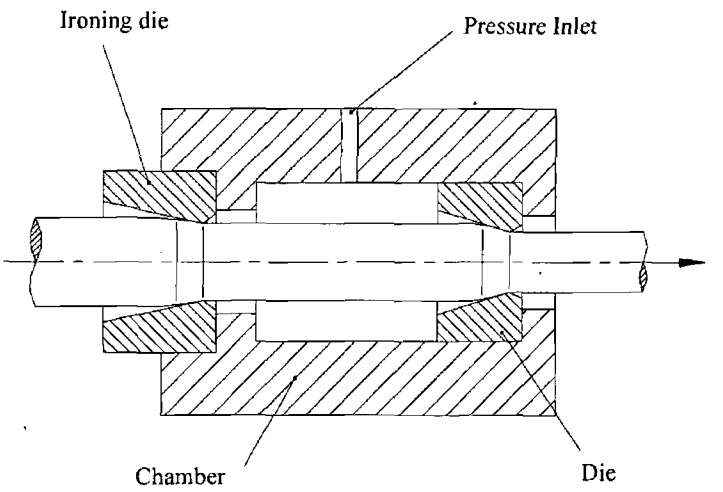

Figure 1. 12: Schematic diagram of the pressure nozzle die *(pressurized chamber used by Orlov [84])*

1.2.2 Utilization of Polymer Melt in Drawing Process History

The use of polymer melts as lubricants was applied in manufacturing processing because of their vast fundamental characteristics comparing to other lubricant materials such as soap and oil. So many differences can be observed in the rheological behaviour of molten polymer compared with typical lubricants, where the most noticeable rheological parameter is a remarkably high viscosity of

polymer melts at higher temperatures. It could be a significant benefit to avoid using the oil as a lubricant in some heavy loads process, where the system journal-lubricant film in a hydrodynamic journal bearing concerning non-Newtonian fluid as lubricants have been earlier investigated and found to be beneficial for bearings involve oscillatory load which induce fatigue loading [44]. The polymer melts were used first in deep drawing and hydrostatic extrusion. The earlier study in polymer melts as a coating material involving drawing process was investigated by Thompson and Symmons [45, 46]; who explored the adherence of polymer coat and analyzed the criteria of polymer coat thickness on the steel wire. They used Christopherson tube [35] and polymer melt as a lubricant and found that the operating characteristics of the device produce a reduction in thickness of the coat as the wire speed is augmented. After that, further investigation was carried out by Stevens [47]; who designed a hydrodynamic pressure wire coating unit consisting of a pressure tube connected to a conventional die. The motion of the pulled wire drags the polymer melt into the tube and generates high hydrodynamic pressure. He found the polymer to be very effective as a lubricant and leaves a protective coating on the wire surface.

Following his work; an investigation was carried out by Crampton et al [48-49] where a device based on an adaptation of the Christopherson tube was applied by employing a polymer melt as the lubricating agent to study the effect of wire speed on the process, they found that, on the basis of experimental proof, the deformation initiated before the die in the Christopherson tube itself, the die effectively acting only as a seal, and the thickness of the coating zone is dependent on the wire speed. Figure 1.13 shows a schematic diagram of the unit they used.

Soon after, Parvinmehr et al. [50-54] presented research results of an experimental and theoretical study of a novel technique of wire-drawing process which, carried out by replacing the conventional reduction wire die by a die-less stepped bore reduction unit, which consists of two parallel bore sections that provide the die, where the smallest bore size was greater than the pulling wire

diameter, that avoids metal to metal contact. In their study the wire diameter was induced by the hydrodynamic action of the polymer melt within the unit. They analyzed the system by taking account of Newtonian and non-Newtonian characteristics of the polymer melt and found, using this technique of wire drawing eliminates the wear and breakage problems during the start-up in the die. Also, because of the easy insertion of the wire through the unit, the leader of wire is no longer essential as they reported. Soon after, Hashmi and Symmons [55] achieved a numerical solution development for a conical tubular orifice through which a continuum is drawn. The results they obtained had a good agreement between the theoretical and experimental work at low drawing speed, but for high drawing speed it was poor as they observed.

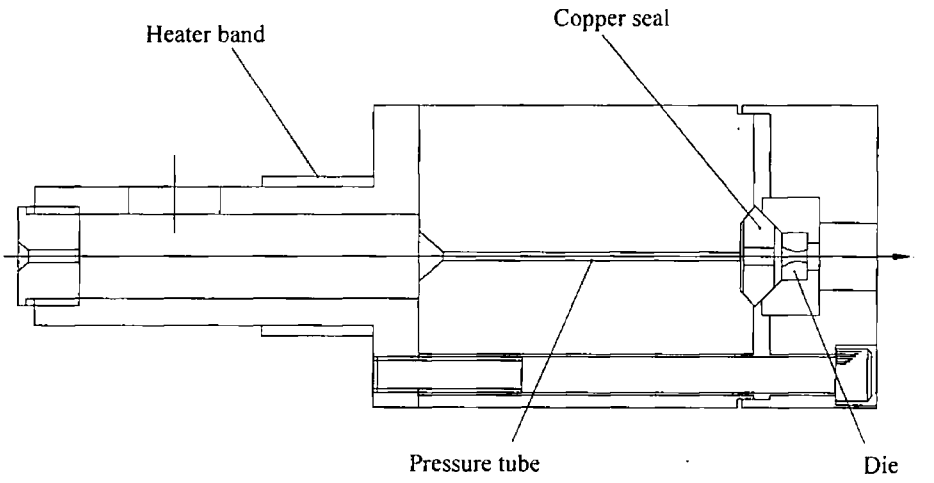

Figure 1. 13: Pressure tube-die and Christopherson tube arrangements

Panwher et al. [56] presented a brief report that shows the effectual reduction of wire diameter using a polymer melt is possible only in a stepped bore tubular system. Later on, they reported [57-59] a technique of tube sinking process in the stepped parallel bore unit filed with polymer melt, and presented an analytical solution based on Newtonian characteristics of the polymer melt. Following their work an investigation carried out by Symmons et al. [60-61], who analytically considered a die-less wire drawing process by using the experimental appearance of viscosity-pressure and viscosity-temperature relationships for the deformation of

the strip by using a stepped parallel bore arrangements. After that, Panwher et al. [62] researched the same system they used before and analyzed the process by taking account of the Non-Newtonian characteristics of the polymer melt while a copper tube was pulled through the unit.

Several theoretical and experimental studies also have been achieved by Memon et al. [63-67] on strips and wires in conjunction with plasto-hydrodynamic concept. In their experimental investigation, they compared the coating performance on copper wire by applying various polymer types with different melt index and various viscosities. They found that, the adhesion is good with polyamides and the coat quality improved using a low melt index polyethylene. They studied the effect of the temperature and the process speed as well and found the temperature of the polymer and drawing speed had significant effects on both the reduction of the area and quality of the wire coating. Their experimental results showed good agreement with the theoretical results. Soon after, an analytical investigation was carried out by Al-Natour and Hashmi [68,69] who developed a complex geometry unit of hydrodynamic pressure device which involves a combined parallel and tapered bore in conjunction with a polymer melt. They achieved an analytical theory to study the behaviour of the polymer melt through the unit by assuming Newtonian characteristics of the pressure medium.

Nwir and Hashmi [70-72] improved a comparative study to investigate the performance of various die gap geometries which involving a simple tapered bore unit, a stepped parallel bore unit and a complex geometry pressure unit, by considering the polymer melt as a non-Newtonian fluid in terms of pressure distribution, maximum pressure and axial stress. They studied the impact of the geometrical configuration of the die on the process consequences. The results obtained were experimentally employed on the stainless steel and copper wires.

In the meantime, Stokes and Symmons, presented experimental investigation results, by using various grads of polyborosiloxane with polymer melts including nylon and polydimethylsiloxane, they compared the deformation for two different types of wire materials (copper wire [73] and steel wire [74]). The results showed a

smooth adhered wire coating which obtained with the nylon and significantly different reduction ratios. Afterward, they developed a difference computer model of plasto-hydrodynamic strips drawing system to the process of numerical multi-dimensional optimization [75]. Then , Hillery and Symmons [76], published a paper which describes a drawing programme of mild-steel wire by using molten polymer and glass materials as lubricants and using a "double bore" non contacting die at temperature varying from ambient to 600°C. They developed a stress analysis model of the deforming wire which takes into consideration lubricant viscosity. The schematic diagram in figure 1.14 shows the die and tube furnace arrangement they used in their experimental work. They found that up to 12% reductions can be achieved by using this technique.

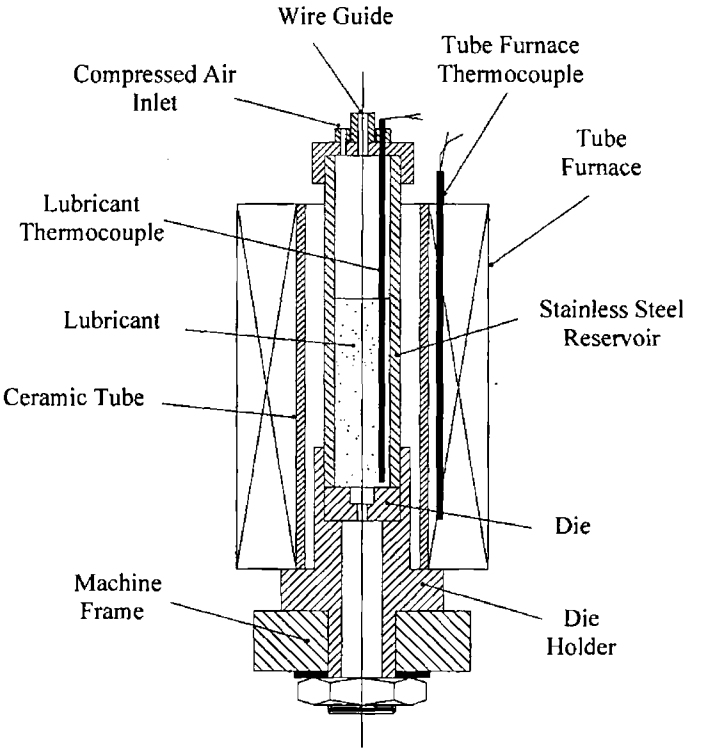

Figure 1. 14: Die and tube furnace arrangement [76]

After that, Akter and Hashmi [12 and 77-82], presented several research publications relating plasto-hydrodynamic phenomenon of wire drawing and coating in terms of altering the process parameters such as type of polymer and geometry shape configurations, taking account of changing in the pressure distribution, the variety of viscosity and temperature. They developed new mathematical models for different types of pressure unit considering the polymer melt characteristics as non-Newtonian fluid. Subsequently, further investigation was carried out by Iqbal and Hashmi [83-85] who studied the rheological properties of a viscous fluid flow by means of plasto-hydrodynamic action in conjunction with experimental and theoretical results. They built a novel of rheological rotating device based on a concept of stepped parallel bore approach of wire drawing die. They considered the change in pressure distribution at various shaft speeds within the unit, while the change in viscosity during the process at higher shear rates was observed analytically.

1.3 Objectives of the present study

The wire drawing and coating processes by means of plasto-hydrodynamic technique in the die-less unit have been explored and studied by many researchers. Most works were done on actual units, which become at times costly studies.

The requirement for improved understanding of the circumstances of hydrodynamic action within the drawing process involving fluids with high viscosities; a modelling of a plasto-hydrodynamic rotating unit based on the stepped- parallel bore concept was used to study the fluid behaviour within the rotating unit at high shear rates in conjunction with wire drawing process, and because of the difficulties to place pressure sensors in some critical positions on the die surface, which might cause damage to the die, especially at the step, the pressure distribution was not observed along the whole die, just at several locations *(See Figure 2.9)*.

Because of the limitations stated above, the main targets of the present work are to analyse new geometrical shapes for the die of the plasto-hydrodynamic rotating

unit based on a concept of a tapered-stepped-parallel bore and measure the hydrodynamic pressure for three types of viscous fluids at high shearing speed experimentally. Moreover, using Computational Fluid Dynamics *(CFD)* tools to build computational models to observe the pressure distribution profile along the whole die and study the behaviour of various viscous fluids for the process at high speed as well as, observing the change in viscosity within the die. The detailed purposes of this project are listed below:

1. Modify the experimental device of plasto-hydrodynamic unit by designing various geometrical dimensions of the tapered bore,
2. Determine the pressure distribution and its development at three different locations inside the die for various types of viscous fluids at different shear rates within each gap.
3. Measure the viscosity of each viscous fluid by using Cone-Plate viscometer type at a lower range of shear rates and determine the impact of changing shear rate on viscosity.
4. Build a CFD model for the die in the grid system for all gaps.
5. Run the computational model based on non-Newtonian characteristics to determine the change in viscosity at higher shear rates.
6. Observe the development in the pressure distribution profile and its variation with an increase in shearing speed.
7. Compute the relative velocity magnitudes of fluid layers within the gap.
8. Discuss and compare the experimental results and the computational results and determine the effect of pressure on the fluid viscosities with the viability of the process and its limitations in relation to realistic purposes.

Chapter Two

Experimental Equipment and Procedures

2.1. Description

A plasto-hydrodynamic unit of a parallel-stepped die was constructed by Iqbal and Hashmi [84]. It has been used as a test bench to study the behaviour of different viscous fluids to simulate the behaviour of polymer melts in the wire drawing process. a general view of the rotating unit and a schematic diagram of the bench layout are shown in Figure 2.1 and Figure 2.2 respectively.

Two segment inserts *(parallel shaped)* are attached to the inner surface of a fixed hallow cylinder. Those inserts work as the parallel-stepped die and a rotational solid shaft presents a moving surface within the unit. The unit is driven by an electric motor of three phase power supplier and squirrel cage 3 kW. The rotating speed is build-up by an accelerator time sets on the frequency inverter which contrasts the setting of the motor speed. By using a Remote hand held digital tachometer (DT-205) type, the actual motor speed can be measured. These arrangements provide shearing speeds between 0.25 to 2 m/sec.

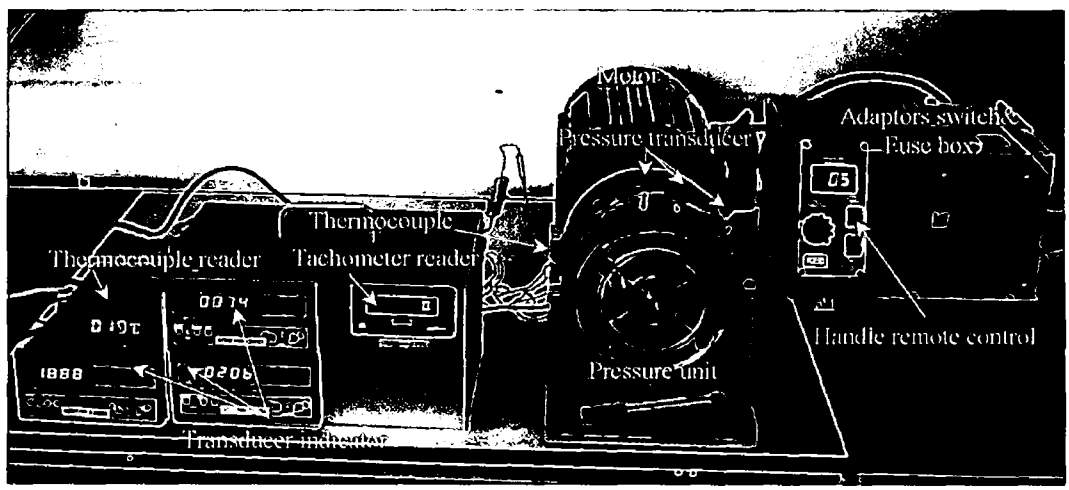

Figure 2. 1: General view of the rotating unit bench

To measure the pressure distribution within the die, two pressure transducers were located in the unit at the middle of each insert and a thermocouple also was inserted within the unit to measure the process temperature.

In this study, a new die design (tapered-stepped-parallel) is used. The new design has several tapered shape inserts with different dimensions. The first parallel insert in the original unit was replaced by a tapered insert. A third pressure transducer was placed in the unit near the step to measure the additional pressure. The pressure transducers are connected to the transducer indicator units to monitor the digital signal of the pressure.

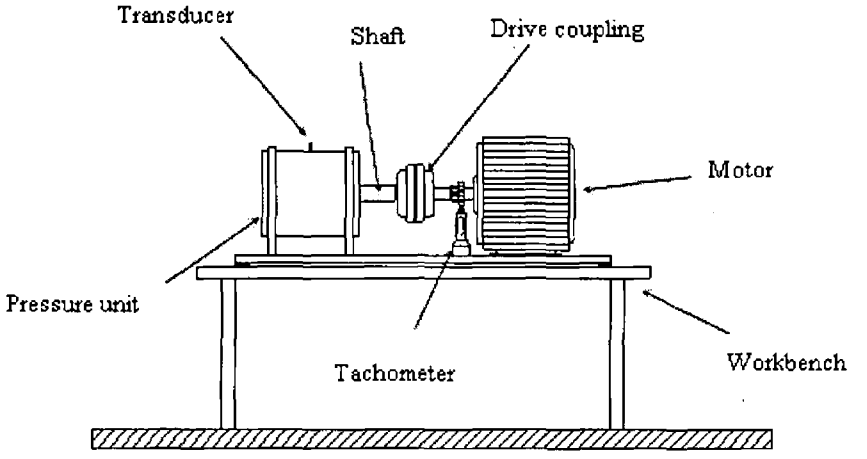

Figure 2. 2: Schematic diagram of the plasto-hydrodynamic rotating unit

2.2 Instrumentation Requirements

In the industrial applications, using good instrumentations enables a continuous monitoring of the *(vital signs)* of the process, these *vital signs* are the power supply, pressure development, the shearing speed and process temperature; these significant process parameters are required to be considered for process control, although they are also of vital importance in troubleshooting. Therefore, several pieces of equipment and various devices are used to observe the experimental work and to obtain accurate results within the process. In order to determine the achievability of the system; the details of the devices and equipments were used during the tests are listed below:

2.2.1 Rotational speed measurements (Tachometer Unit)

2.2.1.1 Digital Magnetic Pickup

The most common method to measure the rotational speed is a *magnetic pickup* technique. The *model RS304-172 pickup* was used in this study, as shown in Figure 2.3, which is connected to the rotating shaft via the motor and the speed was regulated manually by a frequency inverter via the remote control unit of the motor. The basic idea of the magnetic pickup technique is a metallic-toothed-wheel coupled to the rotating shaft and a magnetic pick up coil. The pickup consists of a housing containing a small permanent magnet with a coil around it. While the pickup is surrounded with a fixed magnetic field, once the wheel teeth pass through the magnet field, a voltage pulse is made in the coil. As the numbers of teeth are known, the frequency of the pulses may be known, where the pulse frequency can be related directly to the rotational speed and converted to a DC voltage [86].

2.2.1.2 Digital Tachometer Monitor

A digital tachometer unit involved a frequency regulator which was used to either monitor or to control the speed of the shaft. This digital tachometer is able to read the frequency directly. It is manually controlled by a remote control unit to either increase or decrease the shaft speed via the frequency inverter which can be easily operated from the remote control unit, and run the motor forward or in reverse, start or stop the motor, regulate the speed of the motor and read the frequency which the motor is running at.

Figure 2. 3: Magnetic Pickup

2.2.2 Temperature measurement

2.2.2.1 Thermocouple temperature sensor

The developed temperature can be measured by thermocouple temperature sensors (TC), which are also known as thermoelectric transducers. In this study, a K-type thermocouple temperature sensor was used to measure the temperature during the experimental process. The range of thermocouple temperature working is 0-45 °C. Figure 2.4 shows the thermocouple temperature sensor and its monitor, which are used in the experimental work.

The concept of the thermocouple sensors can be explained as following; a pair of wires with dissimilar metals are joined together at one end (hot junction or sensing junction) and terminated at the other end by terminals (the reference junction) maintained at constant temperature (reference temperature). When there is a temperature difference between sensing and reference junctions, a voltage is produced. This phenomenon is known as the thermoelectric effect. The amount of voltage produced in the circle depends on the difference in the temperature and varieties of metals combinations used. Thermocouples have various configurations such as exposed junction, grounded junction, ungrounded junction, surface patch, etc. [87]

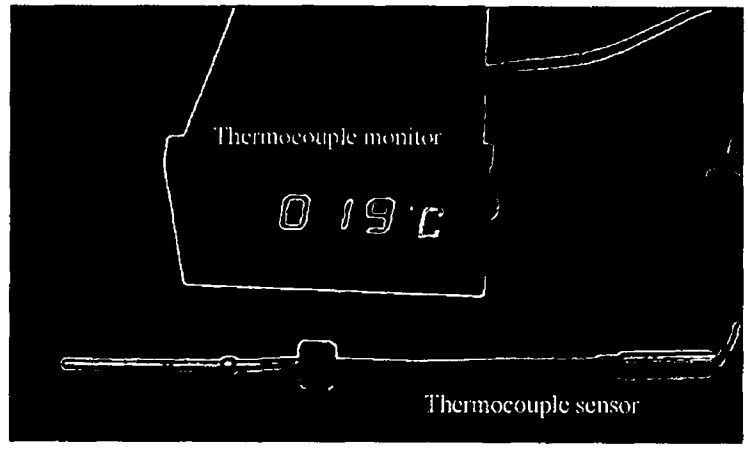

Figure 2. 4: Thermocouple and its monitor

2.2.3 Pressure Measurements

2.2.3.1 Pressure Transducers sensors

To measure the developed pressure gradient during the process, three pressure transducer model *(S/1543-09G)* are used. Two of the pressure transducers are inserted in the tapered zone at two different locations to measure the developed hydrodynamic pressure within the tapered zone, and the third transducer is inserted in the middle of the parallel zone.

This type of transducer has the ability to transform a very small mechanical deformation (input signal) into an electric output signal (voltage). The bonded strain gauge system results in the robust transducer of high accuracy that suits both static and dynamic pressure measurements. The maximum pressure measurements can be provided by this transducer is 6.89×10^3 kPa and its working voltage is 5 volts with shunt resistance of 59 kΩ.

2.2.3.2 Transducer indicator (pressure reader monitor)

For strain gauge type transducers such as load cells, the Transducer indicator model E308 of RDP-group is an inclusive transducer display instrument which provides indication conditioning excitation and ± 19999 digit signals, and for transducers with built-up electronics producing high output signals. Table 2.1 shows the pressure transducers and the transducer indicator units with their calibrations procedures and shunt resistance. Figure 2.5 shows the pressure transducer and the transducer indicator unit.

2.3 Installation of Electrical power set up

The motor is connected by a three-phase plug to the main supplier and controlled by the frequency inverter via an electrical adaptor switch and the fuse box. The rest of the electrical instruments on the bench are carried by two-phase electrical supplier.

Table 2. 1: Pressure transducers and Transducer indicator units' calibrations

Pressure transducer	Transducer indicator	Pressure capacity (kPa)	Shunt Resistor (kΩ)	Shunt calibration factor (MV/V)	Calibration Factor (MV/V)	Calibration value
Transducer-1	Transducer indicator -1	6.89×10^3	59	1.487	2.430	2697
Transducer-2	Transducer indicator-2	6.89×10^3	59	1.4901	2.3614	2780.9
Transducer3	Transducer indicator-3	6.89×10^3	59	1.490	2.463	2666

Figure 2. 5: Pressure transducers and Transducer indicator unit

2.4 Design of the rheological rotating device

2.4.1 Introduction

The need for developing wire drawing and coating process to reduce the use of the material and its expenditures gives the idea to build the rotating shaft model. Therefore, the main purpose of the experimental plan was to create a model of a

rheometrical device and to investigate the development of pressure based on rheological properties of non-Newtonian characteristics. The unit is modified based on a tapered-stepped-parallel shape gap made from mild steel parts. The whole length of the pressure unit is 155 mm and consists of pressure cylinder, two inserts, central rotating shaft, pressure end plate, and the shaft end plate. It was designed to gain easy access to the pressure unit rather than assembling the actual wire drawing unit. Figure 2.6 shows the assembly arrangements of the plasto-hydrodynamic pressure unit and its details.

2.4.2 Design information of the pressure unit parts

2.4.2.1 Pressure Chamber

The pressure chamber made from mild steel with total length of 155 mm and outer diameter of 150 mm. it has two different cylindrical spaces; the first cylinder is the outer casing of the unit which represents a pressure chamber with 65 mm of length and 100 mm of inner diameter. The second cylinder represents a rotating shaft with 74 mm of length and 62 mm of diameter. The pressure cylinder has three M8 socket head cap screws (SHCS) at three different locations for the pressure transducers. The screw was drilled in 14.5 mm deep followed by a straight hole through the cylinder with diameter of 2 mm. Another M8 socket made for the thermocouple. Figure 2.7 shows the pressure cylinder with its details dimensions.

2.4.2.2 Central rotating shaft

The shaft rotates inside the pressure chamber and applies as a central cylinder. It is a solid cylinder made from stainless steel with a diameter of 50 mm and length of 90 mm. the shaft is supported by two bearings model Fag 6012-type. The shaft is attached to the electric motor via a drive coupling. The speed of the shaft is controlled via the frequency inverter which is connected with the digital tachometer and the magnetic pickup as mentioned above. Figure 2.8 shows the shaft details and its diamentions.

2.4.2.3 Design of the Converging Gap in the Tapered-Stepped-Parallel Rotating Unit

Basically, the gap of the pressure unit was designed in term of the tapered-stepped-parallel gap of wire drawing unit as shown in Figure 2.9. This gap was established by setting up two segments *"insert-I and Insert-II"* in the pressure cylinder within the rotating unit as Figure 2.10 shows. The details of the inserts design are given below.

2.4.2.3.1 Insert-I

Five different geometrical dimensions of insert-I were made with a general length of 40 mm and outer diameter of 50 mm. Insert-1 was made in order of a tapered geometrical shape, as shown in Figure 2.11 and Figure 2.12. This insert is attached to the outer casing by two M6 socket head cap screws, which drilled in 15 mm deep. Two holes were drilled at two different locations for each insert. Each hole has 2 mm of diameter. The first hole is made in the middle of the insert and the second hole is after 10 mm from the first one; via these holes the pressure transducers can amount the pressure gradient during the process at two different locations along the tapered zone, where at once the shaft rotates the hydrodynamic pressure develops in the pressure cylinder which can be obtained by the transducer indicator unit. Table 2.2 shows the dimensions of the insert-I.

2.4.2.3.2 Insert-II

Insert-II presents the parallel side of the bore with outer diameter of 50 mm, length of 10 mm and 24.9 mm width. It is attached to the outer casing of the pressure cylinder by two M6 socket head cap screws. The two screws were drilled in 15 mm deep. With these dimensions there is a hole in the middle of the insert to amount the pressure gradient within the parallel zone via the transducer indicator unit. Figures- 2.13 and 2.14 show the dimensional details of the insert-II design. The insert-II was adjacently attached with insert-I. The set of two inserts together provides the tapered-stepped-parallel bore within the pressure cylinder as shown in Figure 2.15.

Table 2. 2: Insert-I dimensions

Insert-I No,	Insert Outer radius (mm)	Insert thickness at the tapered inlet radial gap side (mm)	Insert thickness at the tapered outlet radial gap side (mm)	Height of the entrance radial gap (h_1) (mm)	Height of the end radial gap (h_2) (mm)	Tapered gap ratio
1	50	24.1	24.7	0.9	0.3	0.9/0.3
2	50	24	24.5	1.0	0.5	1.0/0.5
3	50	23.8	24.7	1.2	0.3	1.2/0.3
4	50	3.5	24.7	1.5	0.3	1.5/0.3
5	50	3.5	24.5	1.5	0.5	1.5/0.5

2.4.2.4 End plates

2.4.2.4.1 Pressure End Plate

The pressure end plate sets in the front of the pressure chamber. Figure 2.16 shows the drawing details and dimensions details of the pressure end plate. It has a diameter of 150 mm and thickness of 15 mm. The pressure end plate is attached to the pressure chamber by four M8 bolts. The bolts were drilled through 8.5 mm diameter on 125 mm in four places, and the angle between each two is 90°. The pressure end plate has a V groove for fixing a O-ring type *(on 108.5 P.C.D. and 3.0 wide x 2.0 deep).*

2.4.2.4.2 Shaft End Plate

The shaft end plate sets in the back of the pressure chamber and made of mild steel. It has a diameter of 150 mm and thickness of 6 mm with a passage of 35.5 mm diameter in the middle for the shaft. The shaft end plate is attached to the pressure chamber via four M8 bolts. The bolts were drilled with 6.5 mm diameter on 125 P.C.D. in four places, and the angle between each two is 90°. Figure 2.17 shows the drawing details and its dimensions of shaft end plate.

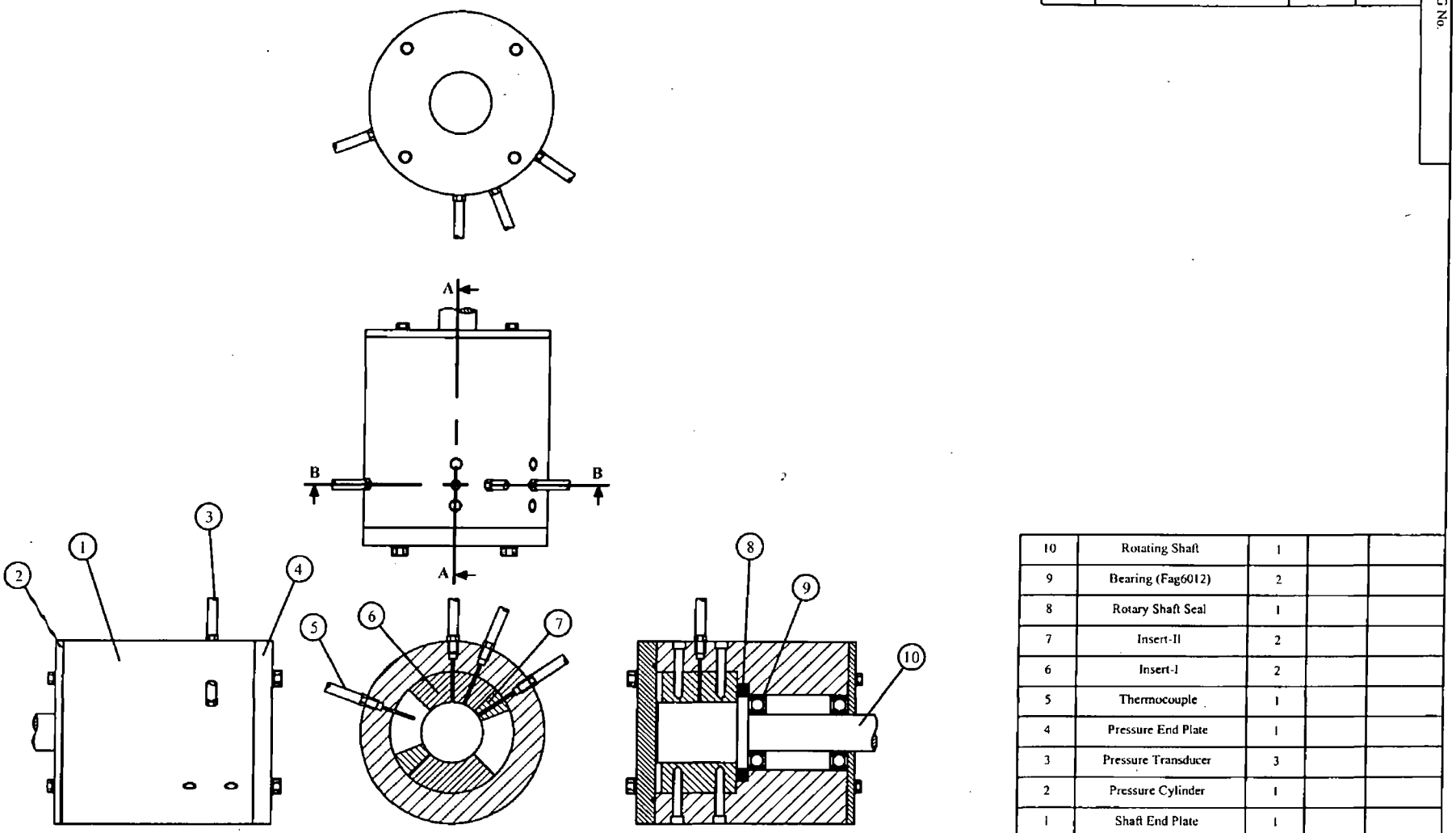

Figure 2.6: Plasto-Hydrodynamic Pressure Unit

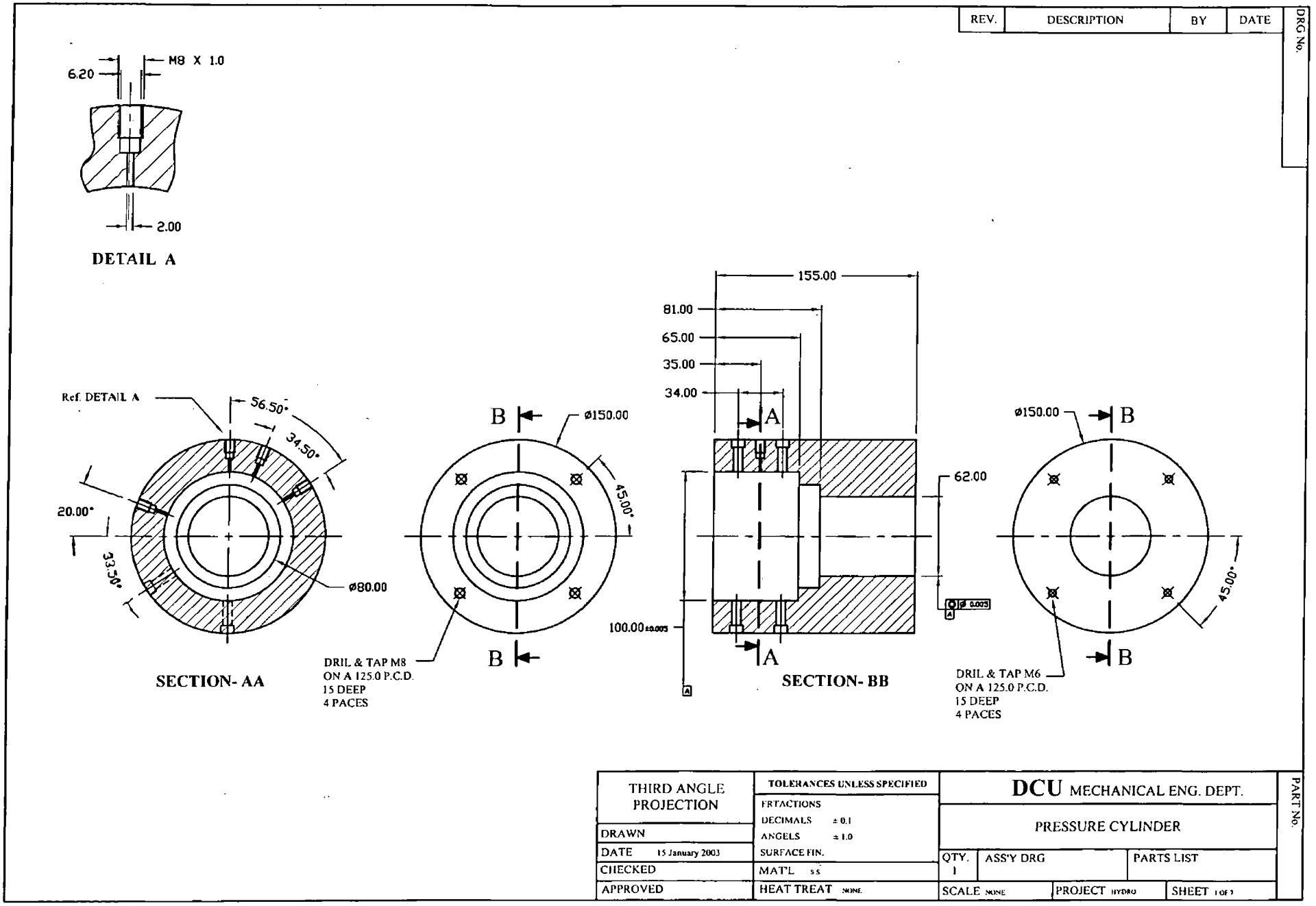

Figure 2.7: Schematic diagram of Pressure Cylinder

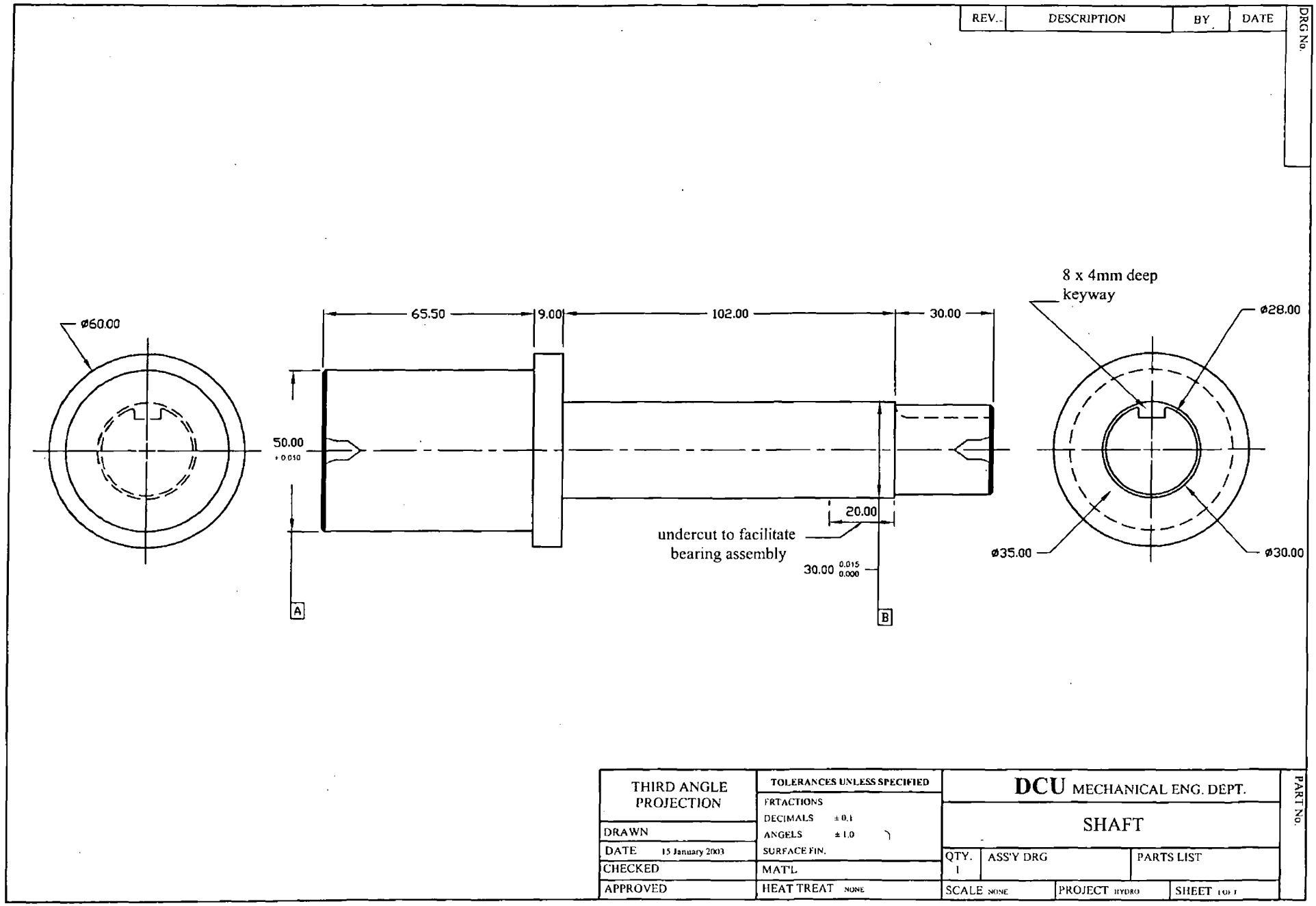

Figure 2.8: Central rotating shaft and its detailed dimensions

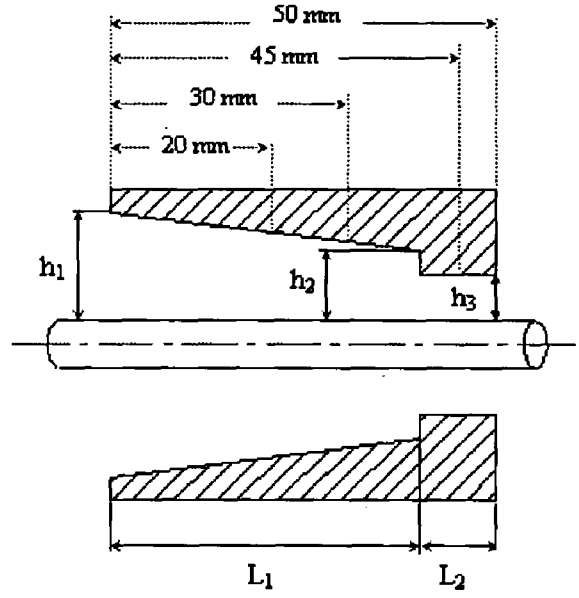

Figure 2. 9: Schematic diagram of an equivalent combined geometry of tapered-stepped-parallel pressure die

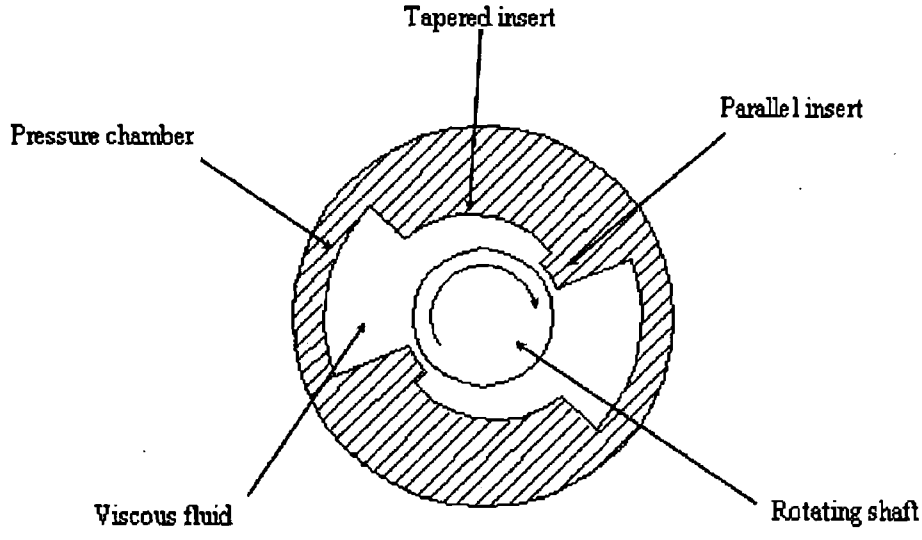

Figure 2. 10: Schematic diagram of the pressure unit

REV.	DESCRIPTION	BY	DATE

DRG No.

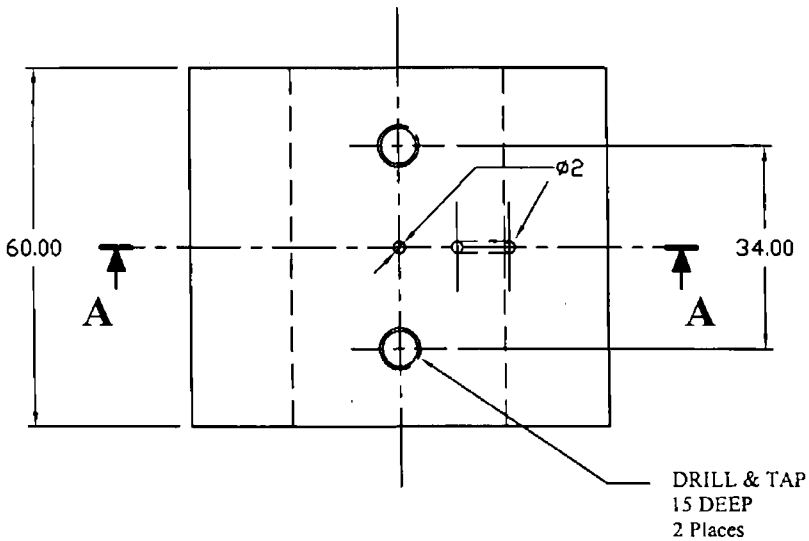

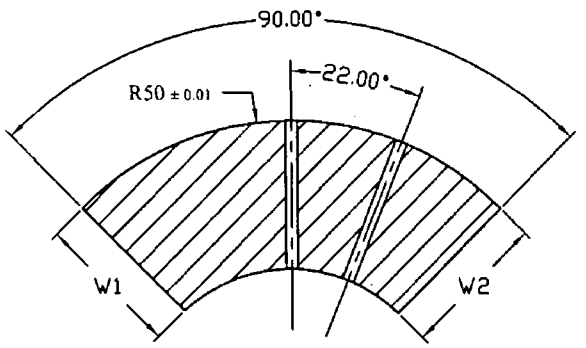

Type	Item No,	$W_1 \pm 0.10$	$W_2 \pm 0.10$
1	2	24.1	24.7
2	2	24.0	24.5
3	2	23.8	24.7
4	2	23.5	24.7
5	2	23.5	24.5

THIRD ANGLE PROJECTION	TOLERANCES UNLESS SPECIFIED	**DCU** MECHANICAL ENG. DEPT.		PART No.
DRAWN	FRTACTIONS DECIMALS ± ANGELS ±	**INSERT-I**		
DATE 15 January 2003	SURFACE FIN.	QTY.	ASS'Y DRG	PARTS LIST
CHECKED	MAT'L S.S			
APPROVED	HEAT TREAT NONE	SCALE NONE	PROJECT HYDRO	SHEET 1 OF 7

Figure 2.11: Schematic diagram of Insert-I

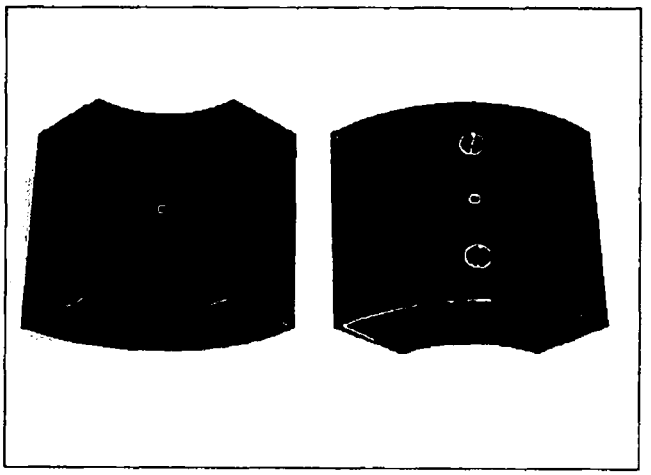

Figure 2. 12: Insert-I

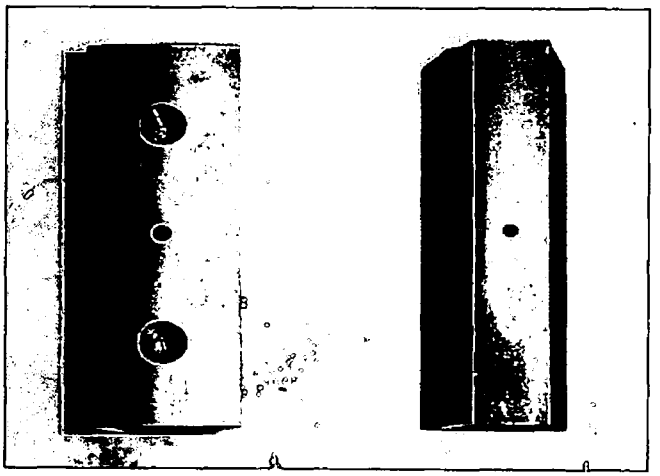

Figure 2. 13: Insert-II

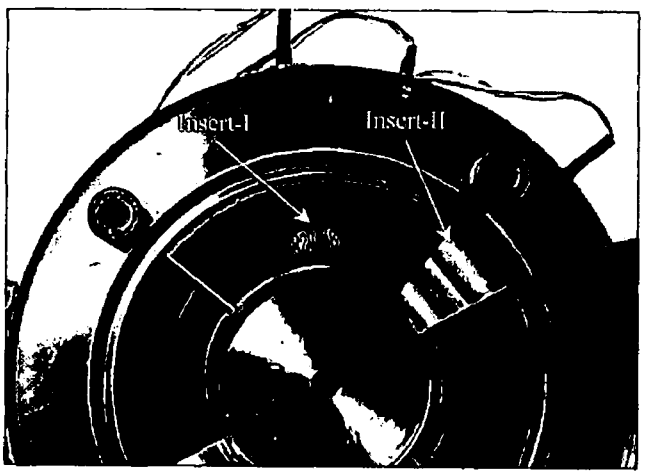

Figure 2. 14: Insert-I attached to insert-II

REV.	DESCRIPTION	BY	DATE

DRG No.

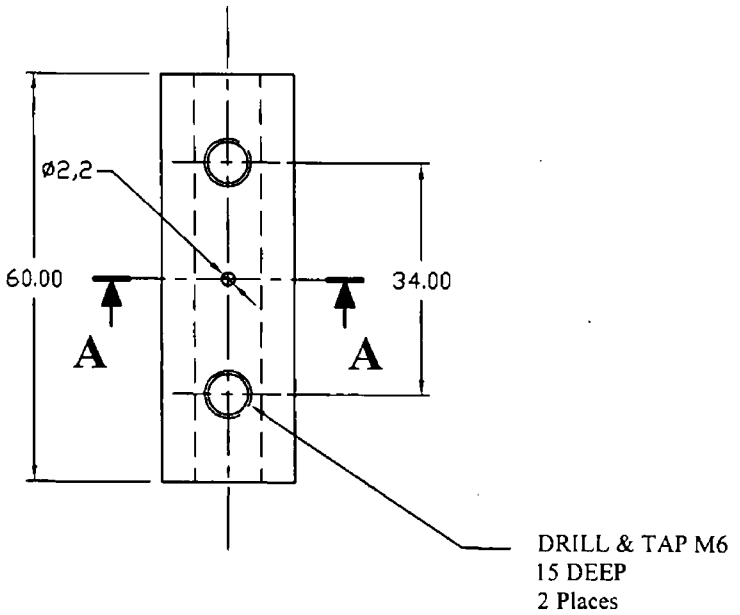

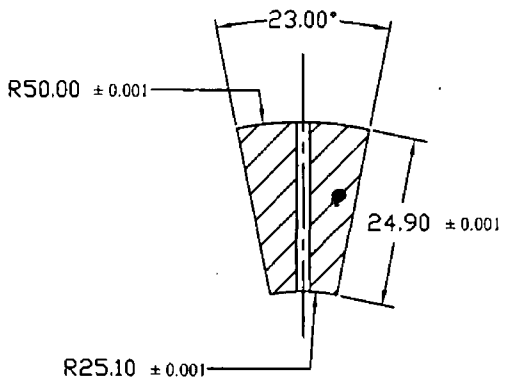

THIRD ANGLE PROJECTION	TOLERANCES UNLESS SPECIFIED	**DCU** MECHANICAL ENG. DEPT.		PART No.
DRAWN	FRTACTIONS DECIMALS ± ANGELS ±	**INSERT-II**		
DATE	SURFACE FIN.	QTY. 1	ASS'Y DRG	PARTS LIST
CHECKED	MAT'L S.S			
APPROVED	HEAT TREAT NONE	SCALE NONE	PROJECT HYDRO	SHEET 1 OF 7

Figure 2.15: Schematic diagram of Insert-II

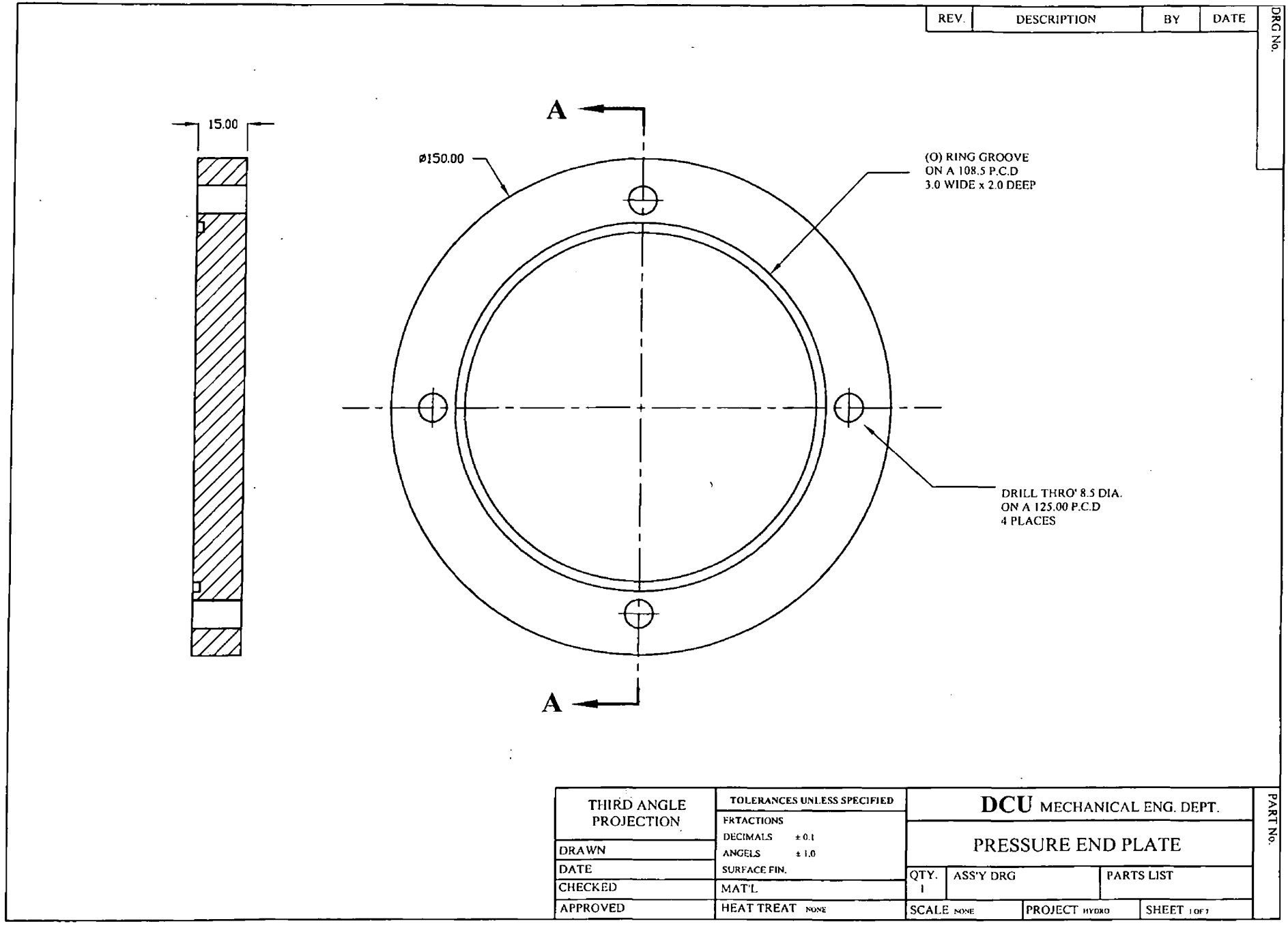

Figure 2.16: Schematic diagram of Pressure end plate

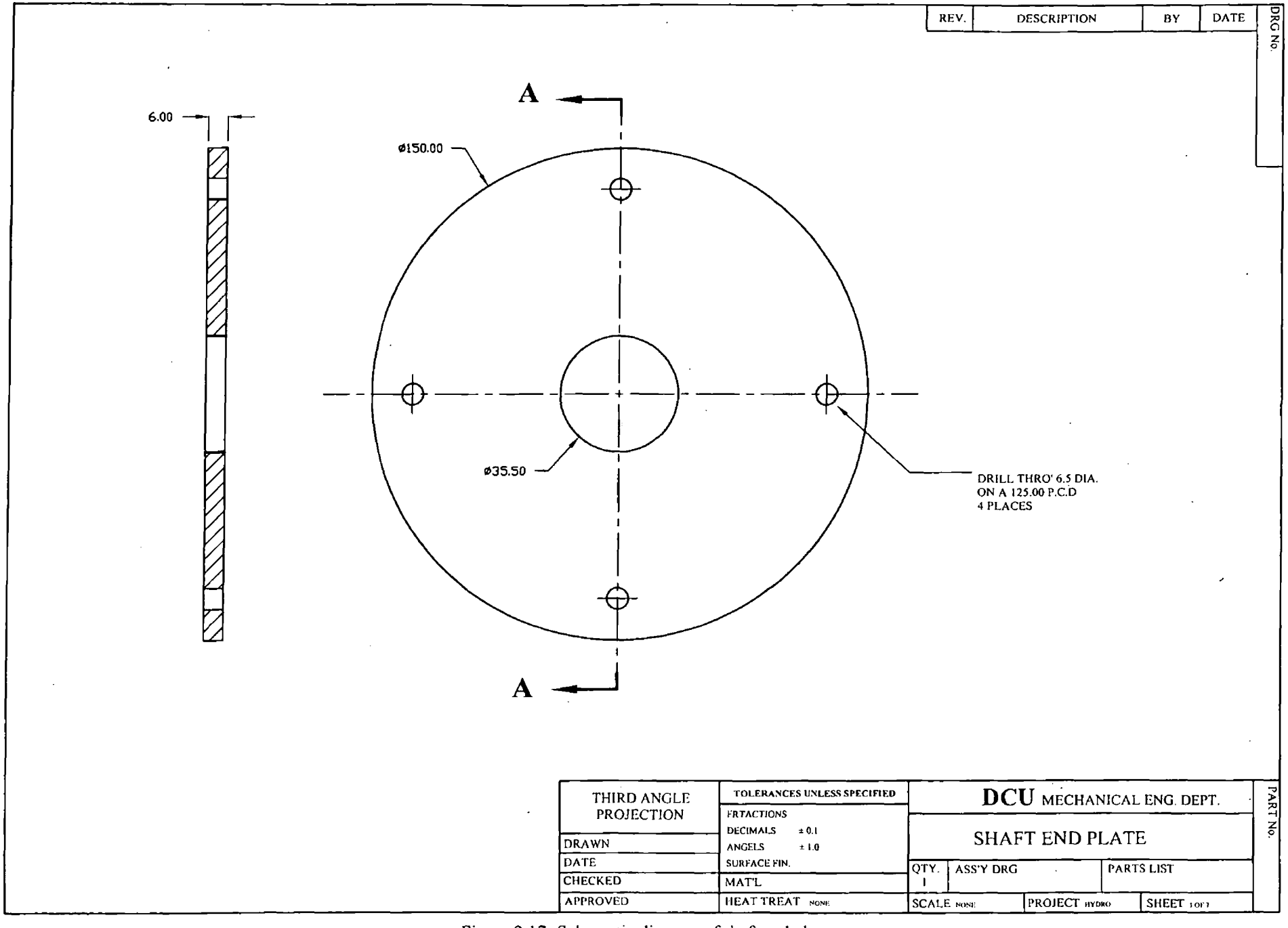

Figure 2.17: Schematic diagram of shaft end plate

2.5 Experimental work test procedures

The proposal test of the experimental work was carried out to measure the rotational speed for the shaft, the process temperature and the distribution of the hydrodynamic pressure within the tapered-stepped-parallel unit. To run the process, the motor is attached to the central shaft via a drive-coupling. The parameters were monitored and recorded continuously via the instrumentations. The pressure gradients were observed within the unit at three various locations. The process temperature measured via the thermocouple and the speed is measured by the tachometer through the magnetic pickup. Figure 2.18 shows a flow chart diagram for the test procedure setup of the unit

Earlier than assembling the unit together, all parts were cleaned up mechanically, and the pressure transducers were calibrated with oil hydraulic pump. For testing the shaft speed, the tachometer unit was calibrated with a standard hand held tachometer. Avoiding any leakage in the unit during running the process, all parts of the unit were sealed suitably.

After the unit was assembled together the pressure cylinder was filled with enough viscous fluid for complete test procedure. The pressure transducers were connected to the Transducer indicator units, where Transducer-1, 2 and 3 were connected to signal indicators-1, 2 and 3 respectively. The Transducer indicator units were calibrated at a desired value, which after switching on it was ensured that the reading from these units was not constant. After one hour from the calibration the readings were at the desired calibrated value. The calibration of Transducer indicator units described above in Table 2.1.

To reach the preferred shaft rotational speed, the motor speed was increased slowly to a certain desired amount by using the frequency inverter and recorded via the tachometer. For the whole test speeds, the process was run at ambient temperature, which was monitored via the thermocouple and pressure distributions were recorded via Transducer indicator units. For each fluid the tests were repeated

at least six times for each shearing speed and tapered-stepped-parallel bore setup. After completing the test the insert-1 was changed during the experimental work, and for each different bore setup the tests where obtained at three different shaft speeds.

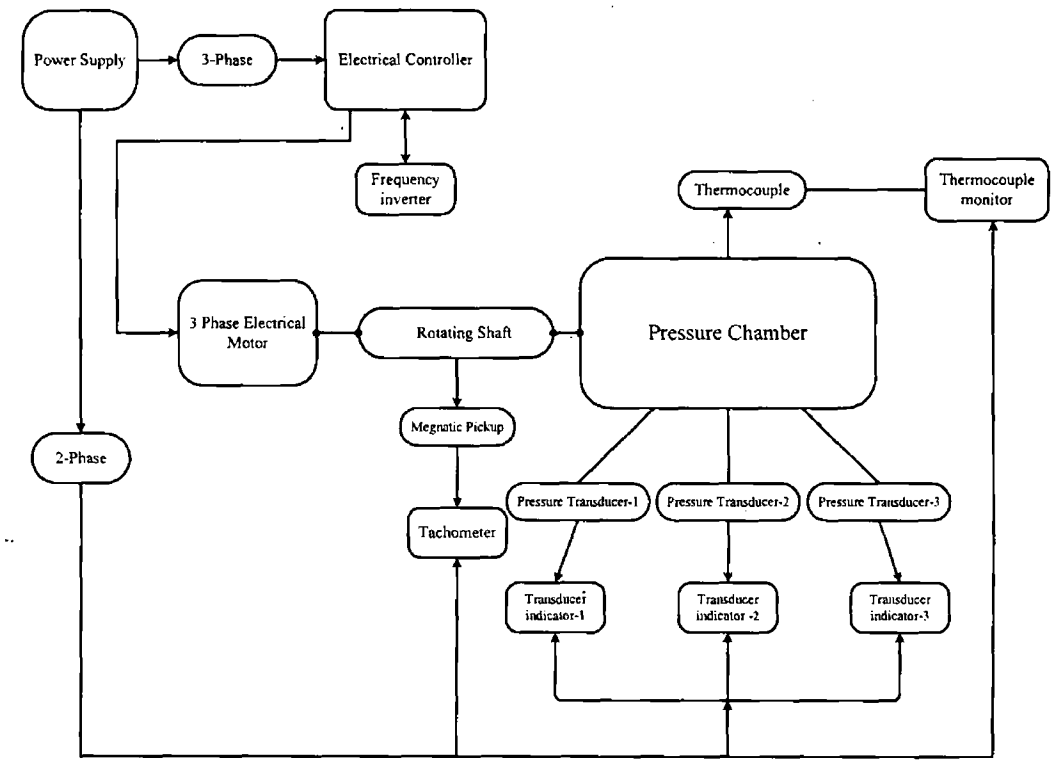

Figure 2. 18: Flowchart diagram of the test procedure setup

2.5 Experimental fluids

The pressure medium is represented by three different viscous fluids, which provide the performance of polymer melt without the need to heat the pressure chamber as the conventional die-less unit required. These viscous fluids are Glycerine and two types of silicone oils.

Glycerine is a clear, colourless and odourless sweet liquid. It is a viscous liquid with a chemical formula of (C_3 H_8 O_3). It is not oil but is derived from vegetable oils [88]. It was first discovered in 1779 by K.W. Shele in a hydrolysate of olive

oil. Primarily it was used in the glue and cork manufactures, colouring materials and ink. Later on, in 1867 A.B. Nobel produced explosives from glycerine.

There are two types of glycerine; natural glycerine which derived from oils, and synthetic glycerine derived from petroleum. In the natural glycerine production, normally crude glycerine is produced by first refining and condensing a sweet-water which obtained from hydrolysis of oils. Nowadays, because of the need to recycle resources, the natural type is the most used in worldwide industries. The pure glycerine normally contains over 95% glycerol. This fluid is very soluble in Water, Ethanol and Acetone, and insoluble in Ether and Benzene. It has a high boiling point 290 °C and melting point at 20 °C [89].

Glycerine is a very significant substance in so many industrial productions, such as applications include pharmaceuticals, cosmetics, toiletries, food products, monoglyceride, polyurethane, cellophane, films, toothpaste, mouthwash, inks, fragrant materials, cigarettes, and cigarette filters and much more.

Silicone oils used in this study are silicone-5 and silicone-12.5. Silicone fluids have exclusive properties because they are not products of petroleum or organic chemistry. They are products of inorganic chemistry which is the only type of polymers made by this method. The simplest silicones are polydimethylsiloxanes, which display the basic structure of the silicones with a Chemical formula of $\{(CH_3)_3SiO\,[(CH_3)_2SiO]_n\,SiO\,(CH_3)_3\}$.

Silicone fluids have a wild range of materials behaviours with various characteristics such as; change of viscosity is low with temperature, thermal stability, chemical stability, mechanical stability, dielectric stability, and high compressibility. These properties make silicone fluids suitable for use in various applications depending on their viscosities range as following;

1- Low viscosity silicone fluids are soluble in a larger range of solvents than higher viscosity fluids including petroleum oils. They present higher purity levels and extra discrete vapour pressure control than higher viscosity fluids.

2- Medium viscosity silicone fluids are used in numerous applications such as brake fluids, electronics and hand creams. They present brilliant, safe, low-volatility heat transfer media, mould releases for rubber, plastic and glass parts, lubrication for most non-metal to metal contact, and toners for photocopiers.

3- High viscosity silicone fluids are used as internal lubricants and process aids for thermoplastics and die casting. They are applied as band-ply lubricants in rubber industry, damping fluids for meters, and liquid springs in shock absorbers and load cell applications [90].

Chapter Three

Computational model

3.1 Introduction

Mathematical techniques are traditionally used to give accurate analyses for general engineering problems. Nevertheless, those mathematical methods can mainly be applied for simpler and easier cases. The mathematical techniques are often called analytical solutions. However, the real world applications in engineering are more complex to handle in simple mathematical forms, which dictate the use of better solution approaches such as numerical solutions.

The simulations can be carried out by the use of commercial software packages which can numerically evaluate the models and the required data together in order to solve and estimate the desired actual characteristics of the model [91].

In the recent two decades, Fluent software has become a practical tool for solving fluid flow problems. Based on a numerical technique named computational fluid dynamics or CFD, Fluent provides state-of-the-art models, standard with every fluid system that allows it to understand the physics of large problems. Nowadays engineers worldwide use the CFD as realistic tools to simulate many applications processes such as, air flow over an aircraft, combustion in a furnace, bubble columns, glass production, semiconductor manufacturing, wastewater treatment plants and blood flow in an aneurysm [92].

The CFD is a tool in which numerical simulations can be carried out, such as a program solves the complete two-dimensional Navier-Stokes equations for viscous flow as well as other governing equations for physical aspects of fluid flow by means of finite-difference numerical technique [93].

Number of researchers studied various applications which are only remotely related to this work involving the study of fluid flow around a moving surface [94-96].

3.2- Design of Simulation Model and its Parameters Definition

3.2.1 Preface

One of the complex issues in simulation in this study is to mimic the relative movement of rotating devices *(e.g. a moving rotor close to a fixed stator).* CFD simulation tools have introduced the Fluent-6 module to facilitate this task. The solution methodology proposed by Fluent-6 is based on a time-dependent sliding mesh formulation and steady-state approaches that use rotating and stationary reference frames.

The need to study the flow behaviour for high viscosity fluids involved with the moving surface has brought the idea of studying the developed hydrodynamic pressure. CFD tools provide systematic approach to analyse such pressure and its related parameters in a comprehensive manner.

CFD has been used in this study to develop two-dimensional models to simulate the experimental models of the plasto-hydrodynamic unit which examines various converging gaps and rotational speeds. The coming subsections describe briefly the basics of CFD tools to simulate the case under study.

3.2.2 The flexibility of the Computational Grid Technology

The principle of any CFD model calculation is a computational grid, this grid divides the solution domain into a huge number of elements where the problem variables are computed and sorted. The grid consists of various types of element shapes for each dimensional type. For 2D-simulation, the grid available in quadrilaterals and triangles shapes. For 3D-simulation the grid forms existing in hexahedral, prisms, pyramids and tetrahedral shapes. These elements can be created (*where the fluid flow takes place in the process*) by using *Gambit software* which is a fluent's companion per-processor.

3.2.3 Parameters Definition in Computational Fluid Dynamics

3.2.3.1 Fluid Material type Setup

The classification of the required material zone can be set from a *Material panel* in

the CFD software from a *Database material list*, which has standard material parameters of both solid and fluid types, by selecting the proper item from the list. This list contains fluid materials that have been defined in the Materials panel. However, for more materials which undefined in that list it is simple to set the desired properties by setting the required materials with their parameters.

3.2.3.2 Fluid viscosity type setup

In incompressible Newtonian fluids, the viscosity is a function of the shear stress which is related to the rate-of-deformation tensor $\overline{\overline{D}}$, as following;

$$\overline{\overline{\tau}} = \mu \overline{\overline{D}} \tag{3.1}$$

where $\overline{\overline{\tau}}$ is the shear stress, μ is the viscosity which is independent of the rate-of-deformation tensor $\overline{\overline{D}}$.

the rate-of-deformation tensor $\overline{\overline{D}}$ is defined by

$$\overline{\overline{D}} = \left(\frac{\partial u_j}{\partial x_i} + \frac{\partial u_i}{\partial x_j} \right) \tag{3.2}$$

in some non-Newtonian fluids, the shear stress is given by;

$$\overline{\overline{\tau}} = \eta(\overline{\overline{D}})\overline{\overline{D}} \tag{3.3}$$

where η is the viscosity of non-Newtonian fluids.

Generally, η is a function of all three constants of the rate-of-deformation tensor $\overline{\overline{D}}$. On the other hand, in the non-Newtonian models that available in *FLUENT*, η is considered to be a function of the shear rate $\dot{\gamma}$ only, which related to the second constants of $\overline{\overline{D}}$ and is defined as;

$$\dot{\gamma} = \sqrt{\overline{\overline{D}} : \overline{\overline{D}}} \tag{3.4}$$

Various options for modelling different types of non-Newtonian fluids are provided by *FLUENT* software which listed as:

- Power law
- Carreau model for pseudo-plastics
- Cross model
- Herschel-Bulkley model for Bingham plastics. [97]

3.2.3.2.1 Power Law for Non-Newtonian Viscosity

The non-Newtonian power law model treats the fluid viscosity according to the following equation;

$$\eta = k\dot{\gamma}^{n-1} e^{T_0/T} \tag{3.5}$$

using this model, fluent provides to setup parameters for maximum and minimum viscosity values on the power law function, producing the following equation:

$$\eta_{\min} < \eta = k\dot{\gamma}^{n-1} e^{T_0/T} < \eta_{\max} \tag{3.6}$$

where k is non-Newtonian factor, n is the power-law index, T_0 is the reference temperature, $\eta_{\min}$ is the minimum viscosity value and $\eta_{\max}$ is the maximum viscosity value.

If the viscosity computed from the non-Newtonian power law is less than $\eta_{\min}$, the value of $\eta_{\min}$ will be used instead. Similarly, if the computed viscosity is greater than $\eta_{\max}$, the value of $\eta_{\max}$ will be used instead. Figure 3.1 shows how viscosity is limited by $\eta_{\min}$ and $\eta_{\max}$ at low and high shear rates according to non-Newtonian power-law model [98].

The value of n determines the group of the fluid as following:

- n = 1 Newtonian fluid
- n>1 shear-thickening (dilatant fluids)
- n<1 shear-thinning (pseudo-plastics)

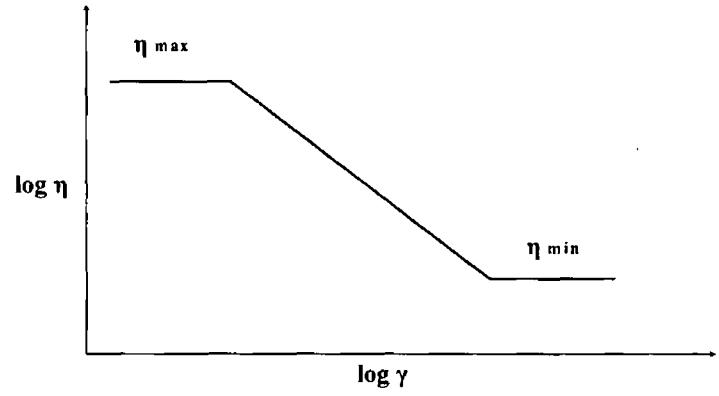

Figure 3. 1: Variation of viscosity with shear rate according to the non-Newtonian power law model

3.2.3.2.2 Herschel-Bulkley Model for Non-Newtonian Viscosity

Herschel-Bulkley model treats the material by combining the effect of Bingham behaviour and power-law behaviour in the fluid.

The concept of Bingham plastics are characterized by a non-zero shear stress when the strain rate is zero as following;

$$\bar{\bar{\tau}} = \bar{\bar{\tau}}_o + \eta \bar{\bar{D}} \tag{3.7}$$

where, τ_o is the yield stress which; for materials remains rigid is $\tau < \tau_o$ and for materials flows as a power-law fluid is $\tau > \tau_o$

at law shear rate ranges, the rigid materials acts as viscous fluid at μ_o, where

$$\dot{\gamma} < \left(\tau_o / \mu_o \right) \tag{3.8}$$

once the shear rate increases and yield stress threshold is approved, the fluid behaviour is described by the power-law as following;

$$\eta = \frac{\tau_o + k\left[\dot{\gamma}^n - \left(\tau_o / \mu_o\right)^n\right]}{\dot{\gamma}} \tag{3.9}$$

This equation is used by Herschel-Bulkley model to determine the fluid viscosity. In addition to the conversion behaviour between a flow and no-flow condition, the Herschel-Bulkley model is capable to exhibit a shear-thinning or shear-thickening behaviour depending on the value of power-law index. Figure 3.2 shows the variation of shear stress with shear rate according to the Herschel-Bulkley model [98].

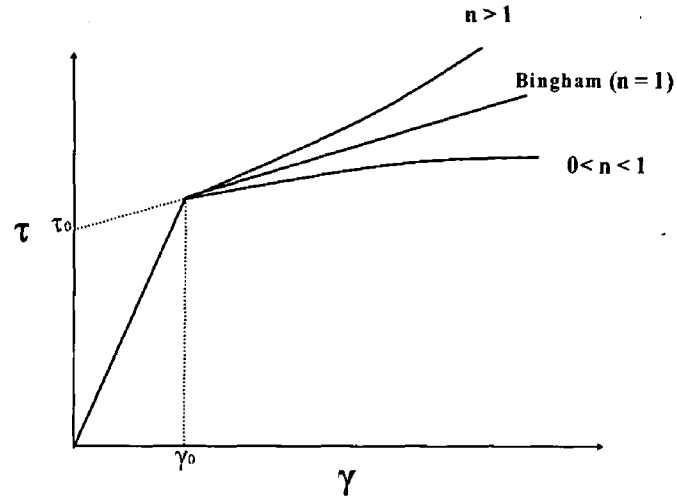

Figure 3. 2: Variation of shear stress with shear rate according to the Herschel-Bulkley model

3.2.3.3. Moving Zone Approach

The computational fluid dynamics provides a powerful set of facilities for solving cases that involve parts in motion. The CFD addresses these problems in two phases; first is flow in a single rotating frame, second is flow in multiple rotating frames. In the first case, the flow is unsteady, because the domain involves rotor/impeller blades that sweep the domain periodically. Nevertheless, in the absence of stators or baffles, it is possible to perform calculations in a domain that

moves with the rotating part. In this case, the flow is steady relative to the rotating frame, which simplifies the analysis [99], which equivalent to the case in this study where the moving surface is flat.

3.2.3.3.1 Rotation Axis setup

In the rotating zone and rotationally periodic boundaries adjacent to the fluid zone, it is essential to state the rotation axis. The rotation axis can be done by setting the *Rotation-Axis Direction* and *Rotation-Axis Origin*. This axis is independent of the axis of rotation used by any adjacent wall zones or any other cell zones. Within 2D-simulation problems; only the *Rotation-Axis Origin* needs to be specified; the axis of rotation is the *z*-direction vector passing through the specified point. In 3D-simulation problems, the axis of rotation is the vector from the *Rotation-Axis Origin* in the direction of the vector given by *Rotation-Axis Direction* inputs.

3.2.3.3.2 Zone Motion setup

From the *Moving Reference Frame* in the *Motion Type,* classifying the zone motion can be done for a rotating reference frame, by setting the appropriate parameters in the panel. In some cases, which include rotational motion, specifying the rotational *Speed* could be done under *Rotational Velocity*, where the rotation axis is defined as described above.

3.2.3.3.3 Analytical classification of the rotating surface in CFD

The equation for conservation of mass or continuity equation is given by;

$$\frac{\partial \rho}{\partial t} + \nabla.(\rho \vec{v}) = S_m \tag{3.10}$$

Equation (3.10) is the general form of the mass conservation equation. The source S_m is the mass added to the continuous phase and any user-defined sources.

The continuity equation for 2D axisymmetric geometries is given by:

$$\frac{\partial \rho}{\partial t} + \frac{\partial}{\partial x}(\rho v_x) + \frac{\partial}{\partial r}(\rho v_r) + \frac{\rho v_r}{r} = S_m \tag{3.11}$$

where x is the axial coordinate, r is the radial coordinate, v_x is the axial velocity, and v_r is the radial velocity.

Conservation of momentum in an inertial reference frame is illustrated by:

$$\frac{\partial}{\partial t}(\rho\vec{v}) + \nabla.(\rho\vec{v}\vec{v}) = -\nabla p + \nabla.(\bar{\bar{\tau}}) + \rho\vec{g} + \vec{F} \tag{3.12}$$

where p is the static pressure, $\bar{\bar{\tau}}$ is the stress tensor, $\rho\vec{g}$ and $\vec{F}$ are the gravitational body force and external body forces respectively.

The stress tensor $\bar{\bar{\tau}}$ is given by

$$\bar{\bar{\tau}} = \mu\left[(\nabla\vec{v} + \nabla\vec{v}^{T}) - \frac{2}{3}\nabla.\vec{v}I\right] \tag{3.13}$$

where μ is the molecular viscosity, I is the unit tensor, and the second term on the right hand side is the effect of volume dilation [100].

Once the equations of motion (3.10) are solved in a rotating frame, the acceleration of the fluid is increased by additional terms that appear in the momentum equations. Fluent provides a good facility to solve rotating frame problems by using either the absolute velocity or the relative velocity as the dependent variable.

The relation between the relative velocity and absolute velocity is given by;

$$\vec{v_r} = \vec{v} - (\vec{\Omega} \times \vec{r}) \tag{3.14}$$

where $\vec{v_r}$ is the relative velocity, $\vec{v}$ is the absolute velocity, $\vec{\Omega}$ is the angular velocity of the rotating frame and $\vec{r}$ is the position vector in the rotating frame.

for an inertial reference frame of the momentum equations (the left-hand side) is given by

$$\frac{\partial}{\partial t}(\rho\vec{v}) + \nabla.(\rho\vec{v}.\vec{v}) \tag{3.15}$$

the left-hand side for a rotating reference frame is given in terms of absolute velocities as;

$$\frac{\partial}{\partial t}(\rho\vec{v}) + \nabla.(\rho\vec{v_r}.\vec{v}) + \rho(\vec{\Omega}\times\vec{v}) \tag{3.16}$$

and in terms of relative velocities the left-hand side is given by;

$$\frac{\partial}{\partial t}(\rho\vec{v_r}) + \nabla.(\rho\vec{v_r}.\vec{v_r}) + \rho(2\vec{\Omega}\times\vec{v_r} + \vec{\Omega}\times\vec{\Omega}\times\vec{r}) + \rho\frac{\partial\vec{\Omega}}{\partial t}\times\vec{r} \tag{3.17}$$

where $\rho(2\vec{\Omega}\times\vec{v_r} + \vec{\Omega}\times\vec{\Omega}\times\vec{r})$ is the Coriolis force *(this force is used in rotating body problems, it is a pseudo-force that explains why bodies at the outer edge of a rotating disk experience higher linear speeds* [101]*)*.

In the flows of rotating domains, the equation for conservation of mass or continuity Equation (3.10); can be written for both the absolute and the relative velocity formulations as follows [102];

$$\frac{\partial\rho}{\partial t} + \nabla.(\rho\vec{v_r}) = S_m \tag{3.18}$$

3.2.3.4 The Concept of Pressure Equation in CFD

The momentum and continuity equations are solved sequentially. In this sequential procedure, the continuity equation is used as an equation for pressure. This procedure can be explained with presenting the Numerical Schemes that used in Fluent.

Fluent provides two numerical methods; segregated solver and coupled solver. By using any of theses solvers, Fluent deals with the governing integral equations for the conservation of mass and momentum. For both solvers; a control-volume-based technique is used as follows:

- Using the computational grid to divide the domain into discrete control volumes.
- Non-linear governing equations are linearized to produce a system of equations for the dependent variables (unknown variables such as velocities, pressure and temperature)in every computational cell
- The resultant linear system is then solved to yield an updated flow-field solution.

In both numerical methods, Fluent uses a similar discretization procedure, but different approaches are used to linearize and solve the discretized Equations [103].

The general solution procedures for *Segregated Solution Method* can be done as described above; by solution algorithm approach, the governing equations are solved sequentially. Before a converged solution is obtained, several iterations of the solution circle must be performed for the governing equations. The iteration of each case is illustrated by a flowchart in Figure 3.3 [104-105]. This solver provides The SIMPLE *(Semi-Implicit Method for Pressure-Linked Equations)* family of algorithms which is used for introducing pressure into the continuity equation.

3.2.3.5 Boundary Conditions Setup

Normally, it's not possible to run the simulation model without specifying the right boundary conditions, which identify the flow and the variables on the boundaries of the physical model. For this reason, there is a significant component within CFD for the simulations model which is important to be specified correctly. The main boundary conditions that are applied in the computational models of this study are:

- *Pressure inlet boundary conditions at the entrance of the gap (zero pressure kPa).*
- *Pressure outlet boundary conditions at the end of the gap (zero pressure kPa).*

- *Stationary wall boundary conditions (along the inserts wall).*
- *Moving rotating wall Boundary Conditions (along the rotating shaft with speed range of 0.5 to 1.5 m.sec^{-1}).*

3.2.3.5.1 Description of Pressure inlet boundary conditions performance

The pressure inlet boundary condition is used to define the fluid pressure at flow inlet along with all other scalar properties of the flow. They are suitable for both incompressible and compressible flow calculations [106]. The behaviour of pressure inlet boundary condition can be explained as a loss-free transition from stagnation conditions to the inlet conditions. Fluent uses this boundary condition as the total pressure of the fluid at the inlet plane, p_0. For incompressible fluids flow, the inlet total pressure and the static pressure p_s, are related to the inlet velocity by the Bernoulli's equation as following:

$$p_0 = p_s + \frac{1}{2}\rho v^2 \tag{3.19}$$

The velocity components can be computed from the obtaining velocity magnitude and the flow direction vector that assigned at the inlet, the inlet mass flow rate and fluxes of momentum can then be computed.

For incompressible flows, total temperature is equal to static temperature, and density at the inlet plane is either constant or calculated as a function of temperature and/or species mass fractions, where the mass fractions are the values that entered as an inlet condition. If flow exits through a pressure inlet, the total pressure specified is used as the static pressure for incompressible flows [107].

3.2.3.5.2 Description of Pressure outlet boundary conditions performance

Pressure outlet boundary condition requires the specification of a static pressure at the outlet boundary [108]. In this condition; *FLUENT* uses the boundary condition of the pressure which was input as the static pressure of the fluid at the outlet plane, p_s and extrapolates all other conditions from the interior of the fluid domain [109].

3.2.3.5.3 Wall conditions performance

A wall type boundary is used to bound fluid and solid regions together. In viscous fluid flows, the no-slip boundary condition is forced at walls by default, although it is possible to specify a desired velocity component for a moving wall surface in wall boundary terms of the translational or rotational motion, or model a slip wall by specifying shear. The shear stress between the fluid and wall are computed based on the flow details in the domain [110].

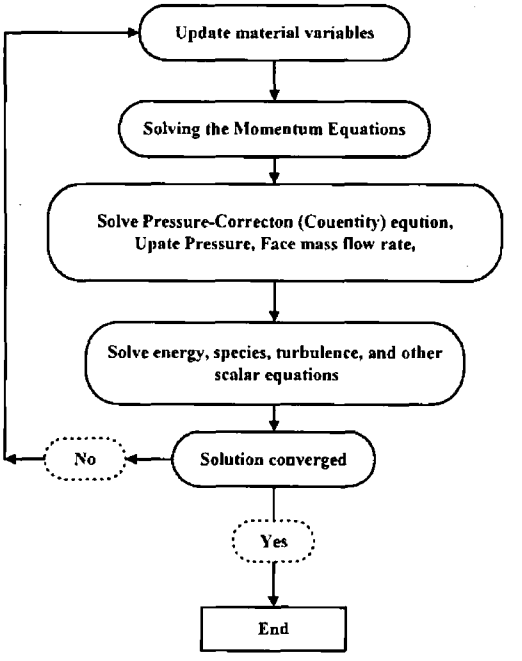

Figure 3. 3: Flowchart of the Segregated Solution Method [107]

3.2.4 The Design of the computational-simulation model

Two dimensional models have been built to simulate the experimental models of the plasto-hydrodynamic unit for various converging gaps involving a rotating shaft surface.

In these models the designs are constructed based on edge zone method, where each surface of the unit gap was defined by a proper edge type inside *Gambit*

software to specify the boundary type's zone. The viscous fluid domain is created as surface zone approach and defined by continuum type's zone. All regions within the process are built in a suitable solver type.

By selecting *FLUENT/UNS* solver in *Gambit*, six various edges were created to represent the converging gaps, then they were united together to present the viscous fluid domain for each case of the five models. To specify the boundary type's zones; the stationary surfaces *(insert-1, insert-2 and the step and others)* and moving shaft surface were defined as edge wall boundary conditions. The start-flow field at the gap entrance was set as an edge pressure-inlet boundary condition and the end-flow field of the gap was situated as an edge pressure-outlet boundary condition. The region of the viscous fluid domain was applied as fluid continuum zone. Meshing the model was done with various sizes into the solver to create the grid elements all over the process area. The mesh was applied in quadrilaterals elements grid shapes and tested until the fine mesh results were satisfied. Figure 3.4 shows a simple of the grid amounts that applied to at the gap entrance field in the 2D- computational model.

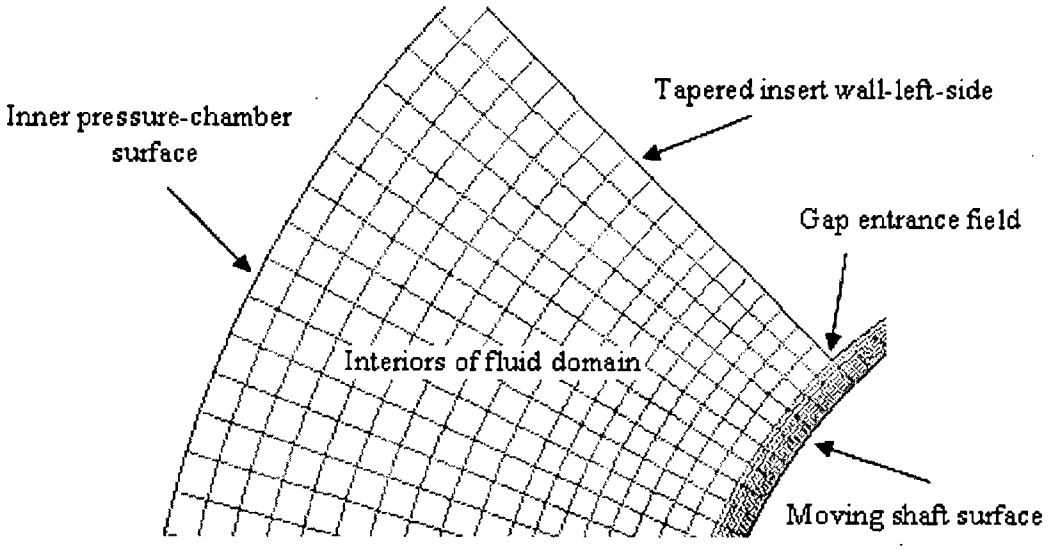

Figure 3. 4: Grid system at the entrance of the converging gap in the 2D- computational model

3.2.5 Running the simulations model and their procedures process setup

3.2.5.1 Applying the model

The simulations models were built in the Gambit software with their boundary conditions classifications and fine grids. The essential step of the process procedures is the exportation of mesh file *(MSH)*, which allows the created geometry to run the model within the fluent software. After building the geometries and their requirements as mentioned above, the models must be imported to Fluent as a case file. These procedures are very important in CFD tools, and must be followed in all cases to run the models.

After exporting the file in fluent, the grid needs to be checked. The boundary conditions can be modified and changed to various options to suit the process requirement. The materials of the process and other properties need to be specified.

To run the computational models, several assumptions have been considered to solve the problem based on non-Newtonian characteristics as following:

- The change in temperature is constant.
- Flow of viscous fluid within the unit is laminar and steady.
- Fluid layers within the gap are small comparing to total dimension of the rotating unit.

3.2.5.2 Solution Strategies of the rotating process

As illustrated in the fluent theories [111-112], the complexities related with solving rotating reference frames are a result of the high degree of coupling between the momentum equations. This situation begins when the effect of the rotational conditions is large. Presenting a high level of rotation brings a large radial pressure gradient. This pressure gradient makes the fluid flow in both; axial and radial directions, which setting up a distribution of the rotation term in the field. The

coupling technique could guide to instabilities in the solution process, therefore, special solution techniques are required to obtain a converged solution. Some of the solution requirements need to be considered to solve the model for (Segregated solver) as follows:

1. The velocity type within the model.
2. Using the PRESTO Scheme, which is well-suited for the steep pressure gradients involved in rotating flows.
3. Ensure that the mesh is sufficiently refined to resolve large gradients in pressure.
4. Reduce the under-relaxation factors for the velocities if necessary.
5. If necessary, start the calculations using a low rotational speed.

3.2.5.3 Post-processing of the rotating frame process

In solving a rotating reference frame, several plot schemes and reports can be obtained for the model such as absolute and relative velocities. For all velocity parameters, corresponding relative values are available for post-processing. The relative variable are also available for post-processing of total pressure, total temperature and any other variables include a dynamic contribution dependent on the reference frame [113]. The results that obtained are presented in next chapter. Flow-chart in Figure 3.5 shows the Computational simulation plane and its solutions procedures.

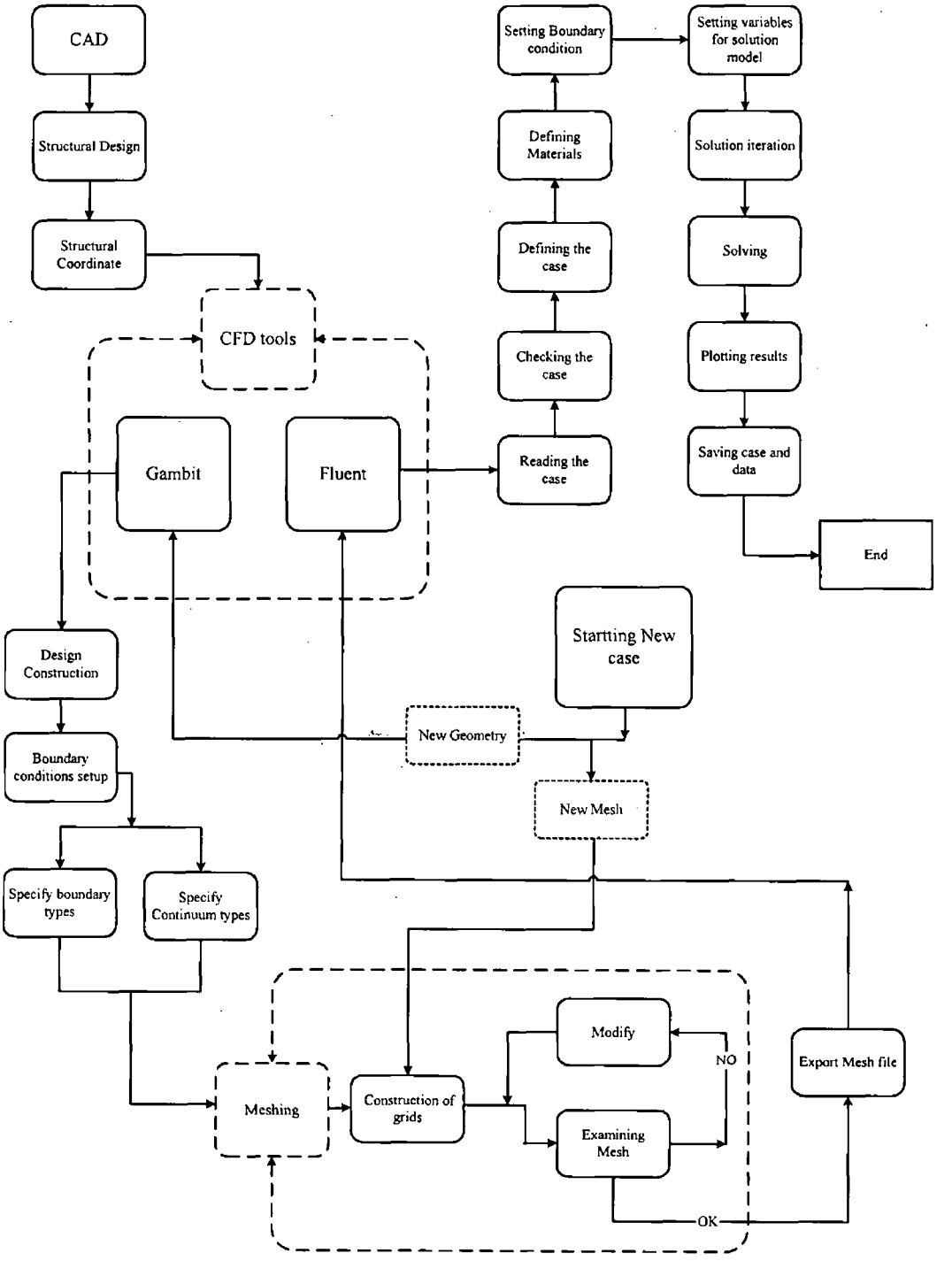

Figure 3. 5: Flow-chart of the Computational simulation plane and its solutions procedures

Chapter Four

Results and Discussions

4.1 Experimental Results

4.1.1 Viscosity Experimental results

The viscosity of the polymer melts changes during the wire drawing process. The change of shearing velocity within the process could be a significant reason for the variety of polymer melt viscosities.

Measurement of the three viscous fluid viscosities in laboratory was done under atmospheric pressure by a Cone-plate type Brookfield viscometer. Because of the limitation of the viscometer measurements, the fluid viscosities are obtained at low shear rate ranges, which can not show any significant change in the fluids viscosities, while the change in viscosity might occur at higher shear rate range. Figures 4.1, 4.2 and 4.3 show the relation of shear rate versus shear stress as obtained by the cone-plate viscometer. It can be noticed that, the viscosity for all fluids show a Newtonian behaviour at lower shear rate range.

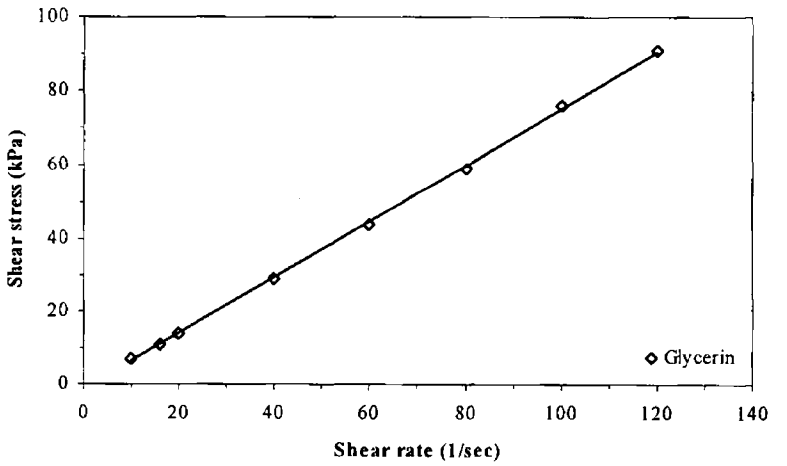

Figure 4. 1: Shear rate versus shear stress for Glycerine by Cone-plate Brookfield viscometer

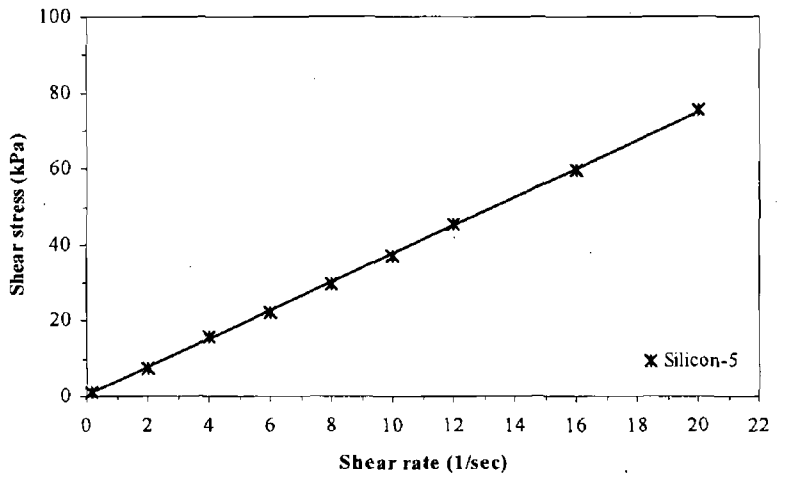

Figure 4. 2: Shear rate versus shear stress for Silicone-5 by Cone-plate Brookfield viscometer

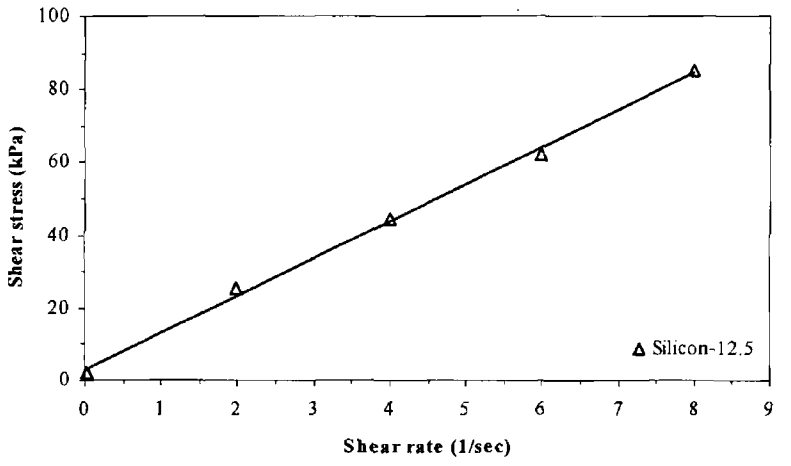

Figure 4. 3: Shear rate versus shear stress for Silicone-12.5 by Cone-plate Brookfield viscometer

4.1.2 Pressure Distribution of Experimental Results

It is well known, in plasto-hydrodynamic wire drawing and coating techniques, that the wire is dipped into a bath of polymer melt and pulled through either a conical or cylindrical bore. When the wire moves, it drags the polymer melt into the orifice which develops pressure between the wire surface and the inner die surface by

means of hydrodynamic action. Similar circumstances occur in the rotating shaft plasto-hydrodynamic pressure unit, where the surface of the rotating shaft drags the viscous fluid in the gap between the inserts and the rotating shaft which gives rise to the hydrodynamic pressure. The magnitude of pressure gradient depends on various parameters such as the rotating shaft speed, viscosity of the viscous fluid and the geometrical features of the bore. The hydrodynamic pressure initiates with zero pressure at the die entrance and rises to reach the highest level near the step at the end of the tapered zone. The pressure profile moves up non-linearly in the tapered zone area then it decrease linearly in the parallel bore zone to leave the die at zero pressure at the end of the parallel bore. The magnitude of the pressure depends on various parameters such as the geometrical shape of the die, shaft speed, fluid temperature, and the fluid viscosity. All these parameters affect the hydrodynamic pressure somehow or other.

A number of experimental works were carried out to determine the pressure distribution within the die for different shaft speeds and geometrical parameters of the radial gaps in the pressure unit in terms of gap ratios and shear rate. The plasto-hydrodynamic rotating unit that used was built based on the conception of a tapered-stepped-parallel pressure die in the wire drawing technique, the results were obtained for three different types of fluids and the tests were repeated at least six times for each shaft speed and gap ratio. Based on the fluid type and the rotating shaft speeds in each case, the results are presented as following;

4.1.2.1 Pressure Distribution results for Glycerine

By using Glycerine as a pressure medium in the process at temperature varying from zero to 18 °C, the results of the experimental work obtained are presented in terms of drawing speed and pressure distribution for various gap ratios (h_1/h_2) of the dies. These results exhibited similar trends with slight differences as the gap ratios and shaft speed were altered. Figures 4.4, 4.5, 4.6, 4.7 and 4.8 show the relation of pressure versus die distance at various gap ratios and different speeds. The experimental tests were obtained at shaft speed of 0.5, 1.0 and 1.5 meter per second respectively.

Figure 4.4 shows the experimental tests for gap ratio of (0.9/0.3) at different speeds, when the shaft rotates, the pressure generates and starts at zero pressure at the entry of the die and increases. The pressure profile behaves non-linearly in the tapered bore zone and linearly in the parallel bore zone. A curved line is extended from the second point of pressure transducer *(by using curve fitting in the Excel program)* to meet an extended straight line at the step, the pressure profile between the step and the second transducer was predicted, the extended straight line was created from the end of the bore where the end pressure equals to zero to meet the point of the third transducer which was extended from the third pressure transducer to the step [90]. For a shaft speed of 0.5 $m.sec^{-1}$ the pressure profile starts at zero then develops to 279 kPa at the middle of the tapered bore to reach 412 kPa at the second pressure transducer, the pressure reaches the highest amount near the step because of the geometry. When it leaves the step and enters the parallel bore it drops down linearly to 238 kPa at the middle of the parallel bore then goes down to leave the die at zero kPa. It is obvious that the pressure profile in the tapered bore has a non-linear relationship with the distance of the die and it is linear in the parallel bore area. The same situation occurs at 1.0 $m.sec^{-1}$ and 1.5 $m.sec^{-1}$, except that the pressure gradient is much higher at each transducer than the first test where it reaches 742 kPa at the second transducer for a shaft speed of 1.0 $m.sec^{-1}$ and 897 kPa at 1.5 $m.sec^{-1}$ speed of shaft.

It is obvious that the increase in the inlet gap reduces the pressure in the bore, in comparison to Figure 4.4 and 4.5, where both dies have the same tapered outlet radial gap and different inlet radial gap, the pressure profile for the smallest inlet gap (0.9/0.3) is much higher than that for the greater inlet.

The results of experimental tests obtained, have slightly different pressure gradients for die gap ratios of (0.9/0.3), (1.0/0.5), (1.2/0.3), and (1.5/0.5) as showing in Figures-4.4, 4.5, 4.7 and 4.8. But as shown in Figure 4.6 the die with a gap ratio of (1.5/0.3) has much less hydrodynamic pressure gradient and somewhat different characteristics, which at 1.5 $m.sec^{-1}$ has the highest magnitude between the distance of 20mm and 30mm in the tapered zone. At a speed of $m.sec^{-1}$, the

pressure gradient develops non-linearly, which increases to 191 kPa at the first transducer and goes up to reach 215 kPa at the second pressure transducer. At this point the pressure generated remains nearly steady with no significant change until the step, and then it drops down after the step to leave the bore at zero kPa. Hydrodynamic pressure profiles for shaft speeds of 1.0 m.sec^{-1} and 1.5 m.sec^{-1} show different trend than for 0.5 m.sec^{-1}.

The pressure profile results in all gaps for Glycerine, exhibited similar trends with slight difference as the gap ratios and speeds were altered [114].

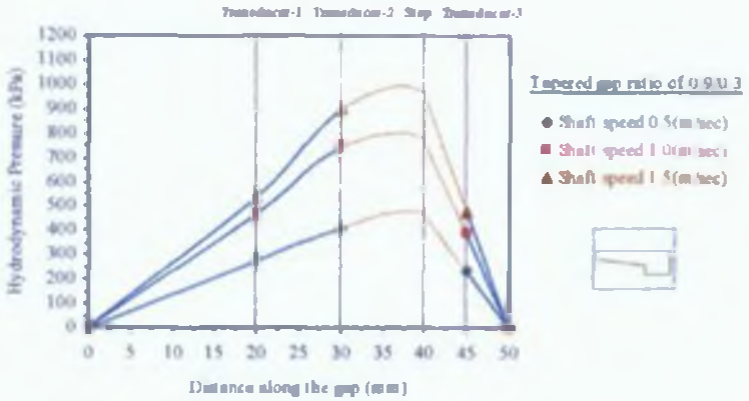

Figure 4. 4: Pressure distribution for *Glycerine* within gap ratio of *(h_1/h_2=0.9/0.3)*

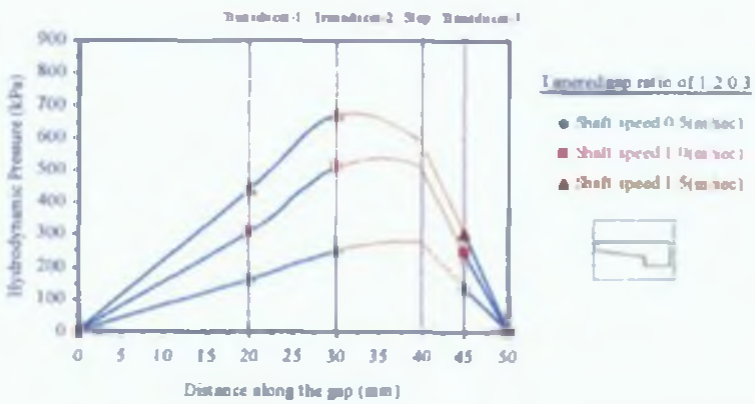

Figure 4. 5: Pressure distribution for *Glycerine* within gap ratio of *(h_1/h_2=1.2/0.3)*

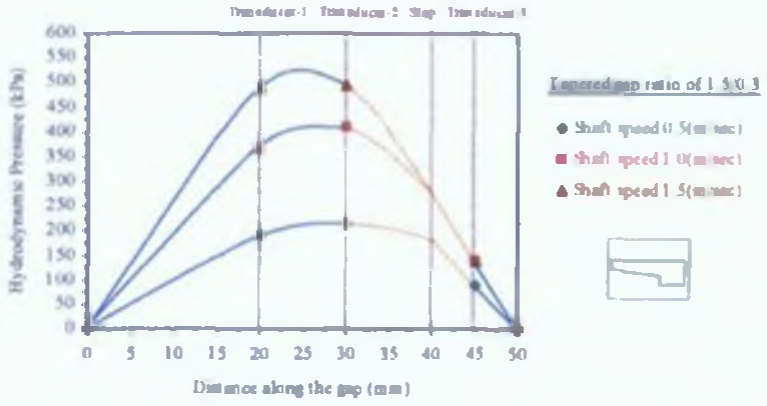

Figure 4. 6: Pressure distribution for *Glycerine* within gap ratio of $(h_1/h_2 = 1.5/0.3)$

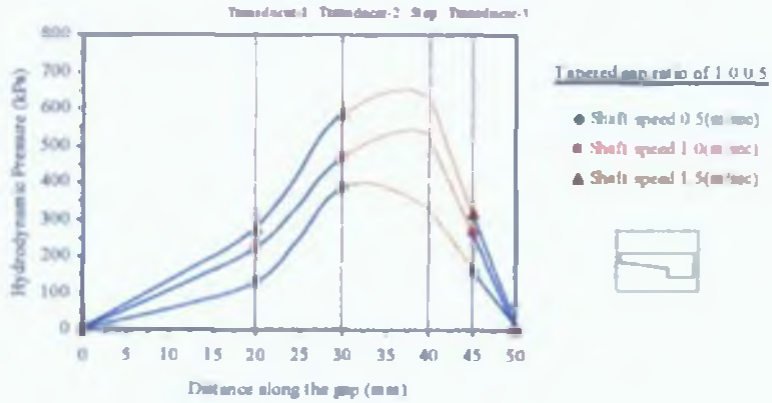

Figure 4. 7: Pressure distribution for *Glycerine* within gap ratio of $(h_1/h_2 = 1.0/0.5)$

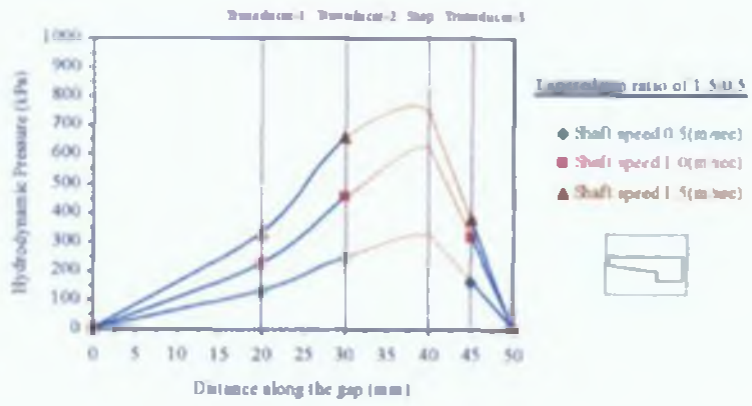

Figure 4. 8: Pressure distribution for *Glycerine* within gap ratio of $(h_1/h_2 = 1.5/0.5)$

4.1.2.2 Experimental results of Silicone-5

The process for Silicone-5 was done at temperature varying from zero to 25 °C. The obtained results exhibited similar trends with slight differences as the shaft speed and the gap ratios altered. These experimental tests were obtained at shaft speeds of 0.5, 1.0 and 1.5 meter per second. Figures 4.9, 4.10, 4.11, 4.12 and 4.13 show the relation of pressure versus the distance along the die for Silicone-5 through the converging gaps.

Figure 4.9 shows the results of experimental tests carried out for three different shaft speeds within the gap ratio of (0.9/0.3), where the initial pressure for all speeds is zero. The same method was used to connect the pressure profile points together via the step point as described above. While the shaft rotates, its surface drags the viscous fluid into the gap and hydrodynamic pressure is generated. The pressure starts at zero and develops nonlinearly in the tapered zone, and linearly in the parallel zone. In Figure 4.9 for a shaft speed of 0.5 $m.sec^{-1}$, the pressure profile starts at zero then develops to reach 637 kPa in the middle of the tapered part to reach 930 kPa at the second pressure sensor. The pressure reaches the highest level to 1000 kPa at the step, and then it drops linearly to 504 kPa at the middle of the parallel zone to leave the die at zero pressure. For a shaft speed of 1.0 $m.sec^{-1}$, the pressure generates nonlinearly as well in the tapered area. The pressure develops to reach 1044 kPa at the first transducer and 1430 kPa at the second transducer which is the highest magnitude for the pressure profile in the bore, it then begins to decrease in the last third zone of the tapered area to reach 670 kPa and drops linearly to 340 kPa at the middle of the parallel bore, then leaves the die at zero pressure. The pressure develops very high before the step and it behaves differ to the shaft speed of 0.5 $m.sec^{-1}$.

For gap ratios of (1.2/0.3) and (1.5/0.3), the hydrodynamic pressure has the highest magnitude at the second transducer for a shaft speed of 0.5 $m.sec^{-1}$ for both dies as shown in Figures 4.10 and 4.11. Figure 4.11 shows that the pressure in the parallel bore is negligible for the shaft speeds of 1.0 and 1.5 $m.sec^{-1}$ for the die gap ratio of (1.5/0.3).

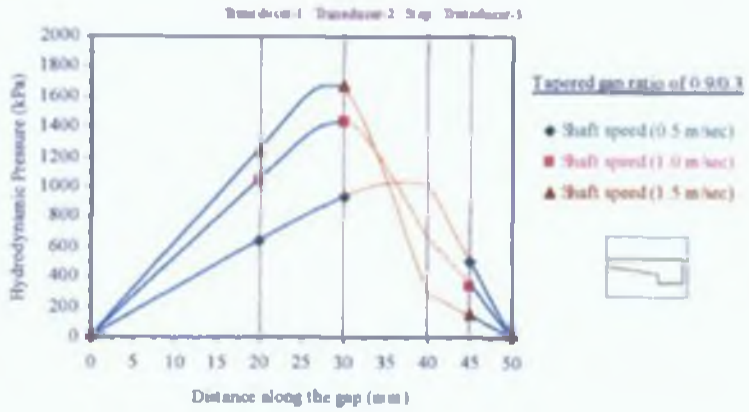

Figure 4. 9: Pressure distribution for *Silicone-5* within gap ratio of $(h_1/h_2 = 0.9/0.3)$

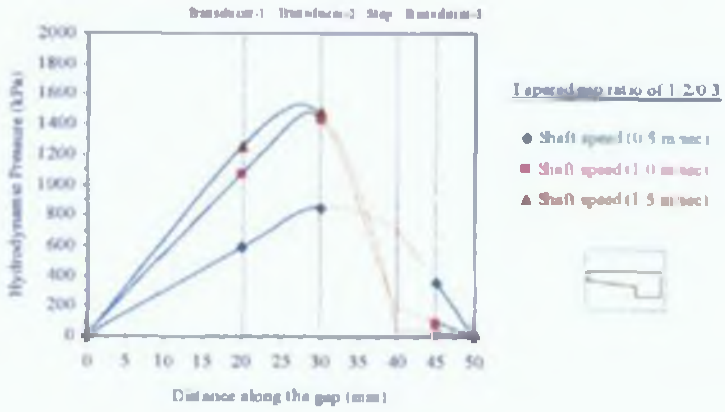

Figure 4. 10: Pressure distribution for *Silicone-5* within gap ratio of $(h_1/h_2 = 1.2/0.3)$

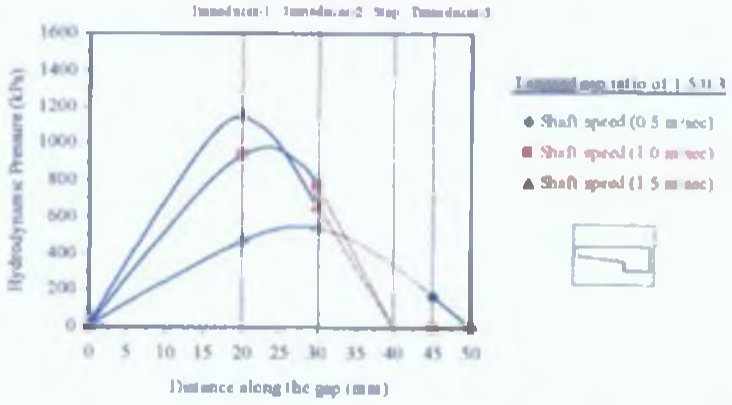

Figure 4. 11: Pressure distribution for *Silicone-5* within gap ratio of $(h_1/h_2 = 1.5/0.3)$

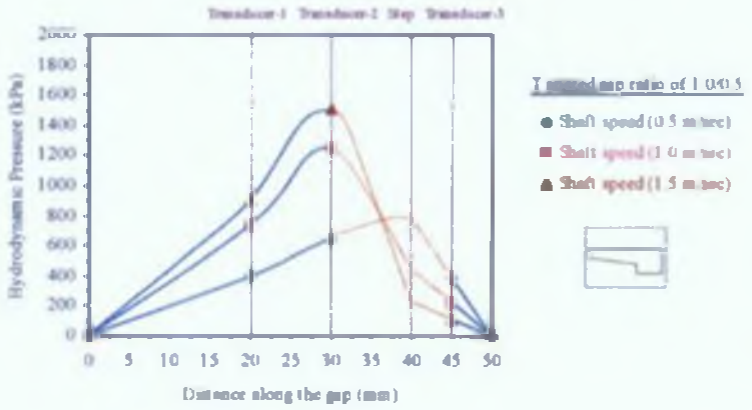

Figure 4. 12: Pressure distribution for *Silicone-5* within gap ratio of *(h_1/h_2 - 1.0/0.5)*

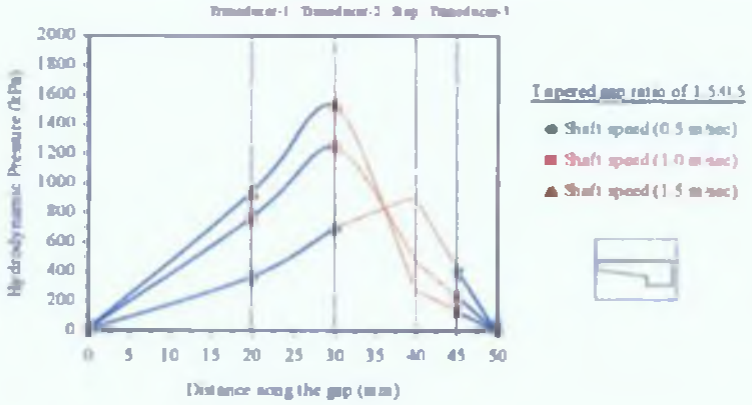

Figure 4. 13: Pressure distribution for *Silicone-5* within gap ratio of *(h_1/h_2 = 1.5/0.5)*

All results for Silicone-5, showed similar trends with insignificant differences as the gap ratios and shaft speeds are altered as the figures illustrated, especially in the first three profiles for gap ratios of (0.9/0.3), (1.0/0.5), and (1.5/0.5), but as it shown in Figure 4.11, the die with a gap ratio of (1.5/0.3) has a less amount of hydrodynamic pressure gradient, and somewhat different characteristics which at 1.0 and 1.5 m.sec^{-1}has the highest magnitude at the first transducer in the middle of the tapered zone. This shows an opposite behaviour of pressure profile in the tapered zone compared to other four gap ratios. At a speed of 0.5 m.sec^{-1}, the pressure gradient develops non-linearly, which increases to 468 kPa at the first transducer and develops to reach 537 kPa at the second pressure transducer. At this stage the pressure drops down smoothly until the step, and then it drops down after the step to leave the bore at zero pressure. Hydrodynamic pressure profiles for shaft

speeds of 1.0 m.sec^{-1} and 1.5 m.sec^{-1} show different trend than for 0.5 m.sec^{-1}, where they have negligible hydrodynamic pressure in the parallel zone. Even with the altering the radial gaps, the hydrodynamic pressure trends to have nearly the same pressure profile behaviour in the tapered zone area for all speeds within the gaps except the gap ratio of (1.5/0.3) [115].

For all experimental tests using Silicone-5 as pressure medium, almost similar trends of the pressure distribution are observed for various gap ratios; the difference is that the overall gap ratio affects the magnitude of the pressure generated. An increase in the inlet gap may cause back flow of the viscous fluid which causes the reduction of pressure in the parallel part of the unit.

4.1.2.3 Experimental results of Silicone-12.5

The experiential works that applied using Silicone12.5 as a viscous fluid to present a pressure medium of the process have been done from zero to 25 °C. The obtained results exhibited similar trends with slight differences of pressure gradients in comparison with the first two cases *(Glycerine and Silicone-5)*. The results were obtained within all gap ratios, as the shaft speeds and the gap ratios changed. These experimental tests were achieved at shaft speeds of 0.5, 1.0 and 1.5 meter per second. Figures 4.14, 4.15, 4.16, 4.17 and 4.18 show the pressure distribution profiles at three locations along the gap for a number of dies with various gap ratios. The same method was used to connect the pressure profile points together via the step point as described above. The pressure profiles for (0.9/0.3), (1.0/0.5) and (1.5/0.5) gap ratios are showing similar trends with a variety of pressure magnitudes, where the pressure values is higher in the tapered zone rather than the parallel zone. The pressure amount is higher within the tapered zone at any time speeds were increased. Nearly all figures shown that, the pressure at the second transducer within the tapered bore is higher than the first transducer. It is obvious that the hydrodynamic pressure drops down in the parallel bore, where the amount of the pressure are very small comparing to its level in the tapered zone, especially for the shaft speed of 1.0 and 1.5 m.sec^{-1}. In the other hand, the profiles show that for 0.5 m.sec^{-1} shaft speed, the magnitude of the pressure higher than it for the other two speeds, and the

differences between the pressure profiles in the parallel zone can be noticed; that at the higher shaft speeds, a lesser amount of pressure magnitudes were obtained.

In Figure 4.15, relatively dissimilar pressure profiles have been obtained for gap ratio of (1.2/0.3), where the higher pressure within the tapered bore for the shaft speed of 1.5 m.sec^{-1} is observed at the first transducer *(which is 1696 kPa and at the second transducer is 1664* kPa), which vary with the other two profiles behaviour of 0.5 and 1.0 m.sec^{-1} shaft speed. In this tapered gap; since the speed increased, the pressure in the second half of the bore decreases which can be noticed as the figure shows. However, the pressure profiles in the parallel zone exhibit similar trends with the other three gaps that mentioned before except for speed of 0.5 m.sec^{-1}, which shows a slight higher amount of hydrodynamic pressure and closer to the pressure profiles for the other two speeds.

The die with (1.5/0.3) gap ratio, shows a completely different pressure behaviour within the tapered bore comparing to all other gap ratios; where for all shaft speeds the highest amount are obtained at the first pressure transducers, as it shown in Figure 4.16; the highest amount of hydrodynamic pressure (1708 kPa) is observed at the higher speed (1.5 m.sec^{-1}), the smallest (907 kPa) at the lower shaft speed (0.5 m.sec^{-1}), and so on. Not the same trend could be noticed in this gap, where at the second pressure point sensor; the higher rotating speed develops a lesser amount of pressure (565 kPa) within the tapered bore, the lower shaft speed produced higher pressure magnitude (726 kPa) and the highest pressure magnitude was obtained at shaft speed of 1.0 m.sec^{-1}.

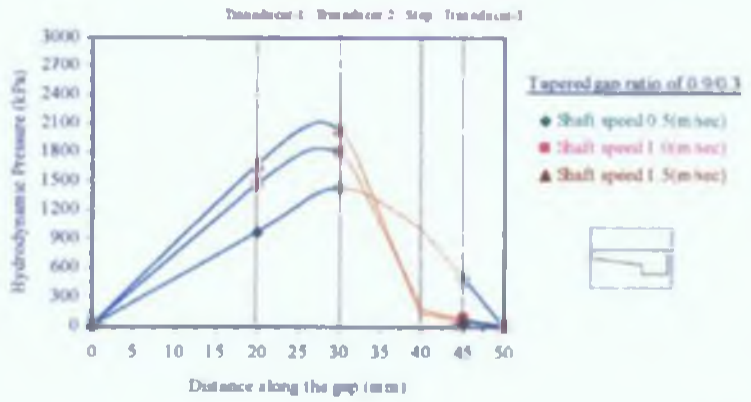

Figure 4. 14: Pressure distribution for *Silicone-12.5* within gap ratio of *(h_1/h_2=0.9/0.3)*

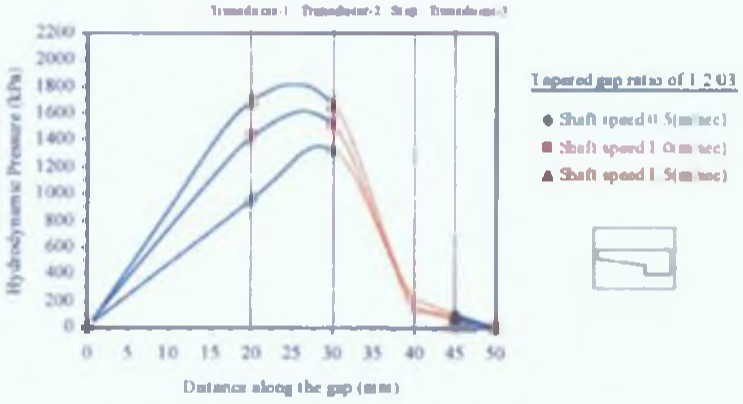

Figure 4. 15: Pressure distribution for *Silicone-12.5* within gap ratio of *(h_1/h_2=1.2/0.3)*

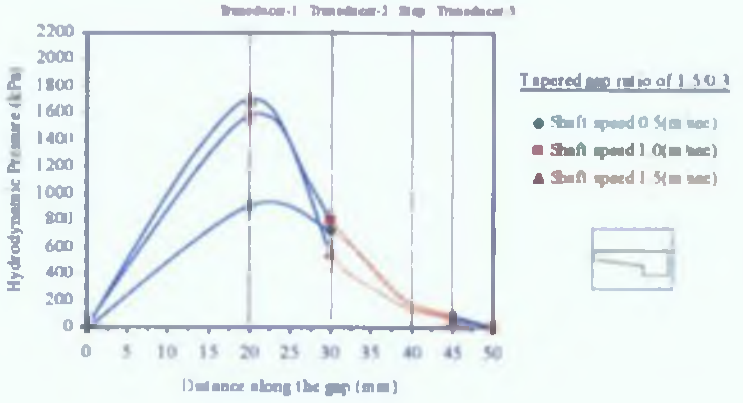

Figure 4. 16: Pressure distribution for *Silicone-12.5* within gap ratio of *(h_1/h_2=1.5/0.3)*

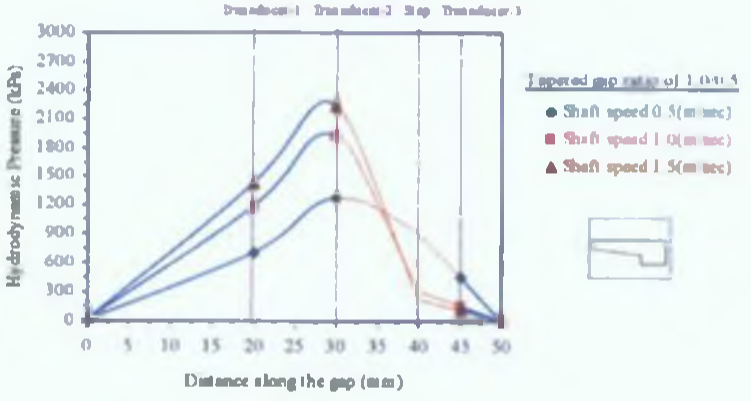

Figure 4. 17: Pressure distribution for *Silicone-12.5* within gap ratio of *(h_1/h_2=1.0/0.5)*

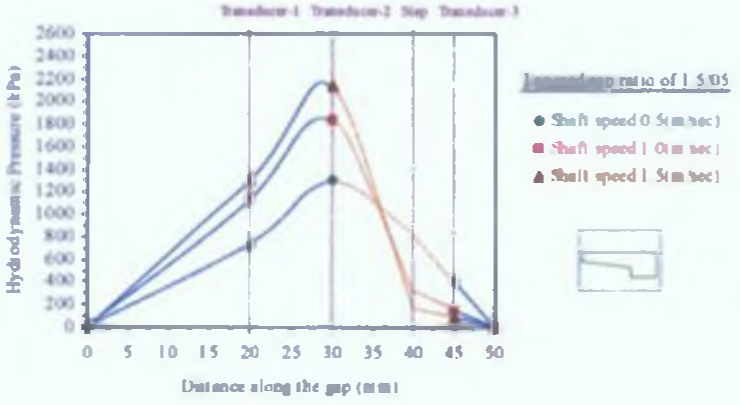

Figure 4. 18: Pressure distribution for *Silicone-12.5* within gap ratio of *(h_1/h_2=1.5/0.5)*

4.2 Computational Simulation results

A number of computational simulation models have been studied to determine the pressure distribution within the models for various rotating wall speeds *(rotating shaft)* and various simulated radial gaps in terms of conjunction grid system and moving wall by using the computational fluid dynamics. Based on the notion of the plasto-hydrodynamic rotating unit, the converging gaps were created in 2D models. In these models; the results are obtained for three different types of viscous fluids that used in the experimental work and presented as following;

4.2.1 Computing velocity vector profiles

Since the specification of the boundary conditions of the model and the movement of the rotating wall are specified, the CFD can solve the problems based on the model parameters, which after several solution iterations; the velocity vector presents the magnitudes and the directions of the applied velocity profile on the moving wall and velocity fluid layers within the interior domain.

Figure 4.19 shows the velocity vector of fluid domain around the entrance of the gap as the arrows show the directions of the fluid layers and its velocity magnitudes. It is obvious that the fluid layers have the highest velocity magnitude near the moving wall and its decrease towards the stationary wall. On the other hand, a back flow can be noticed coming from inside the gap which caused by the

step wall. Where the fluid elements hit the step wall which makes the fluid layers beside insert-1 reserve their motion direction along the wall, as well flow back can be seen in the fluid domain before the gap. For all rotating wall speeds; every single model is exhibited similar velocity vector movement for all models for three viscous fluids, the magnitude differences are dependent on the applied amount of the rotating wall speed.

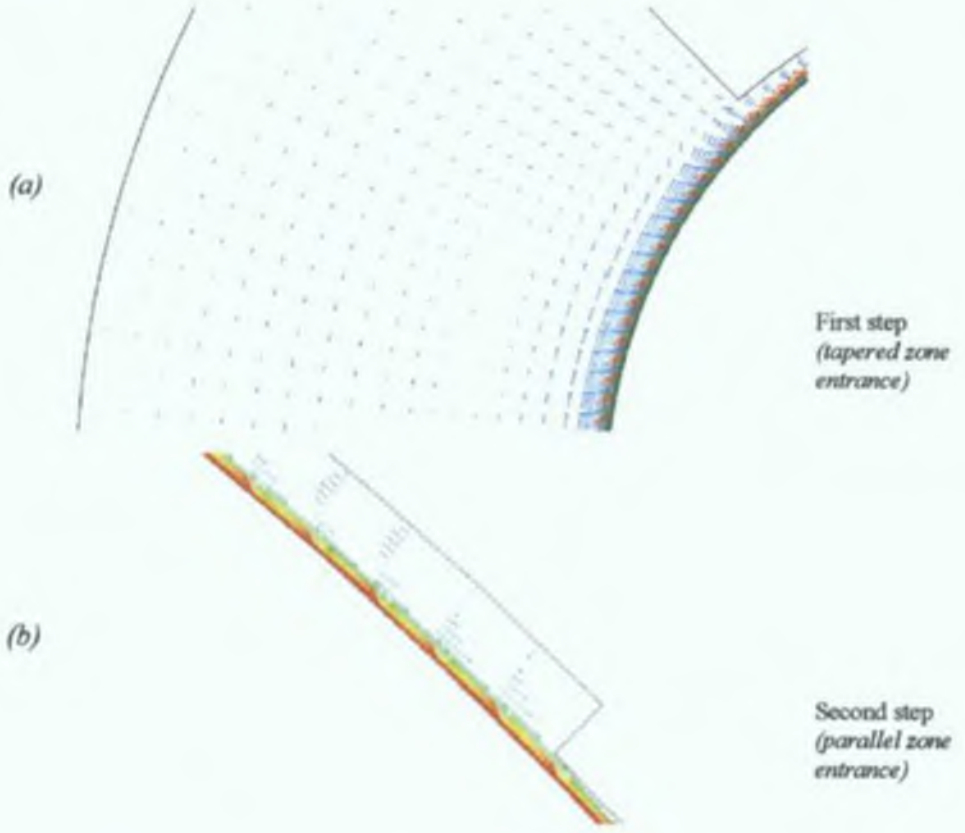

Figure 4. 19: Velocity Vector of the fluid domain around the gap entrance and the step at rotating wall speed of $0.5\ m.sec^{-1}$

4.2.2 Computational Viscosities

Experimentally, the change in fluid viscosity within the process was not possible to obtain at the high shear rate ranges by using the cone-plate viscometer. Therefore, it was a benefit to discover it within the computational model at higher shear rates. To employ the non-Newtonian power law model within the CFD, several variables should be defined which are;

- Non-Newtonian factor *(k)*
- Power-law index *(n)*
- Minimum viscosity value μ_o
- Maximum viscosity value μ

since these constants were not possible to obtain experimentally, the suggestion was to apply the variables that obtained by previous researchers for each fluid. Table 4.1 shows the non-Newtonian-power law constants for all viscous fluids are used in this study [85];

Table 4. 1: Non-Newtonian-power law parameters

Viscous fluid	Non-Newtonian factor	Power law index	Minimum viscosity (Pa.sec)	Maximum viscosity (Pa.sec)
Glycerine	7.36	0.75	1	6
Silicone-5	1634	0.234	3	13
Silicone-12.5	7855	0.12	6	24

By applying these constants in the non-Newtonian power-law model, the viscosity profiles were obtained for each viscous fluid at high shear rate ranges within all gaps. For each fluid, the profiles showed similar performance within the gaps. Figures 4.20, 4.21, and 4.22 show examples of the viscosity profiles that obtained by non-Newtonian power-law model for each viscous fluid.

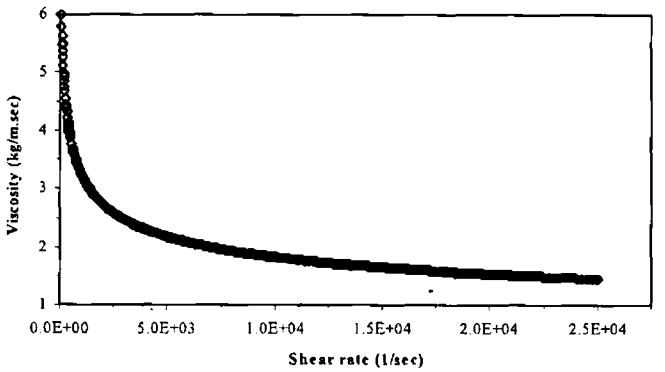

Figure 4. 20: Viscosity versus shear rate based on non-Newtonian- power law model for *Glycerine* within *(0.9/0.3)* gap ratio

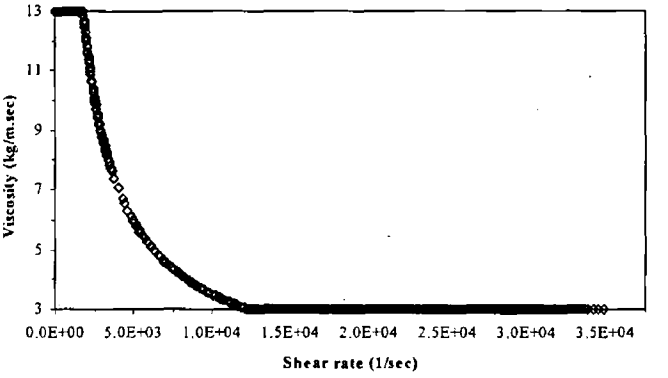

Figure 4. 21: Viscosity versus shear rate based on non-Newtonian- power law model for *Silicone-5* within *(0.9/0.3)* gap ratio

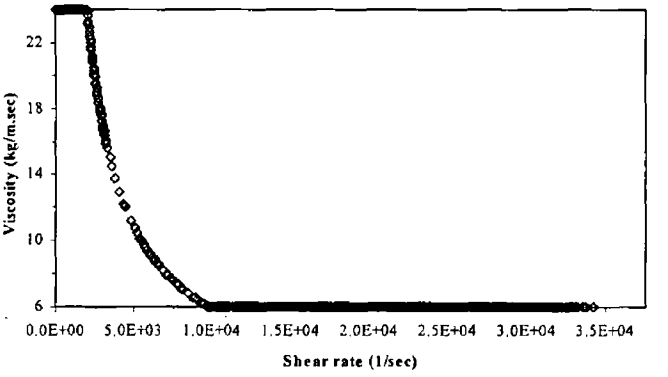

Figure 4. 22: Viscosity versus shear rate based on non-Newtonian- power law model for *Silicone-12.5* within *(0.9/0.3) gap ratio*

The profiles for Silicone-5 and Silicone12.5 show a constant magnitude of viscosities at the minimum limits that applied which starts at a cretin shear rate ($12x10^4$ sec^{-1}) for Silico-5 fluid and (9.5 $x10^4$ sec^{-1}) for Silicone-12.5. Thus, the non-Newtonian power law model does not present the whole range of viscosity changes which remains to be constant at the minimum magnitudes even with higher shear rates because the power law model uses the applied minimum value of viscosity even if the fluid viscosity is below this amount [102].

By applying the non-Newtonian approach of Herschel-Bulkley model [98], the full range of change in the viscosity is obtained at higher shear rates and the profiles showed better performances, where the Herschel-Bulkley model combines

the effects of Bingham and power-law behaviour in a fluid. The Bingham behaviour is characterized by a non-zero shear stress when the strain rate is zero.

The Herschel-Bulkley model requires the yield stress entry of the fluid to be defined, in which the fluid at a specific amount of shear stress starts to flow. This amount of the shear stress is known as the critical shear stress. Therefore, the yield stress was obtained for each viscous fluid within the non-Newtonian power-law model from a plot of the shear stress versus shear rate relation. Figures 4.23, 4.24 and 4.25 show the shear rate shear stress relation for each viscous fluid. As shown in Figure 4.23, the yielding stress for Glycerine was obtained at $\approx$ 90 sec^{-1} shear rate because its molecular viscosity is too small comparing to other two fluids.

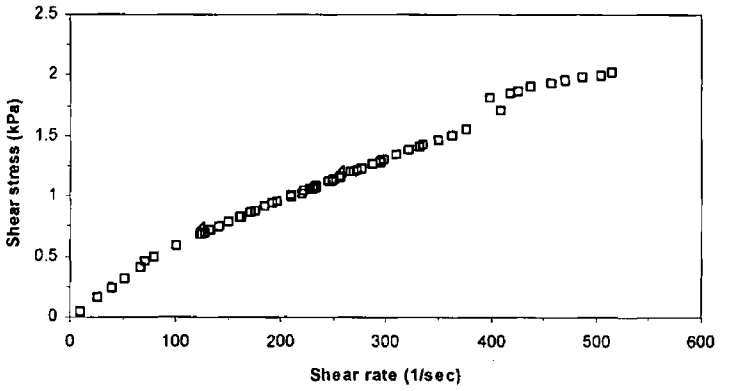

Figure 4. 23: Shear rate-Shear stress relation for *Glycerine*

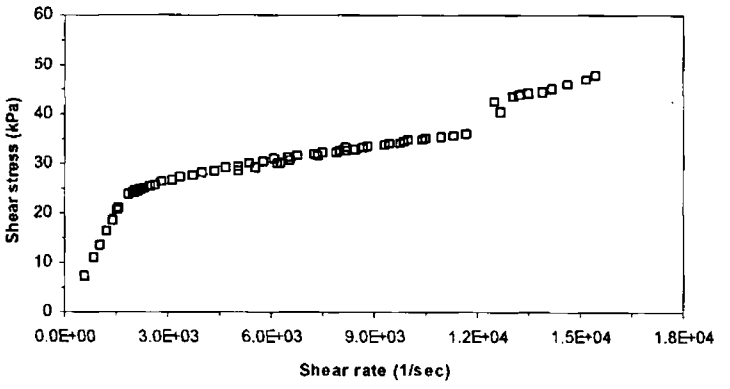

Figure 4. 24: Shear rate-Shear stress relation for *Silicone-5*

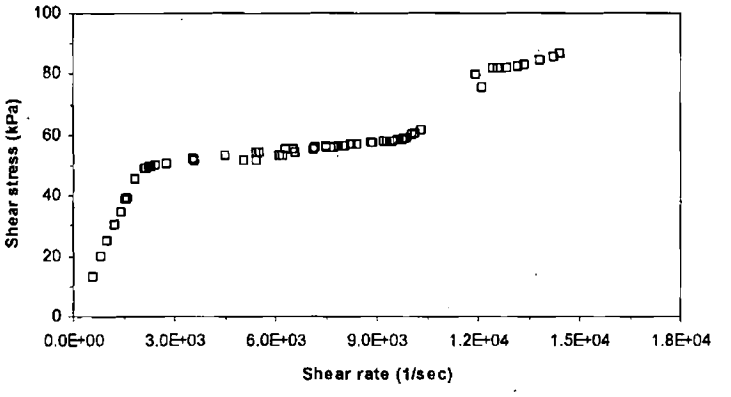

Figure 4. 25: Shear rate-Shear stress relation for *Silicone-12.5*

Moreover, the Herschel-Bulkley model requires the yielding viscosity which is considered as the maximum viscosity value in non-Newtonian model. These constants for each viscous fluid and its yielding-shear rate magnitude as obtained by non-Newtonian power-law model are listed in Table 4.2.

Table 4. 2: Constants of the viscous fluids for Herschel-Bulkley model

Viscous fluid	Yielding-Shear rate (sec^{-1})	Yield stress (kPa)	Yielding viscosity ($kg.m^{-1}.sec^{-1}$)
Glycerine	80	0.6	6
Silicone-5	1800	23.5	13
Silicone-12.5	2100	48	24

By applying these constants in the Herschel-Bulkley model, the viscosity profiles were observed for each viscous fluid at high shear rates within all gaps. For each fluid, the viscosities profiles showed similar performance into the gaps. Figures 4.26, 4.27 and 4.28 show the viscosity profiles obtained for each viscous fluid at high shear rate ranges.

It is clear that the viscosity profiles show slighter magnitudes than those applied within the non-Newtonian power-law model, where at higher shear rates, it shows somehow law values while the performance of viscous fluids begin to behave as Newtonian fluids, which for glycerine around (0.65 $kg.m^{-1}.sec^{-1}$) at shear rate range of $4x10^4$ sec^{-1}, ≈ (0.5 $kg.m^{-1}.sec^{-1}$) at $1.2x10^5$ sec^{-1} for silicone-5 and , ≈ (0.6 $kg.m^{-1}.sec^{-1}$) at $1.2x10^5$ sec^{-1} for silicone-12.5.

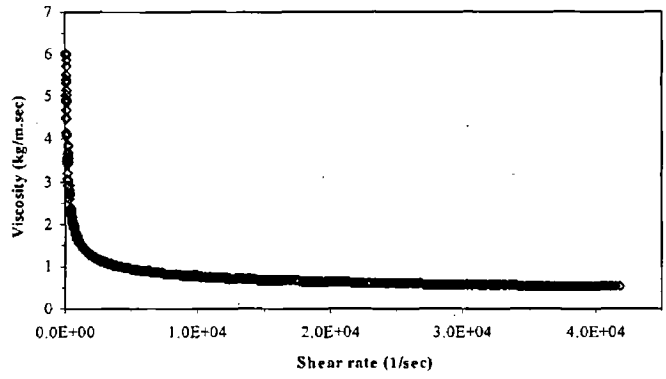

Figure 4. 26: Viscosity versus shear rate based on Herschel-Bulkley model for *Glycerine* within *(0.9/0.3) gap ratio*

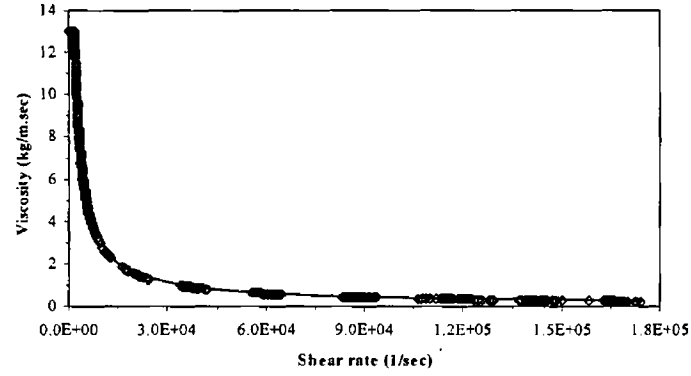

Figure 4. 27: Viscosity versus shear rate based on Herschel-Bulkley model for *Silicone-5* within *(0.9/0.3) gap ratio*

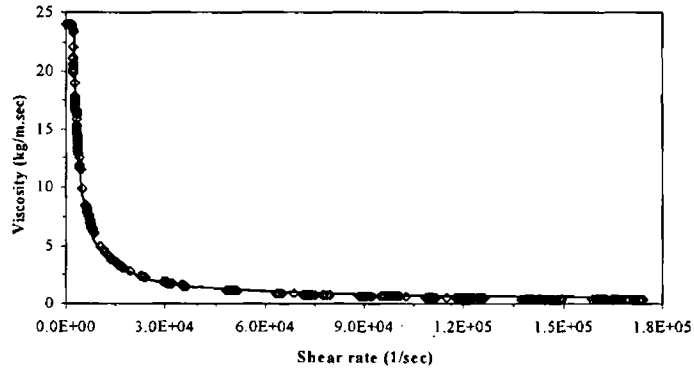

Figure 4. 28: Viscosity versus shear rate based on Herschel-Bulkley model for *Silicone-12.5* within *(0.9/0.3) gap ratio*

4.2.3 Pressure distributions results of the computational models

The pressure profiles obtained by non-Newtonian power-law model showed high pressure gradients, which vary significantly from the experimental results. These pressure values could be caused by the non-Newtonian power-law treatment of the fluid viscosity. The viscosity of the fluid in non-Newtonian power law model has higher and lower limits and can not exceed these limiting values [102]. A sample of comparison pressure distribution profiles for Glycerine by the non-Newtonian power-law model and experimental measurements within the (0.9/0.3) gap ratio is shown in Figure 4.29. The variation between the experiment and analysis is most likely due to the use of power-law model for viscosity of Glycerine.

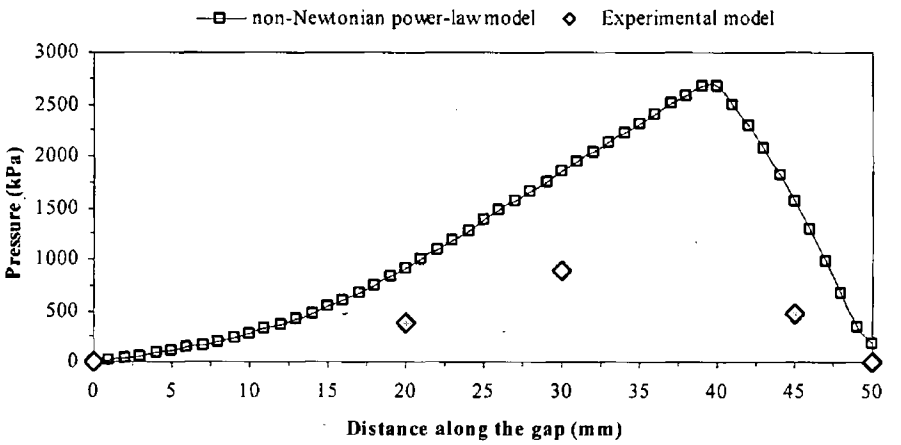

Figure 4. 29: Comparison of pressure distribution profiles for *Glycerine* by non-Newtonian power-law model and experimental measurements within *(0.9/0.3) gap ratio at 1.5 m.sec^{-1} shaft speed*

Therefore, by applying the yield stress of the viscous fluids; the Herschel-Bulkley model achieved better consequences and improved conformity with the experimental results, since the model can exhibit the shear-thinning or shear-thickening behaviour based on the value of the power-law index [102].

Figure 4.30 shows the pressure distribution profiles for Glycerine at 0.5 m.sec^{-1} shaft speed through various gap ratios. It is obvious that the dimensional shapes of the gap give dissimilar behaviour of pressure profile at specific shearing speed. It shows somehow nonlinear development of pressure distribution within the tapered

zone to reach the highest amount at the step for some cases, then drops linearly after the step through the parallel zone and leaves the gap at insignificant pressure amount. Not all gaps present the same mode; (1.2/0.3) and (1.5/0.3) gap ratio show different trends. The behaviour within the tapered zone is fully nonlinear. Pressure drops appear in the second half of tapered bore which might caused by the slip condition on the gap wall.

In most gaps Glycerine behaves in the same manner except within gap ratio of (1.2/0.3) which shows different trend where it exhibits to have a pressure drop in the second part of the tapered bore to reach the step with lesser pressure magnitude at all speeds as shown in Figure 4.31.

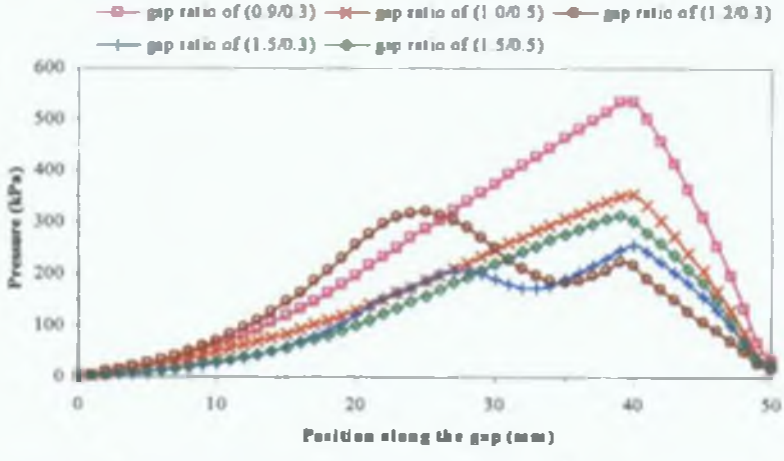

Figure 4. 30: Pressure distribution profile for *Glycerine* at *0.5 m sec*$^{-1}$ shaft speed at various gap ratios

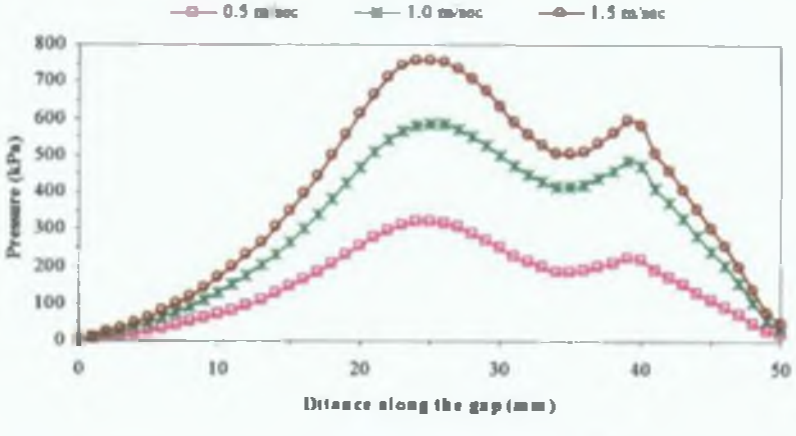

Figure 4. 31: Pressure distribution profiles for *Glycerine* within *(1.2/0.3)* at various shaft speeds

On the other hand, in (1.5/0.3) gap ratio, the pressure for Glycerine behaves similar to the (1.2/0.3) gap ratio, but the drop is not so high as observed in that case, where the step-pressure higher than the developed pressure within the tapered zone as Figure 4.32 shows.

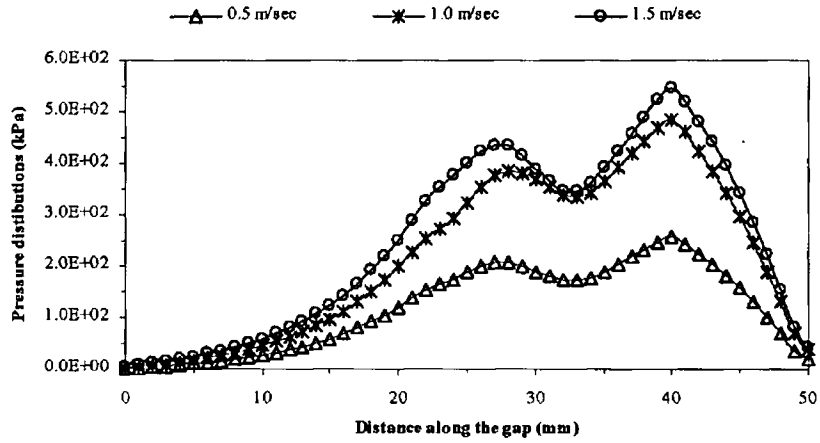

Figure 4. 32: Pressure distribution profiles for *Glycerine* within *(1.5/0.3)* at various shaft speeds

The pressure distributions for all viscous fluids exhibited similar trends and somehow higher magnitudes are observed whenever the fluid viscosity is higher. These pressure profiles are presented in Appendix-A, where the increase in the shaft speed presented somehow higher hydrodynamic pressure.

4.3 Comparisons of the Models Results and Its Discussions

4.3.1 Computational models

Computationally, Figure 4.33 and 4.34 show the pressure distribution profiles for the three viscous fluids at 0.5 $m.sec^{-1}$ and 1.0 $m.sec^{-1}$ rotating wall speed within (0.9/0.3) gap ratio. It shows nonlinear developed pressure distribution within the tapered zone to reach the highest amount at the step, then drops linearly after the step in the parallel zone and leaves the gap at insignificant pressure amount. At 0.5 $m.sec^{-1}$ rotating speed, Silicone-12.5 has $1.8x10^3$ kPa at the step which is the highest pressure magnitude within the gap. On the other hand, Glycerine shows the less pressure distribution which is $5x10^2$ kPa at the same region. It is obvious at the

same shearing speed that the fluid of higher viscosity is the higher developed pressure magnitude.

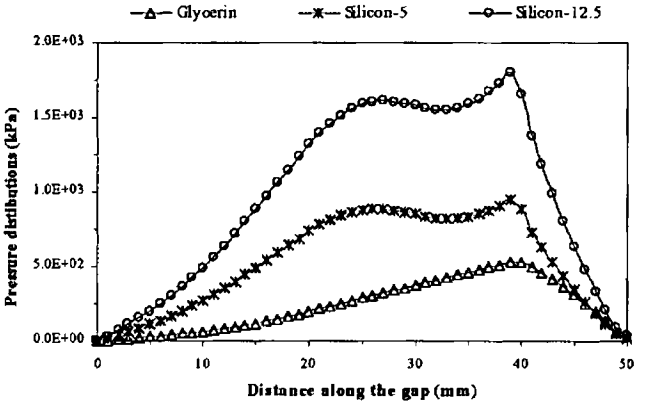

Figure 4. 33: Pressure distribution profile at *0.5 m.sec^{-1}* rotating wall speed within *(0.9/0.3) gap ratio*

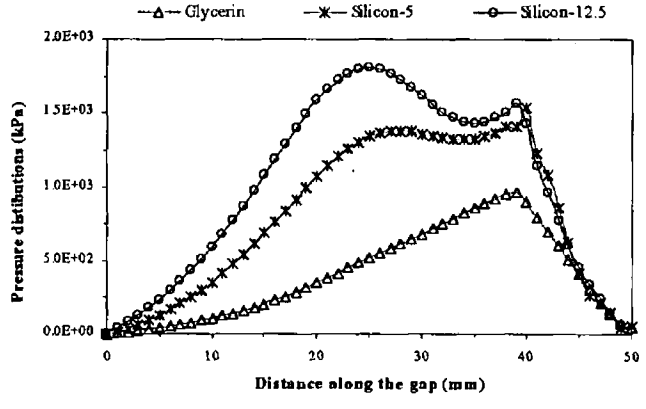

Figure 4. 34: Pressure distribution profile at *1.0 m.sec^{-1}* rotating wall speed within *(0.9/0.3) gap ratio*

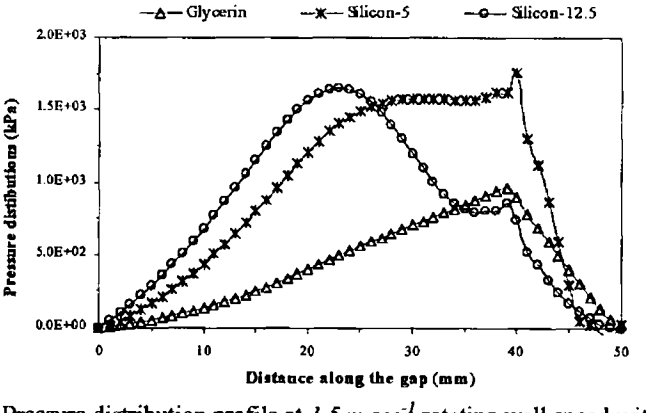

Figure 4. 35: Pressure distribution profile at *1.5 m.sec^{-1}* rotating wall speed within *(0.9/0.3) gap ratio*

For all viscous fluids within (0.9/0.3) gap ratio, the pressure profiles exhibited quite similar trends at 0.5 $m.sec^{-1}$ and 1.0 $m.sec^{-1}$ shaft speeds. However, at 1.5 $m.sec^{-1}$ shaft speed, the pressure profiles for Silicone-5 and silicone-12.5 showed dissimilar trends, where a pressure drops found in both cases, as it showed above in Figure 4.35.

Silicone-12.5 profile shows higher pressure drop which could be affected by the critical shear stress on the wall of the insert-I. The drop starts after the developed pressure reaches the highest magnitude ($1.65x10^3$ kPa) at the middle of the tapered zone, then continues to show nearly the less amount of the pressure *(comparing to the other two fluids)* at the step which is ($8.5x10^2$ kPa) and the slighter pressure magnitude in the first half of the parallel zone. Similar situation is observed for Silicone-5 but the developed pressure remains steady after the second half of the tapered zone ($1.55x10^2$ kPa) to reach the highest magnitude at the step ($1.75x10^2$ kPa), then it goes down linearly slight until the middle of the parallel zone and leaves at zero pressure. For both cases the pressure profiles showed nonlinear behaviour in the parallel zone which vary with the theory.

The pressure profiles in most cases have showed similar trends as described above, same as Figures 4.36, 4.37 and 4.38 shown the pressure profiles within (1.2/0.3) gap ratio. The rest of pressure profiles for all gaps are presented in Appendix-A

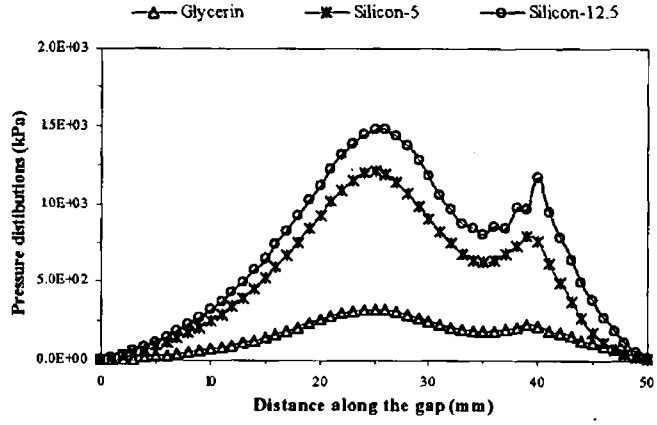

Figure 4. 36: Pressure distribution profile at *0.5 $m.sec^{-1}$* rotating wall speed within *(1.2/0.3) gap ratio*

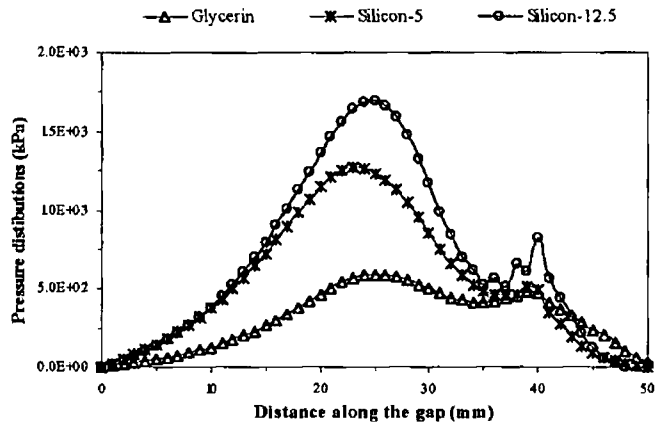

Figure 4. 37: Pressure distribution profile at *1.0 m.sec*$^{-1}$ rotating wall speed within *(1.2/0.3) gap ratio*

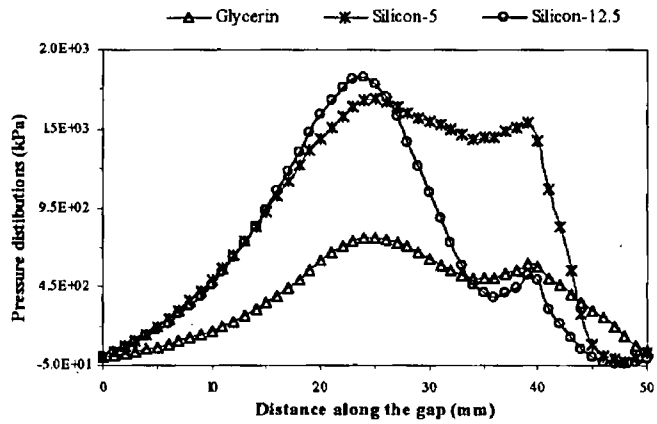

Figure 4. 38: Pressure distribution profile at *1.5 m.sec*$^{-1}$ rotating wall speed within *(1.2/0.3) gap ratio*

It can be noticed that the higher the fluid viscosity is the higher pressure drops which could be because of their variety viscosities ranges as well as the effect of the critical shear stress on the gap wall where the higher the fluid viscosity is the higher critical shear magnitude obtained.

4.3.2 Computational Fluid Dynamics and Relative velocity profiles

The relative velocity magnitude of the fluid is one more significant factor could affect the development of pressure distribution within the gap. It could be of benefit to observe the profiles of fluid velocities within a radial direction at various locations along the gap and compute the velocity vector of the fluid layers.

Several fluid surfaces are created before and within the gaps to observe the velocity behaviour at specific locations based on the assumption of the tapered-stepped-parallel bore as shown in the schematic diagram of Figure 4.39, where surface-1 is created at 15 mm distance before the entrance of the gap.

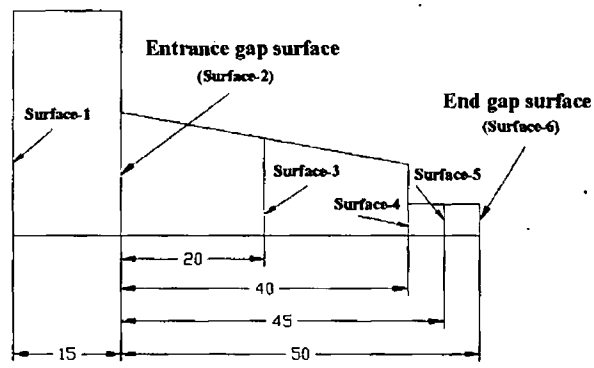

Figure 4. 39: Schematic diagram of fluid surfaces within the tapered-stepped-parallel gap

The velocity vector was obtained for the fluid domain as shown above in Figure 4.19. Velocity vector for each surface gives the magnitude of the surface fluid-layers velocities and their directions within the domain. Figures 4.40, 4.41, 4.42, 4.43, 4.44 and 4.45 show the velocity vectors of fluid layers at the surfaces as obtained in (0.9/0.3) gap ratio for Silicone-12.5 at 1.5 $m.sec^{-1}$ rotating wall speed.

At surface-1, the velocity vector shows a back-flow condition, where the fluid elements are encountered by the left-side-wall of insert-I. A similar behaviour was indicated for surface-2 *(gap entrance surface),* which could be caused by the step-wall. On the other hand, the three fluid surfaces in the parallel bore do not show the flow-back condition because there is no wall to interrupt the flow and reverses its direction which possibly will change its performance.

Profiles of x-relative velocity versus radial distance relations might describe the velocity behaviour at each surface as shown in Figures 4.46, 4.47, 4.48, 4.49, 4.50 and 4.51. In Figure 4.46, the x-relative velocity profile of the fluid-surface-1 shows negative quantities for most of the fluid domain below the pressure chamber wall until the radial distance of 3 mm, where velocities start to have positive values. Similar behaviour was noticed for surface-2, but the extents of the negative

velocities are less, because the size of step-wall is smaller since the gap dimension is too small compared with the whole unit.

Figure 4. 40: Velocity vector ($m.sec^{-1}$) at *surface-1*

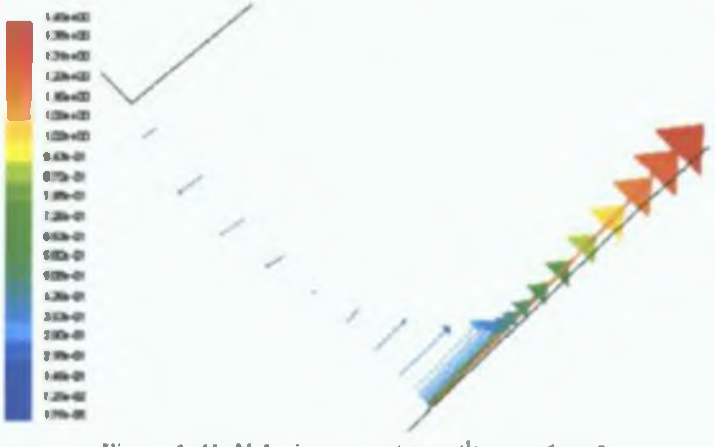

Figure 4. 41: Velocity vector ($m.sec^{-1}$) at *surface-2*

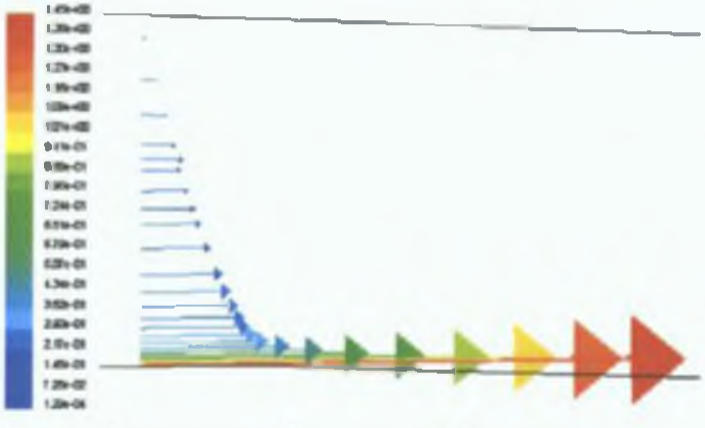

Figure 4. 42: Velocity vector ($m.sec^{-1}$) at *surface-3*

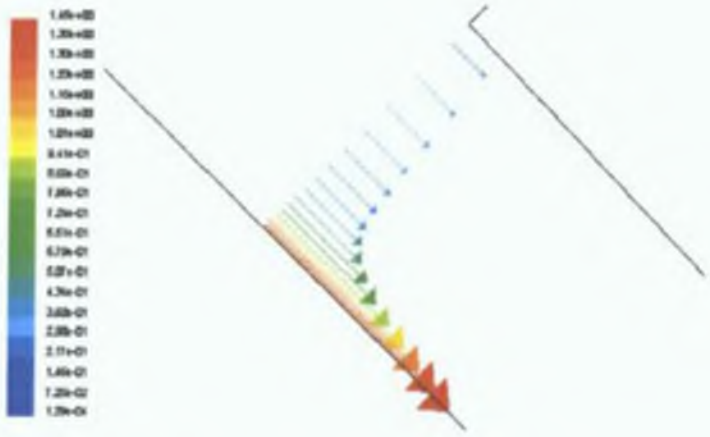

Figure 4. 43: Velocity vector (m.sec^{-1}) at *surface-4*

Figure 4. 44: Velocity vector (m.sec^{-1}) at *surface-5*

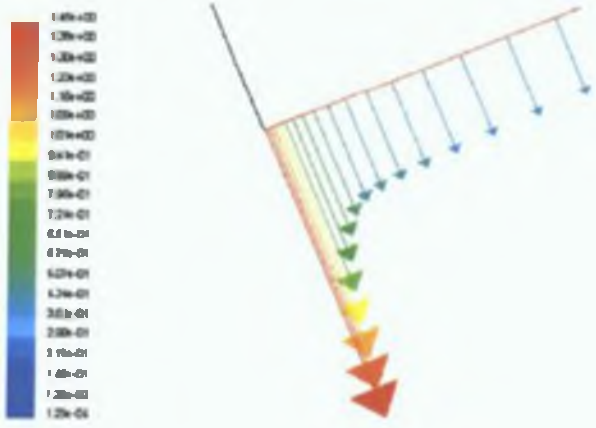

Figure 4. 45: Velocity vector (m.sec^{-1}) at *surface-6*

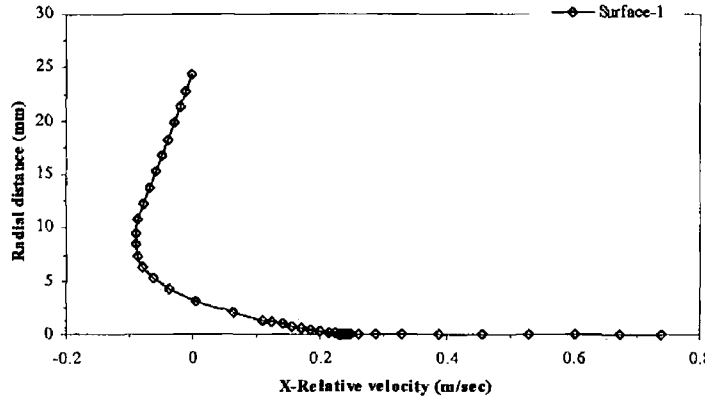

Figure 4. 46: *X*-Relative velocity of the fluid layers at *surface-1*

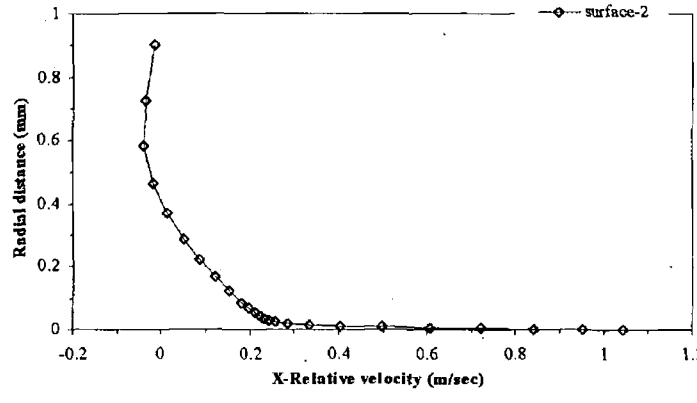

Figure 4: 47: *X*-Relative velocity of the fluid layers at *surface-2*

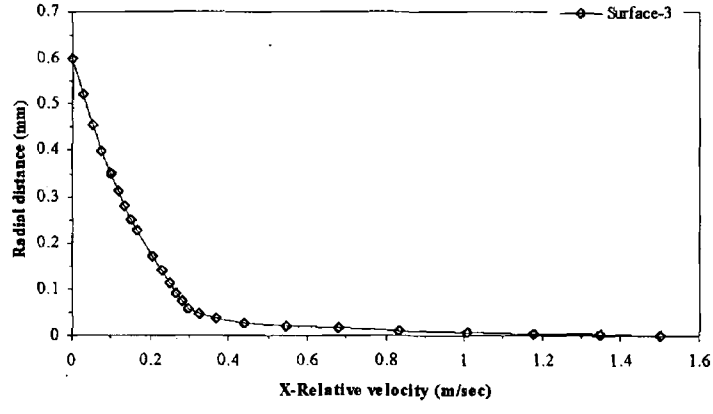

Figure 4. 48: *X*-Relative velocity of the fluid layers at *surface-3*

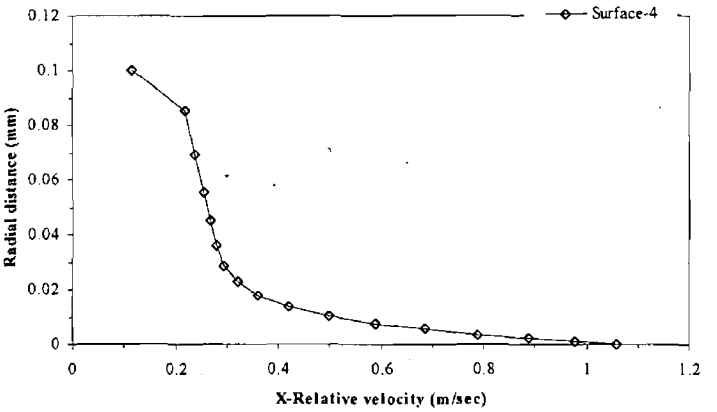

Figure 4. 49: *X*-Relative velocity of the fluid layers at *surface-4*

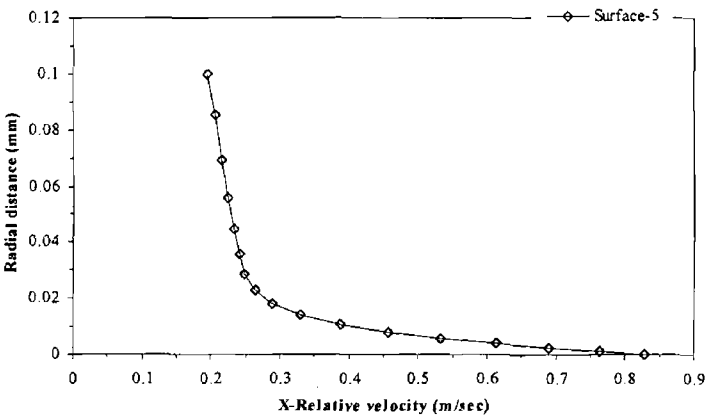

Figure 4. 50: *X*-Relative velocity of the fluid layers at *surface-5*

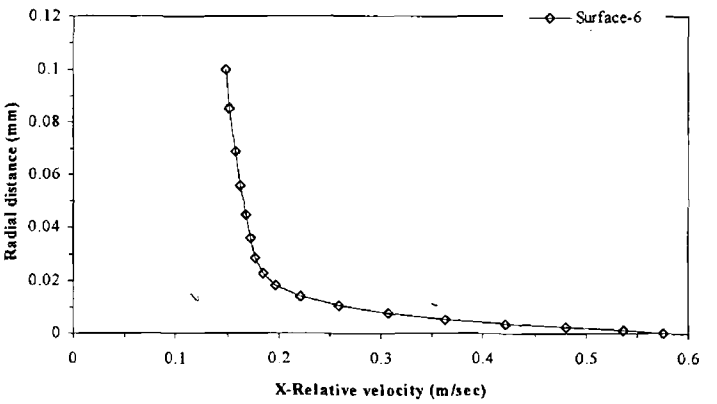

Figure 4. 51: *X*-Relative velocity of the fluid layers at *surface-6*

The three fluid surfaces within the parallel bore showed positive x-relative velocities magnitudes with no back-flow observed in this zone. The back flow conditions obtained before the gap region and at the gap entrance could be the reason for the negligible developed pressure gradient in the fluid domain, where not all fluid elements can get through the gap entrance because of the insert-1 left-side wall and the coming back-flow from inside the gap, all together expanded back flow outside the gap which makes the fluid moves as a swirl in this region.

4.4 Comparison of the results of experimental and computational models

Computationally, the pressure distribution profiles were obtained along the whole gap since they were not possible to observe experimentally at particular locations. Generally, most cases of pressure distribution results showed good agreements between the experimental and computational models.

Figure 4.90 shows a comparison pressure profile for both models within (0.9/0.3) gap ratio for Glycerine at 1.0 $m.sec^{-1}$ shaft speed. It shows that the highest pressure magnitude is obtained near the step region with 10^3 kPa which agreed with the theory of the developed hydrodynamic pressure. Not all viscous fluids showed the same distribution behaviours within this gap; silicone-5 profile shows nearly steady pressure distributions within the second part of the tapered zone which almost agreed with the experimental result where the step-pressure reaches $1.5x\ 10^3$ kPa as shown in Figure 4.53.

For Silicone-12.5, the pressure distribution at same speed shows a drop in the second half of the tapered bore to reach the step with less magnitude of pressure ($0.8x10^2$ kPa) than the tapered bore as shown in Figure 4.54. This drop in the pressure profile could be caused by the slip condition on the tapered bore wall while Silicone-12.5 has much higher viscosity than Glycerine, as well as the back flow condition near the step wall could affect its development. These pressure profiles illustrated that, in the parallel bore they have less pressure magnitudes for the higher fluid viscosity which can be caused by the effect of shear stress on the wall.

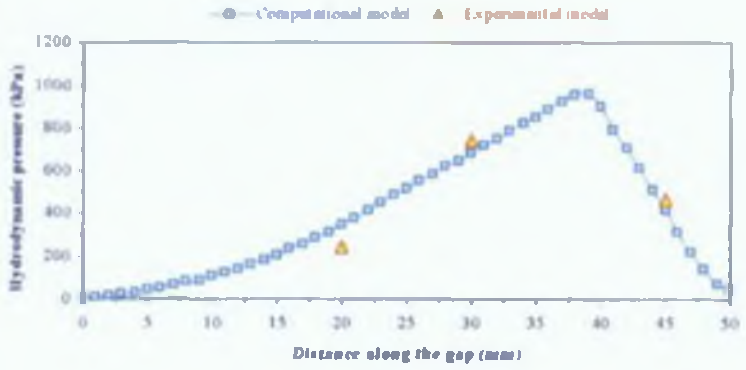

Figure 4. 52: Pressure distribution profile for *Glycerine* within tapered gap ratio of *(0.9/0.3) at 1.0 m.sec^{-1}* shaft speed

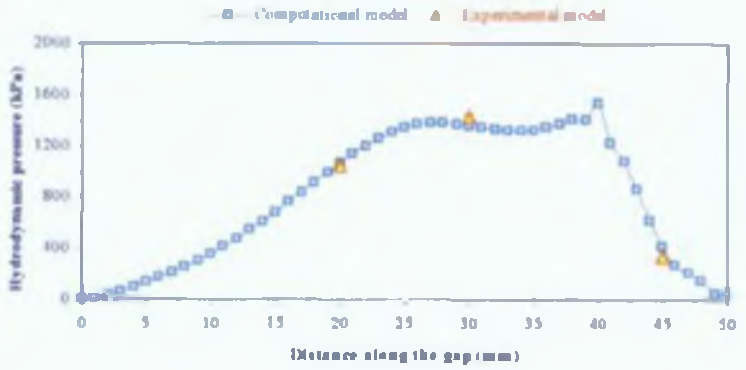

Figure 4. 53: Pressure distribution profile for *Silicone-5* within tapered gap ratio of *(0.9/0.3) at 1.0 m.sec^{-1} shaft speed*

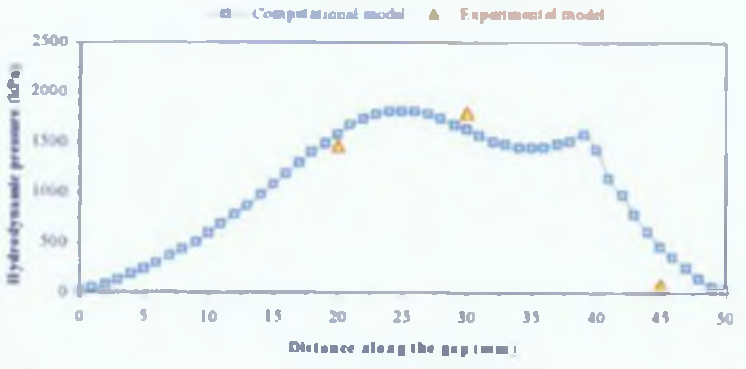

Figure 4. 54: Pressure distribution profile for *Silicone-12.5* within tapered gap ratio of *(0.9/0.3) at 1.0 m.sec^{-1} shaft speed*

In (1.5/0.3) gap ratio, Silicone-12.5 showed slightly similar pressure magnitudes within the tapered bore. However, in the experimental results the pressure distribution in the parallel zone found to be reasonably negligible at all speeds which is less than $0.06x10^{3}$ kPa. In the computational models, the pressure exhibited to have a negative magnitude of about -10^{2} kPa at 1.5 m.sec^{-1} rotating speed as shown in Figure 4.55.

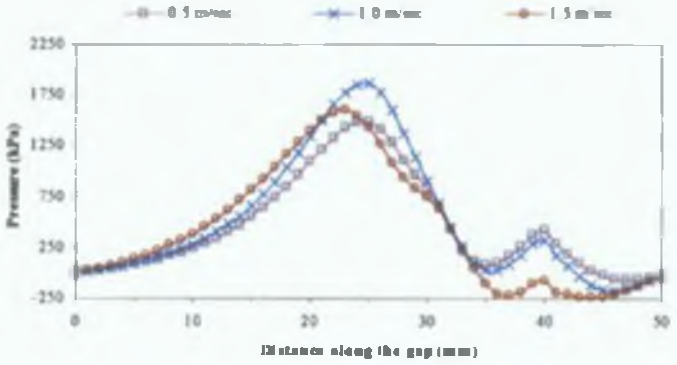

Figure 4. 55: Pressure distribution profile for *Silicone-12.5* within tapered gap ratio of *(1.5/0.3)* at various rotating shaft speed

This case showed the highest pressure magnitude observed at the first part of the tapered zone then large pressure drops occurred in the second part of the bore, where it reaches a negative pressure value before the step region to increase slightly higher before the step then drops again in the parallel bore below zero pressure to leave the die at zero pressure; as shown in Figure 4.56, the x-relative velocity profile doesn't show the back flow condition in parallel bore. A more a advanced model may highlight this in more details.

On the other hand, it could be possible, because of the shearing between the fluid layers, where flow of these layers are affected by the moving wall and the narrower gap at the same time, once the fluid elements reach the parallel zone, the shearing speeds of these fluid layers increase, which might affect the viscosity of the fluid to decrease, thus the pressure drops. Again, the main reason here could be the effect of the slip condition on the wall while the pressure distributions show that the

higher the fluid viscosity is the greater the pressure drop obtained. This pressure drop could be explained as; the critical shear stress prevents the pressure to develop over a specific magnitude which at this point forces the pressure to decrease.

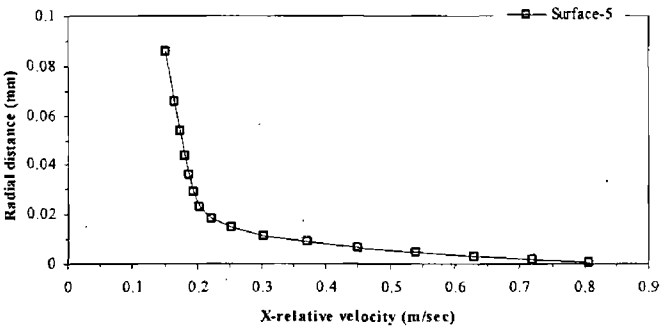

Figure 4. 56: *X*-relative velocity profile at surface-5 for *Silicone-12.5* within gap ratio of *(1.5/0.3) at 1.5* $m.sec^{-1}$ rotating shaft speed

Experimentally, the pressure was assumed to be zero at the end of the die, which found slightly varied with the computational models. While in the CFD, the fluid at the pressure-outlet boundary condition computes the pressure from the flow of the fluid domain [98]. All the comparison of pressure distribution profiles are presented in Appendix-A.

Chapter Five

Conclusions and suggestions for future work

5.1Conclusion

This project investigates the development of hydrodynamic pressure behaviour through various converging gaps in conjunction with wire drawing/coating process involving polymer melts. This study is represented in two sections as follows;

5.1.1 Experimental study

- The fluid viscosities were obtained using a Cone-plate type Brookfield viscometer at low shear rate ranges from zero to 22 sec^{-1}. The viscosity for all fluids showed a Newtonian behaviour at these ranges of shear rates.
- The developed pressure profiles within the tapered-stepped-parallel gap for Glycerine and two different types of silicone fluids showed that, the higher pressure magnitude was obtained within the narrowest converging gap *(e.g. for Glycerine within (0.9/0.3) gap, the developed pressure reached 900 kPa at 1.5 $m.sec^{-1}$ at the second transducer while in the wider gap (1.5/0.5) reached 650 kPa at same speed)*
- The effect of the fluid viscosity on the process showed that for higher fluid viscosity higher pressure values were obtained
- The influence of the higher speed on the pressure distributions have been investigated for all gaps at various rotating shaft speeds. The developed pressure at higher speed was larger than it for lower speed. The obtained pressure at 1.5 $m.sec^{-1}$ showed higher magnitudes than it at 0.5 and 1.0 $m.sec^{-1}$ shaft speed for all viscous fluids during all gaps. On the other hand, for higher fluid viscosity *(silicone-5 and silicone-12.5)* the developed pressure showed drops in the second part of the die *(the parallel bore)* where the higher applied speed the larger pressure drop was obtained.

5.1.2 Computational simulations

- Through the approach of computational fluid dynamics, using the limitations of the fluid viscosities at maximum and minimum values; the viscosities of the fluids within the process were obtained by means of non-Newtonian power-law model and the critical shear stress values of the viscous fluids are determined. The yielding stress for lower fluid viscosity *(Glycerine)* was obtained at very low shear rate (80 sec^{-1}), which found to be 0.6 kPa while for Silicon-12.5 was 48 kPa at 2100 sec^{-1}.
- The pressure distribution profiles during the process were obtained within all gaps by using the Herschel-Bulkley model for non-Newtonian fluids, where the achieved results showed good agreement with the experimental models.
- The pressure gradients at the step region were obtained for all shaft speeds and gaps *(because it is difficult to obtain experimentally).*
- The change in the die shape and its dimension effect the pressure distribution within the process and showed that the wider converging gap the lower developed pressure was obtained.
- The critical shear stress has an essential affect on the developed pressure and found that the higher fluid viscosity the higher affect of the critical shear stress obtained.
- The velocity vectors and the magnitudes of the x-relative velocity were considered for various radial fluid surfaces, which showed somewhat affect on the pressure distributions.

5.2 Suggestions for future work

- The rheological performances of the viscous fluids could be better solved if the change in pressure involved is accounted for with the change in temperature.

- Experimentally, the temperature of the process was obtained outside the gap because it was not possible to insert a thermocouple within the gap without any damage. The temperature was considered to be constant. It is therefore suggested to insert two thermocouples before and after the gap to observe the change in the temperature within the gap then run the computational model based on these values where, the better rheological understanding of the non-Newtonian behaviour can be enhanced once the temperature is considered.
- The geometrical shape of the die could be changed to tapered-stepped-tapered or parabolic forms.
- Computationally, the viscous fluids could be changed by various polymer melt types with very high viscosities involved by heating-up system for the pressure chamber.
- The process behaviour was considered to be steady and the flow laminar because there were no blades on the shaft surface. However, the flow showed a swirl flow outside the gap which might be resulted due to turbulent flow. Therefore, it would be a benefit to insert pressure transducer within unit before the gap and study the process based on the turbulent and unsteady conditions within the CFD.

References

[1] http://www.gbsco.com/page2.html, "*The Fight against the Friction Begins*", SKF Distributor, General Bearing Services Co. S.A.R.L (2004)

[2] P. M. B. Walker. "*Dictionary of Science and Technology*". Chambers, (1999)

[3] http://www.rheology.org/sor/info/default.htm, "*About the Society of Rheology*", The Society of Rheology, (2003)

[4] D. Doraiswamy. "*The Origins of Rheology, a Short Historical Excursion*". Dupont Technologies, Experimental Station, Wilmington, 0334, (1988)

[5] http://www.contract-research-technical-consultant.com, "*Rheometry*", Impact Analytical, (2004)

[6] P. C. Powell. "*Engineering with polymers*". Chapman & Hall. New York, (1983)

[7] L. Horath. "*TED 225, Material Processing II*". Course Packet, Applied Engineering & Technology, California University of Pennsylvania, (2002)

[8] S. L. Rosen. "*Fundamental Principles of Polymeric Materials*". John Wiley& Sons, Inc, (1993)

[9] H. E. King, J. E. Herbolzheimer and R. L. Cook, "*The Diamond-Anvil Cell as a High Pressure Viscometer*". Journal of applied Physics, 2071-2081, (1992)

[10] M. M. Denn, "*Process Fluid Mechanics*". Prentice-Hall, Inc. Englewood Cliffs, New Jersey, (1998)

[11] S. Kim "*A Study of Non-Newtonian Viscosity and Yield Stress of Blood in a Scanning Capillary-Tube Rheometer*". PhD Thesis, Drexel University, Philadelphia, USA, (2002)

[12] S. Akter, "*Study of Viscous Flow During Thin Film Polymer Coating and Drawing of Continuum*". PhD Theses, Dublin City University, Ireland, (1997)

[13] J. F. Steffe, "*Rheological Methods In Food Process Engineering*", PhD, P.E, Michigan State University, (1996)

[14] H.A. Barnes, J.F. Hutton, and K. Walters, "*An Introduction to Rheology*" Elsevier Amsterdam, (1989)

[15] B. R. Munson, D. F. Young and T. H. Okiishi, "*Fundamentals of Fluid Mechanics*" Wiley, New York, (1998)

[16] B. Rabinowitsch, "*Uber Die Vikostat And Elastizitat Von Solen*" Z. Phys. Chem. 141, (1929)

[17] H. Parvinmehr, "*Optimization of Plasto-hydrodynamic System of Wire Drawing Using Polymer Melts*". PhD Theses. Dublin City University, (1983)

[18] J. A. Brydson, "*Flow Properties of Polymer Melts*", Published By Plastic Institute, London, (1970)

[19] L. Masaro and X. Zhu "*Physical Models of Diffusion for Polymer Solutions, Gels and Solids*" Prog. Polym. Sci. 24, 731-775, (1999)

[20] M. L. Williams, R. F. Landel And J.D. Ferry, "*The Temperature Dependence of Relaxation Mechanisms In Amorphous Polymers and Other Glass-Forming Liquids*", J. Am. Chem. Soc., 77, 3701-3706, (1955)

[21] G.J. Dienes, Applied Physics series, 24, 779, (1957)

[22] http://www2.ocean.washington.edu/oc540/lec02-25/, "*Settling of Particles; Threshold of Motion, Oceanography 540, Marine Geological Processes*", (2002)

[23] J. J. Benbow and P. Lamb, "*New Aspect of Melt Fracture*", Spe Trans, 7, (1963)

[24] R. F. Westover, "*The Significance of Slip In Polymer Melt Flow*" Polymer Engineering and Science, 83, (1966)

[25] D.M. Binding, M.A. Couch and K. Walters "*The Pressure Dependence of The Shear and Elongational Properties of Polymer Melts*" J. Non-Newtonian Fluid Mech. 79, 137-155, (1998)

[26] B. Maxwell and A. Jung, "*Hydrostatic Pressure Effect on Polymer Melt Viscosity*" Modern Plastics, 35, 174, (1957)

[27] R.F. Westover, "*Effect of Hydrostatic Pressure on Polyethylene Melt Rheology*" Society of Plastic Engineering Translations. 1, 14, (1961)

[28] S.Y. Choi, "*Determination of Melt Viscosity as a Function of Hydrostatic Pressure in A Melt Viscometer*", Journal of Polymer Science. 6, 2043, (1968)

[29] S.Y. Choi, N. Nakajima, In: Proc. 5th Int. Cong. of Rheology, University of Tokyo Press, 4, 287, (1970)

[30] V. Semjonov, "*Ube Rein Rotationsviskosimeter Zur Messung Der Druckabhangigkeit Der Viskoctat*" Einiger Polyolefinschmelzen, Rheologica Acta, 2, 133

[31] F.N. Cogswell and J.C. Mcgowan, Brit. Polym. J. 4, 183 (1972)

[32] F. N. Cogswell," *The Influence of Pressure on the Viscosity of Polymer Melts*", Plastics & Polymers, 41, 39.

[33] J. Ellis, "*Ultrasonic and Viscoelastic Studies at Different Pressures*", PhD. Thesis, University Of Salford, (1976)

[34] D.M. Binding, M.A. Couch, K. Walters, "*The Pressure Dependence of the Shear and Elongational Properties of Polymer Melts*". J. Non-Newtonian Fluid Mech. 79,137-155, (1998)

[35] D.C Christopherson And P.B. Naylor, "*Promotion of Fluid Lubrication in Wire Drawing*", Proc. Inst. Mech. Eng., 643 , (1955)

[36] J.G. Wistreich, "*Lubrication in Wire Drawing*", Wear, 505-511, (1957)

[37] G. H. Tattersall, " *Hydrodynamic Lubrication In Wire Drawing*" J. Mech. Eng Sc Vol.3, No 4, 378, (1961)

[38] P. S. Chu, "*Theory of Lubrication Applied to Pressure Nozzle Design in Wire Drawing*" Proc. Inst. Mech. Eng. 181, (1967)

[39] D. S. Bedi, "*A Hydrodynamic Model for Wire Drawing*". Journal of The International Production And Research, Vol.6, N.4, (1968)

[40] A. Middilemiss, "*Hydrodynamic Lubrication For Drawing Steel Wire*" Tribology in Iron and Steel Works, Isi, Publication 125

[41] V. L. Kalmogrov And K. P. Selishchev, "*Cold Drawing Tubes With Improved Lubrication*" Stall In English, 830-831, (1962)

[42] M. Bloor, D. Dowson and B. Parson, "*An Elasto-Palsto-Hydrodynamic Lubrication Analysis of The Plane Strain Drawing Process*" Journal of Mechanical Seince, Vol-12, No-3, (1970)

[43] S.I. Orlov, V.L. Kolmogrov, V.I. Uralskll and V.T. Stukalov "*Integrated development and introduction of new high speed mills and hydrodynamic lubrication system for drawing wires*", Steel in the USSR. Vol-10, 953-956, (1974)

[44] S. T.N. Swamy, B. S. Prabhu and B. V. A. Rao, "*Calculated Load Capacity of Non-Newtonian Lubrication Infinite Width Bearings*" , Ear, Vol.3, 277-285, (1975)

[45] P.J. Thompson And G.R. Symmons, "*A Plasto-Hydrodynamic Analysis of The Lubrication and Coating of Wire Using Polymer Melt During Drawing*", Proc. Inst. Mech. Eng., 191, (13), 115, (1977)

[46] Symmons, G. R.; And Thompson, P. J. "*Hydrodynamic Lubrication And Coating Of Wire Using a Polymer Melt During The Drawing Operation*", Wire Industry, Vol-45, 469-473, 483, (1978)

[47] A.J. Stevens, "*A Plasto-Hydrodynamic Investigation of the Lubrication and Coating of Wire Using a Polymer Melt During Drawing Process*". M. Phil. Thesis, Sheffield City Polytechnic, (1979)

[48] R. Crampton, G.R Symmons And M.S.J. Hashmi, " *A Non-Newtonian Plasto-Hydrodynamic Analysis of the Lubrication and Coating of Wire Using a Polymer Melt During Drawing*", Proc. Int. Symposium On Metal Working Lubrication, Sanfrancisco, USA, (1980)

[49] M. S. J. Hashmi, R. Crampton and G. R. Symmons, "*Effects of Strain Hardening And Strain Rate Sensitivity of The Wire Material During Drawing Under Non-Newtonian Plasto-hydrodynamic Lubrication Conditions*", International Journal Of Machine Tool Design & Research, Vol21, P 71-86, (1981)

[50] H. Parvinmehr, G. R. Symmons and M. S. J. Hashmi, "*Novel Technique of Wire Drawing*" Journal Of Mechanical Engineering Science, Vol24, N 1, P 1-4, (1982)

[51] H. Parvinmehr, G. R. Symmons and M. S. J. Hashmi, "*Non-Newtonian Plasto-Hydrodynamic Analysis of Dieless Wire-Drawing Process Using a Stepped Bore Unit*", International Journal Of Mechanical Sciences, V 29, N 4, P 239-257, (1982)

[52] H. Parvinmehr, G. R. Symmons and M. S. J. Hashmi, "*Plasto-Hydrodynamic, Dieless Wire Drawing: Theoretical Treatment And Experimental Results*", Developments In The Drawing of Metals, Proceedings of The International Conference, London, Metals Soc (Book 301), P 54-62, (1983)

[53] H. Parvinmehr, "*Optimisation of Plasto-Hydrodynamic System of Wire Drawing Using Polymer Melts*", PhD Thesis, Sheffield City Polytechnic, UK, (1983)

[54] G. R Symmons, M. S. J. Hashmi and H. Parvinmehr "*Aspects Of Product Quality And Process Control in Plasto-Hydrodynamic Dieless Wire*

Drawing", Proceeding of 1st Conference on Manufacturing Technology, Irish Manufacturing Committee, Dublin, Pp.153-172, (1984)

[55] M. S. J. Hashmi and G. R. Symmons, "*A Numerical Solution For The Plasto-Hydrodynamic Drawing of Rigid Non-Linearly Strain Hardening Continuum Through a Conical Orifice*". 2nd International Conference on Numerical Methods For Non-Linear Problems, Spain, (1984)

[56] M. I. Panwher, R. Crampton and M. S. J. Hashmi " *Dieless Tube Sinking Plasto-Hydrodynamic Analysis Based on Newtonian Fluid Characteristics*" Proceeding of 1st Conference on Manufacturing Technology, Irish Manufacturing Committee, Pp.153-172, Dublin, (1984)

[57] M. I. Panwher, R. Crampton and M. S. J. Hashmi, "*Plasto-Hydrodynamic Tube Sinking: Experimental Evidence And Numerical Solution*" Proceeding of 3rd International Conference on Numerical Methods For Non-Linear Problems, Dubrovnik, Yugoslavia, Pp.115-129, (1986)

[58] M. I. Panwher "*A Novel Technique For Tube Sinking*" PhD Thesis Sheffield City Polytechnic, UK, (1986)

[59] M. I. Panwher, R. Crampton and M. S. J. Hashmi, "*Mathematical Modeling of Dieless Tube Sinking Based On Non-Linear Deformation Profile*", Proceeding of 6th Conference of Irish Manufacturing Committee, Pp.248-254, Dublin, (1989)

[60] G. R. Symmons, M.S.J. Hashmi and Yd. Xie, "*The Optimisation of Plasto-Hydrodynamic Wire Drawing Process*", Proceeding of 6th International Conference on Modelling, Paris, France, Pp.362-266, (1987)

[61] G. R. Symmons, Yd. Xie, and M.S.J. Hashmi, "*Thermal Effect on Plasto-Hydrodynamic Wire Drawing Using a Polymer Melt*", Proceedings of 10th International Conference on Rheology, Vol.2, Pp.295-297, Sydney, Australia, (1988)

[62] Panwher, M.I, Crampton, R. and Hashmi, M.S.J, "*Analysis of The Die-Less Tube-Sinking Process Based on Non-Newtonian Characteristics of*

The Fluid Medium", Journal of Materials Processing Technology, Vol 21, No 2, P 155-175, (1990)

[63] G. R. Symmons, A.H. Memon and M. S. J. Hashmi, "*A Mathematical Model of a Plasto-Hydrodynamic Drawing of Narrow Strip*", Mathematical Computation Modeling, Vol.11, Pp.926-931, (1988)

[64] G. R. Symmons, A.H. Memon and M. S. J. Hashmi, "*A Newtonian Model of a Plasto-Hydrodynamic Drawing Process of a Rectangular Cross Sectional Continuum*", Proceeding of 7th International /Conference on Modelling Identification and Control, Grindlwald, Switzerland, Pp67-70, (1988)

[65] G. R. Symmons, A.H. Memon, R. Crampton and M. S. J. Hashmi, "*An Experimental Study of A Plasto-Hydrodynamic Strip Drawing Process of Rigid Non-Linearly Strain Hardening Strip Through A Stepped rectangular Slot*", Journal of Process Mechanical Engineering, Proceeding of International Mechanical Engineering, Part-E, Vol.203, Pp.57-65, (1989)

[66] G. R. Symmons, A.H. Memon, R. Crampton And M. S. J. Hashmi, " *A Numerical Solution for Plasto-Hydrodynamic Drawing of Girid Non-Linearly Strain Hardening Strips Through A Stepped Rectangular Slot*", Proceeding of 3rdfffdinternational Conference on Numerical Methods In Id. Forming Proces, Colorado, USA, pp.575-580, (1989)

[67] A.H. Memon, Ming, Zhang; M.S.J. Hashmi, and G.R. Symmons, "*Polymer Coating of Wire Using a Die-Less Drawing Process*" Journal Of Materials Processing Technology, Vol.26, N 2, P 173-180, (1991)

[68] Al-Natour and M.S.J. Hashmi, "*Development of a Complex Geometry Pressure Unit For Hydrodynamic Coating Applications*", Proceeding of 6th Conference of The Irish Manufacturing Committee, Dublin City University, Pp.280-297, (1989)

[69] Al-Natour, "*Plasto-Hydrodynamic Pressure due to the Flow of Viscous Fluid through A Confined Passage*", M.Eng Thesis, Dublin City University, (1989)

[70] M. A. Nwir, "*Plasto-Hydrodynamic Pressure In a Simple Tapered And Combined Geometry Unit For Drawing And Coating Wires*", PhD Thesis, Dublin City University, Dublin, Ireland, (1994)

[71] M. A. Nwir And M.S.J. Hashmi, "*Optimization of Pressure And Drawing Stress In A Simple Tapered Pressure Unit Using Borosiloxane As Pressure Fluid*", Proceeding of The 12th Conference of The Irish Manufacturing Committee, Pp.253-258, (1995)

[72] M. A. Nwir And M. S. J. Hashmi , "*Hydro-Dynamic Pressure Distribution In Tapered, Stepped Parallel Bore and Complex Geometry Pressure Units: Experimental Results*", Journal of Materials Processing Technology, Vol.77, pp.294-299, (1998)

[73] M.R. Stokes And G. R. Symmons, "*Performance Comparison of Polymer Fluids In Die-Less Wire Drawing*", Journal of Materials Processing Technology, V 43, N 1, P 13-20, (1994)

[74] M.R. Stokes And G. R. Symmons, "*Die-Less Wire Drawing Using Polymer Fluids*" Journal Of Synthetic Lubrication, V 12, N 3, , P 205-213, (1995)

[75] M.R. Stokes And G. R. Symmons, "*Numerical Optimisation of The Plasto-Hydrodynamic Drawing of Narrow Strips*", Journal of Materials Processing Technology, V 56, N 1-4, P 733-742, (1996)

[76] M.T Hillery And G.R. Symmons, "*Hydrodynamic Drawing of Wire At Elevated Temperatures*", Journal of Materials Processing Technology, V 56, N 1-4, P 302-312, (1996)

[77] S. Akter And M. S. J. Hashmi, "*High Speed Nylon Coating of Wire Using a Plasto-Hydrodynamic Pressure Unit*", Journal of Materials Processing Technology, V 63, N 1-3, P 453-457, (1997)

[78] S. Akter And M. S. J. Hashmi, "*Formation And Re-Melting of a Solid Polymer Layer on The Wire, In A Polymer Melt Chamber*", Journal of Materials Processing Technology, V 77, N 1-3, P 314-318, (1998)

[79] S. Akter And M. S. J. Hashmi, "*Modelling of The Pressure Distribution Within A Hydrodynamic Pressure Unit: Effect of The Change In Viscosity During Drawing Of Wire Coating*", Journal of Materials Processing Technology, V 77, N 1-3, P 32-36, (1998)

[80] S. Akter And M. S. J. Hashmi, "*Plasto-Hydrodynamic Pressure Distribution In An Exponentially Converging Coating Unit*", International Journal of Materials & Product Technology, V 13, N 3-6, P 384-399, (1998)

[81] S. Akter And M. S. J. Hashmi, "*Experimental Results of High Speed Wire Coating Using a Combined Hydrodynamic Unit*", Journal of Materials Processing Technology, V 92-93, P 224-229, (1999)

[82] S. Akter And M. S. J. Hashmi, "*Pressure Distribution Within a Stepped Parallel Bore Hydrodynamic Pressure Unit*", International Journal of Modeling And Simulation, V 20, N 1, P 20-26, (2000)

[83] S. A. Iqbal And M. S. J. Hashmi, "*High Pressure Viscosity Rheometry Based on Hydrodynamic Principle*", Proceeding of The International Conference on Advances In Materials And Processing Technologies (Ampt 98), Kuala Lampur, Malaysia, Vol.Ii. pp.338-348, (1998)

[84] S. A. Iqbal "*Development of A Novel Rheometeric Device for Determination of Pressure Dependent Viscosity of Non-Newtonian Fluids*", M.Eng Thesis. DCU, (2000)

[85] S. A. Iqbal And M.S.J. Hashmi, "*Determination of the Pressure Dependent Viscosity of Non-Newtonian Fluid Using A New Rheometrical Device*", Journal of Materials Processing Technology, [11] Volume 119, Pages 146-151, (2001)

[86] J. D. Lenk, "*Polymer Extrusion", Handbook of Controls and Instrumentation*" .Hanser Gardner Publications; 4th edition (2001)

[87] H. Dean Baker, "*Temperature Measurements in Engineering*". Vol. I and II, John Wiley & Sons Inc, (1961)

[88] http://www.natural-essential-oils.com/carrier_oil/glycerine.htm, "*Essential Oils for Natural Aromatherapy*". SEO-SEM Services.com, (2003)

[89] http://www.sy-kogyo.co.jp/english/sei/1_gly.html, (2003)

[90] http://www.fluorochemsilanes.co.uk/conventional%20siliconee%20fluids.htm, "*Conventional Silicone Fluids*", Fluorochem.net, (2003)

[91] A. M. Law and W. David Kelton, "*Simulation Modelling and Analysis*" Third Edition. Industrial. Engineering series, McGraw-HILL. (2000)

[92] http://www.fluent.com/solutions/brochures/fluent.pdf, "*Fluent flow modelling software*", Fluent. Inc., (2002).

[93] D. John and JR. Anderson, "*Computational fluid dynamics- The basics with applications*". Mechanical Engineering Series. McGraw-HILL, (1995)

[94] Hathaway, D. Michael and Wood, R. Jerry. "*Application of a multi-block CFD code to investigate the impact of geometry modeling on centrifugal compressor flow field predictions*", American Society of Mechanical Engineers (Paper), 96-GT-372, 12pp,(1996)

[95] Axon, Lee, Garry, Kevin, Howell and Jeff "*Evaluation of CFD for modelling the flow around stationary and rotating isolated wheels*", Developments in Vehicle Aerodynamics, Proceedings of the 1998 SAE International Congress & Exposition, Detroit, MI, USA, v-1318 ,p 65-75Feb 23-26 (1998)

[96] S.V. Makarytchev, D.F. Fletcher, and R.G.H. Prince, "*Progress in understanding the physical processes inside spinning cone columns*", Chemical Engineering Research and Design, v 81, n 1, p 122-130, (2003)

[97] http://www.fluentusers.com/fluent6.1/doc/ori/html/ug/node297.htm, *"Viscosity for Non-Newtonian Fluids"* , Fluent, support, services centre, Fluent Inc., (2003)

[98] http://www.fluentusers.com/fluent6.1/doc/ori/html/ug/node297.htm, *"Power law for non-Newtonian viscosity"* , Fluent, support, services centre, Fluent Inc., (2003)

[99] http://www.fluentusers.com/fluent6.1/doc/ori/html/ug/node361.htm, *"Overview of Moving zone Approaches"* , Fluent, support, services centre, Fluent Inc., (2003)

[100] http://www.fluentusers.com/fluent6.1/doc/ori/html/ug/node334.htm, *"Continuity and Momentum Equations"* , Fluent, support, services centre, Fluent Inc., (2003)

[101] misterguch.brinkster.net/bigdictionary.html, *"The Great Big Chemistry Dictionary"*, (2003)

[102] http://www.fluentusers.com/fluent6.1/doc/ori/html/ug/node364.htm, *"Equations for a Rotating References frame"* , Fluent, support, services centre, Fluent Inc., (2003)

[103] http://www.fluentusers.com/fluent6.1/doc/ori/html/ug/node310.htm, *"Overview of Numerical Schemes"* , Fluent, support, services centre, Fluent Inc., (2003)

[104] http://www.fluentusers.com/fluent6.1/doc/ori/html/ug/node811.htm, *"Segregated Solution Method"* , Fluent, support, services centre, Fluent Inc., (2003)

[105] http://www.fluentusers.com/fluent6.1/doc/ori/html/ug/node812.htm, *"Coupled Solution Method"* , Fluent, support, services centre, Fluent Inc., (2003)

[106] http://www.fluentusers.com/fluent6.1/doc/ori/html/ug/node179.htm, *"Pressure Inlet Boundary Conditions"* , Fluent, support, services centre, Fluent Inc., (2003)

[107] http://www.fluentusers.com/fluent6.1/doc/ori/html/ug/node182.htm, *"Calculation Procedure at Pressure Inlet Boundaries"* , Fluent, support, services centre, Fluent Inc., (2003)

[108] http://www.fluentusers.com/fluent6.1/doc/ori/html/ug/node195.htm, *"Pressure Outlet Boundary Conditions"* , Fluent, support, services centre, Fluent Inc., (2003)

[109] http://www.fluentusers.com/fluent6.1/doc/ori/html/ug/node198.htm, *"Calculation Procedure at Pressure Outlet Boundaries"* , Fluent, support, services centre, Fluent Inc., (2003)

[110] http://www.fluentusers.com/fluent6.1/doc/ori/html/ug/node212.htm, *"Wall Boundary Conditions"* , Fluent, support, services centre, Fluent Inc., (2003)

[111] http://www.fluentusers.com/fluent6.1/doc/ori/html/ug/node368.htm, *"Solution Strategies for a Rotating Reference Frame"* , Fluent, support, services centre, Fluent Inc., (2003)

[112] http://www.fluentusers.com/fluent6.1/doc/ori/html/ug/node347.htm, *"Modeling Axisymmetric Flows with Swirl or Rotation"* , Fluent, support, services centre, Fluent Inc., (2003)

[113] http://www.fluentusers.com/fluent6.1/doc/ori/html/ug/node369.htm, *"Post processing for a Single Rotating Reference Frame"* ., Fluent, support, services centre, Fluent Inc., (2003)

[114] A. Imhamed and M.S.J. Hashmi, "*Pressure Distribution within a New Shaped Plasto-Hydrodynamic Pressure Unit*" the 3rd International Conference on Advanced Manufacturing Technology, ACTM proceeding, Kuala Lumpur-Malaysia, 1070-1073, (May 2004)

[115] A. Imhamed and M. S. J. Hashmi, "*Plasto-hydrodynamic pressure distribution using Silicone-5 within a combined tapered and stepped gap geometry Pressure Unit*" the 14th international conference on Flexible Automation& intelligent Manufacturing, Toronto-Canada, 1018-1024, (July, 2004)

Appendix-A

Comparison between models Results

Comparison between the Results of Computational and Experimental Models for Glycerine

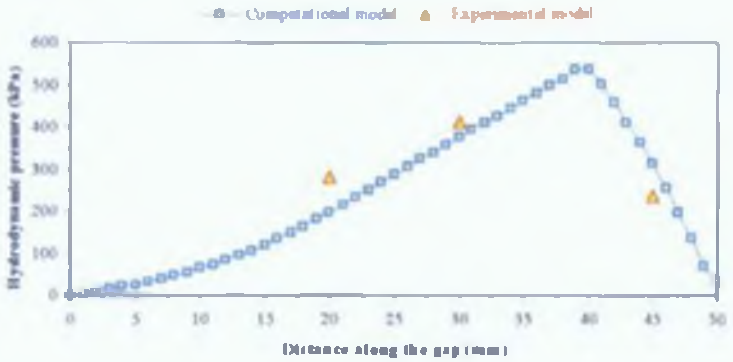

Figure A. 1: Pressure distribution profile for *Glycerine* within tapered gap ratio of *(0.9/0.3) at 0.5 m.sec*$^{-1}$ shaft speed

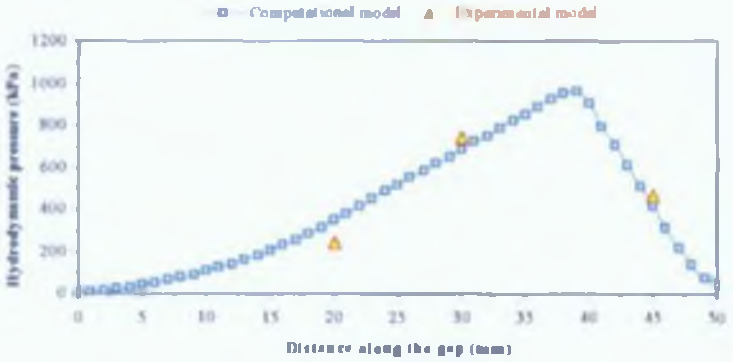

Figure A. 2: Pressure distribution profile for *Glycerine* within tapered gap ratio of *(0.9/0.3) at 1.0 m.sec*$^{-1}$ shaft speed

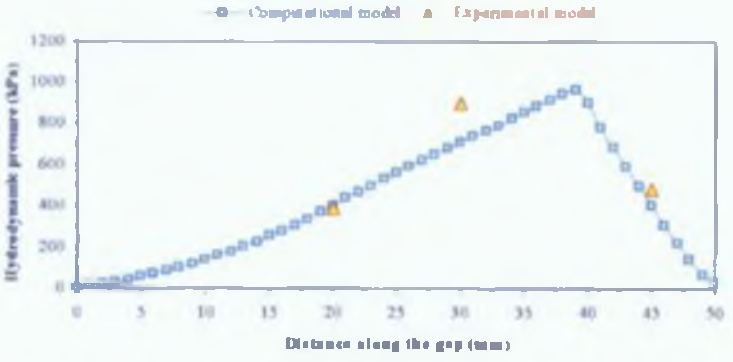

Figure A. 3: Pressure distribution profile for *Glycerine* within tapered gap ratio of *(0.9/0.3) at 1.5 m.sec*$^{-1}$ shaft speed

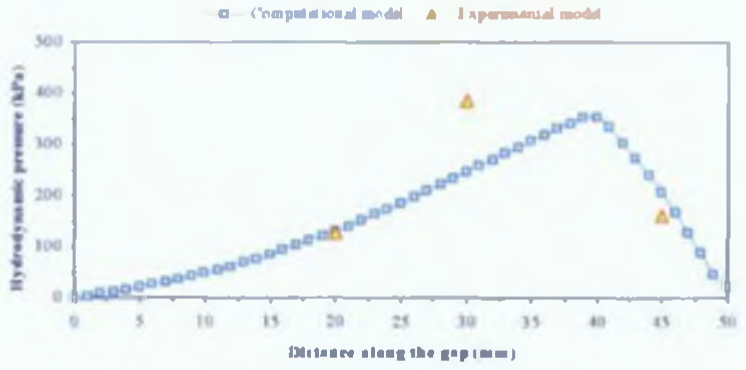

Figure A. 4: Pressure distribution profile for *Glycerine* within tapered gap ratio of *(1.0/0.5) at 0.5 m.sec*$^{-1}$ shaft speed

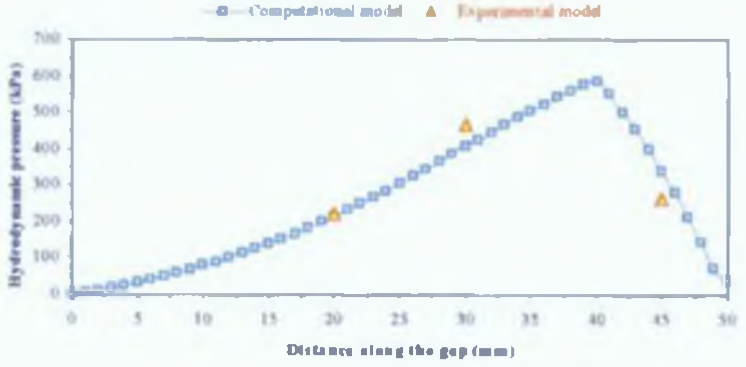

Figure A. 5: Pressure distribution profile for *Glycerine* within tapered gap ratio of *(1.0/0.5) at 1.0 m.sec*$^{-1}$ shaft speed

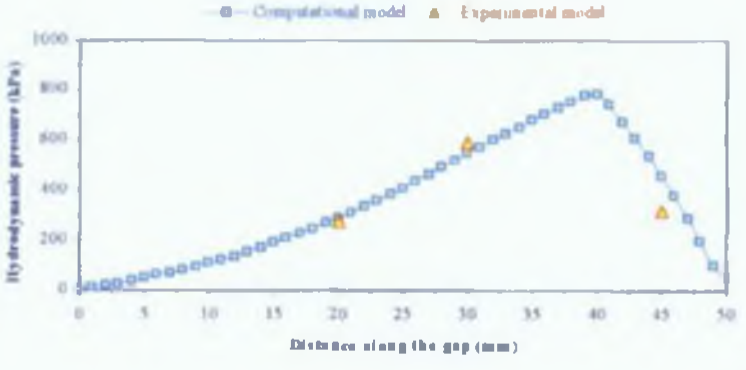

Figure A. 6: Pressure distribution profile for *Glycerine* within tapered gap ratio of *(1.0/0.5) at 1.5 m.sec*$^{-1}$ shaft speed

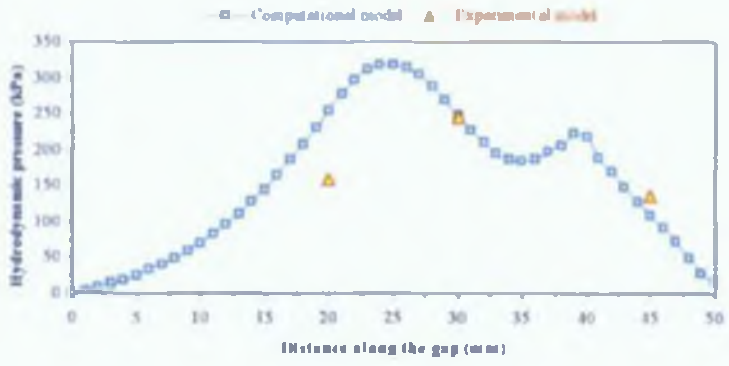

Figure A. 7: Pressure distribution profile for *Glycerine* within tapered gap ratio of *(1.2/0.3) at 0.5 m.sec*$^{-1}$ shaft speed

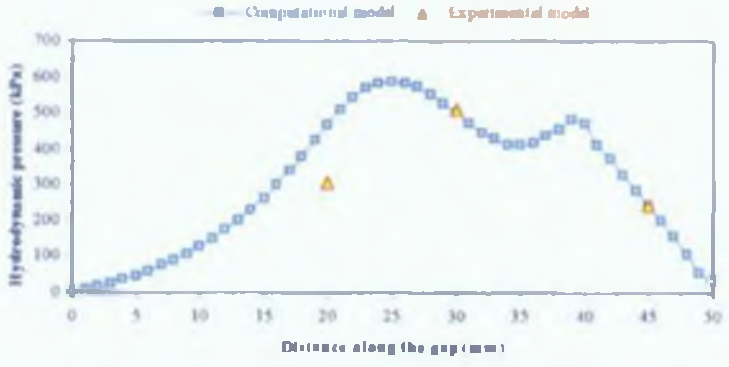

Figure A. 8: Pressure distribution profile for *Glycerine* within tapered gap ratio of *(1.2/0.3) at 1.0 m.sec*$^{-1}$ shaft speed

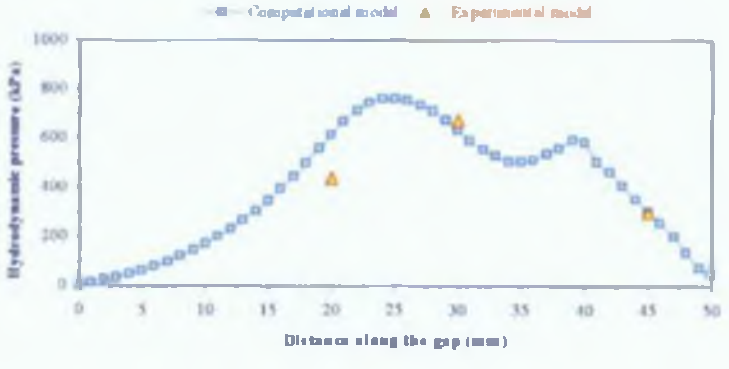

Figure A. 9: Pressure distribution profile for *Glycerine* within tapered gap ratio of *(1.2/0.3) at 1.5 m.sec*$^{-1}$ shaft speed

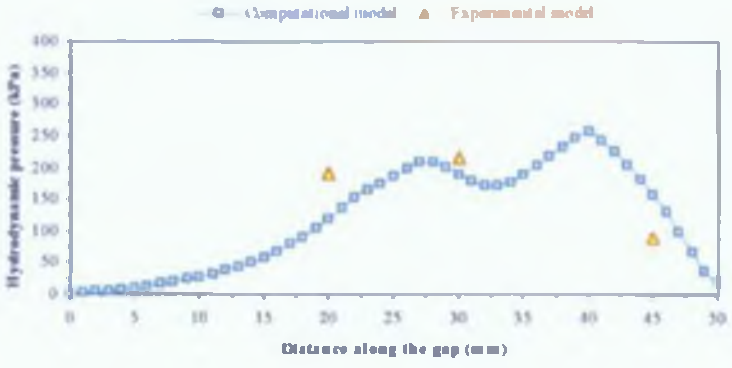

Figure A. 10: Pressure distribution profile for *Glycerine* within tapered gap ratio of *(1.5/0.3) at 0.5 m.sec*$^{-1}$ shaft speed

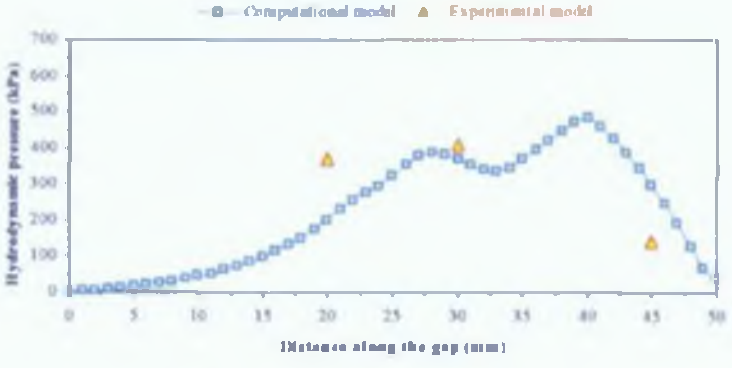

Figure A. 11: Pressure distribution profile for *Glycerine* within tapered gap ratio of *(1.5/0.3) at 1.0 m.sec*$^{-1}$ shaft speed

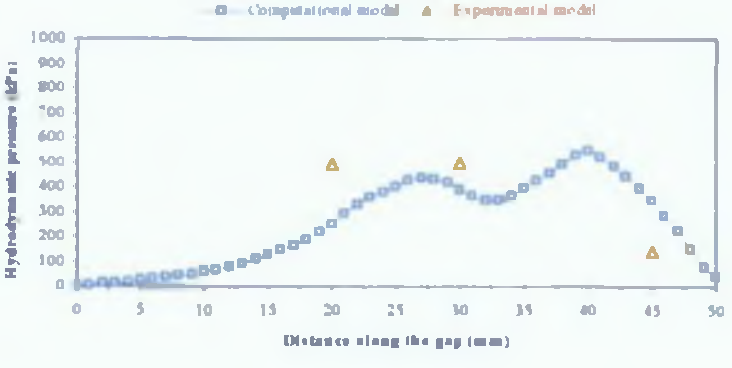

Figure A. 12: Pressure distribution profile for *Glycerine* within tapered gap ratio of *(1.5/0.3) at 1.5 m.sec*$^{-1}$ shaft speed

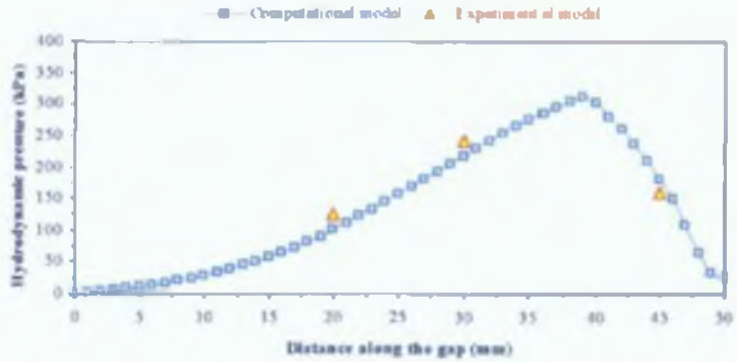

Figure A. 13: Pressure distribution profile for *Glycerine* within tapered gap ratio of *(1.5/0.5) at 0.5 m.sec*$^{-1}$ shaft speed

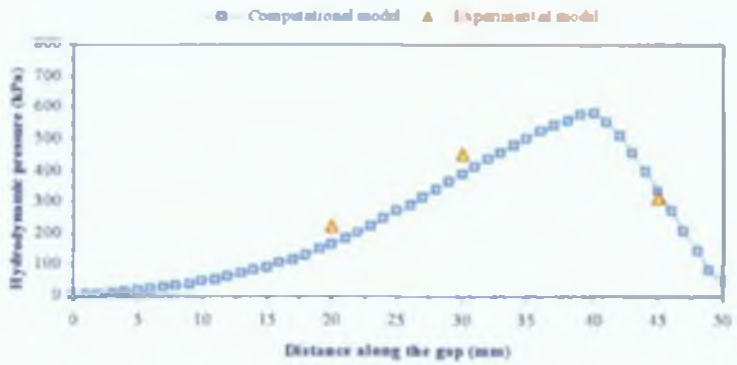

Figure A. 14: Pressure distribution profile for *Glycerine* within tapered gap ratio of *(1.5/0.5) at 1.0 m.sec*$^{-1}$ shaft speed

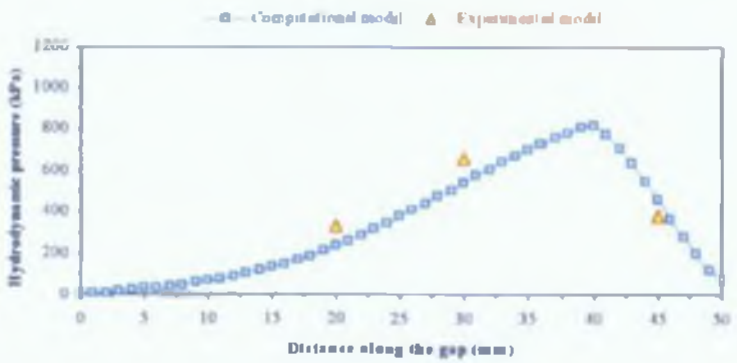

Figure A. 15: Pressure distribution profile for *Glycerine* within tapered gap ratio of *(1.5/0.5) at 1.5 m.sec*$^{-1}$ shaft speed

Comparison between the Results of Computational and Experimental Models for Silicone-5

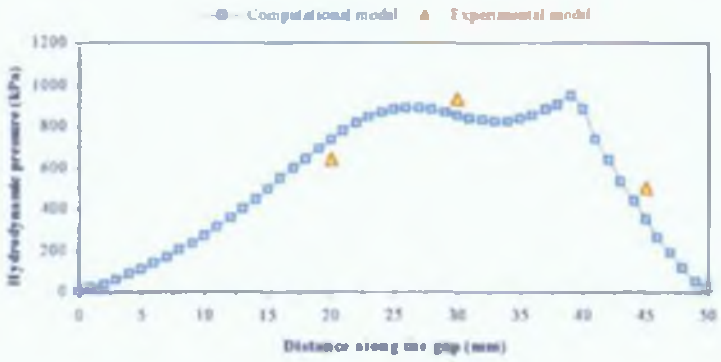

Figure A. 16: Pressure distribution profile for *Silicone-5* within tapered gap ratio of *(0.9/0.3) at 0.5 m.sec*$^{-1}$ shaft speed

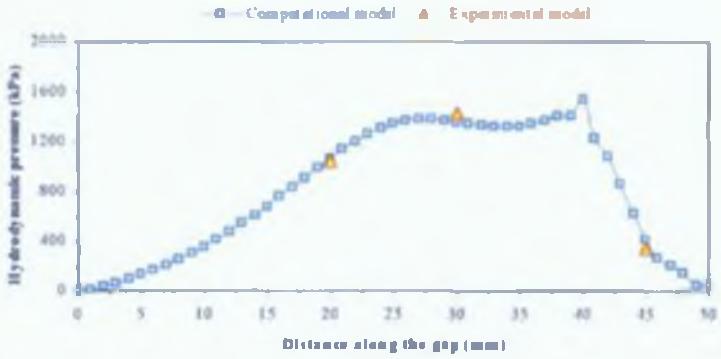

Figure A. 17: Pressure distribution profile for *Silicone-5* within tapered gap ratio of *(0.9/0.3) at 1.0 m.sec*$^{-1}$ shaft speed

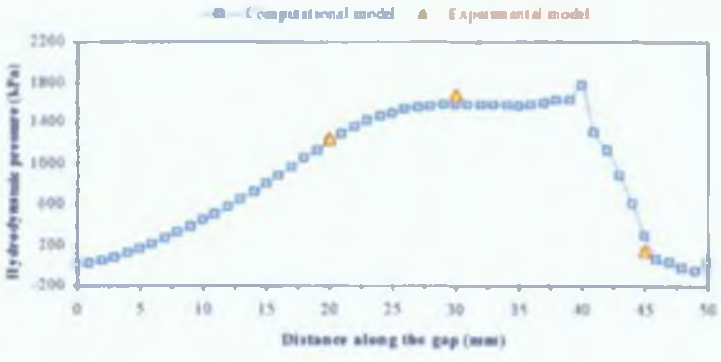

Figure A. 18: Pressure distribution profile for *Silicone-5* within tapered gap ratio of *(0.9/0.3) at 1.5 m.sec*$^{-1}$ shaft speed

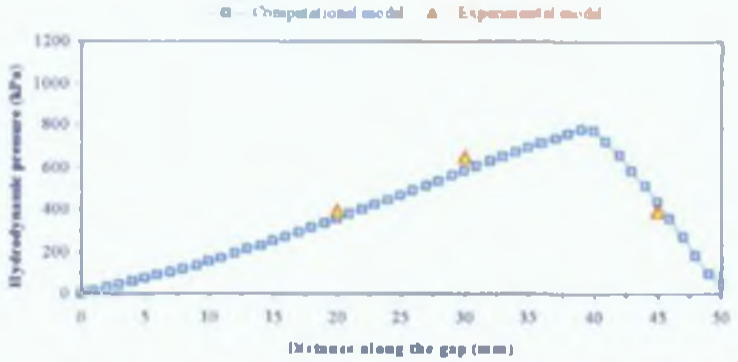

Figure A. 19: Pressure distribution profile for *Silicone-5* within tapered gap ratio of *(1.0/0.5) at 0.5 m.sec*$^{-1}$ shaft speed

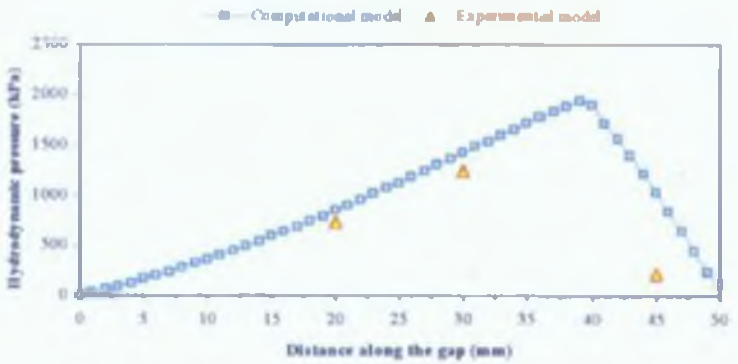

Figure A. 20: Pressure distribution profile for *Silicone-5* within tapered gap ratio of *(1.0/0.5) at 1.0 m.sec*$^{-1}$ shaft speed

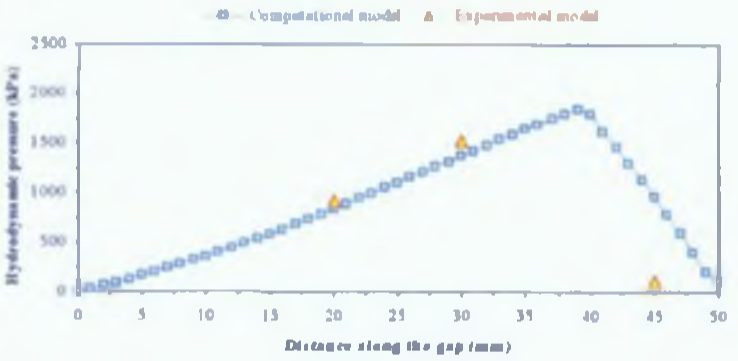

Figure A. 21: Pressure distribution profile for *Silicone-5* within tapered gap ratio of *(1.0/0.5) at 1.5 m.sec*$^{-1}$ shaft speed

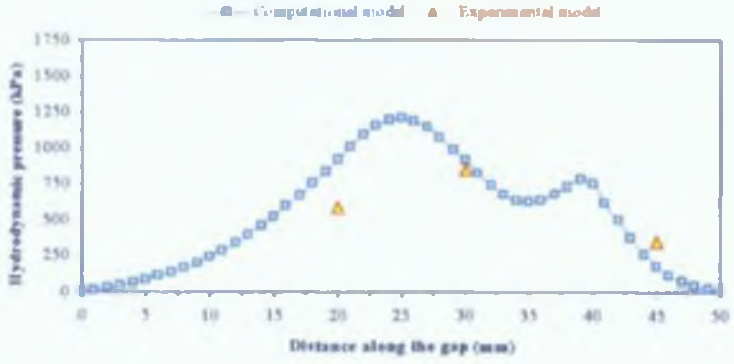

Figure A. 22: Pressure distribution profile for *Silicone-5* within tapered gap ratio of *(1.2/0.3) at 0.5 m.sec*$^{-1}$ shaft speed

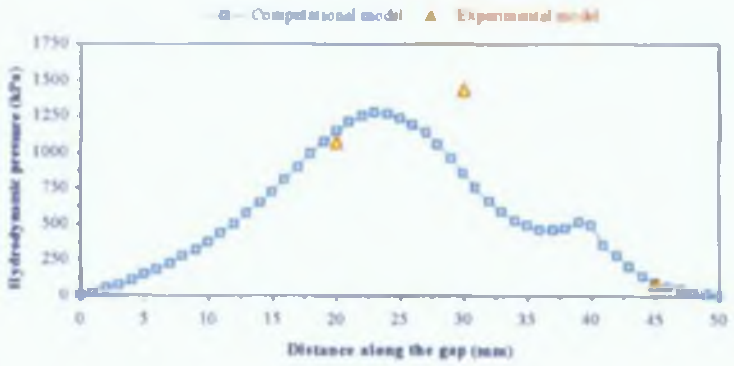

Figure A. 23: Pressure distribution profile for *Silicone-5* within tapered gap ratio of *(1.2/0.3) at 1.0 m.sec*$^{-1}$ shaft speed

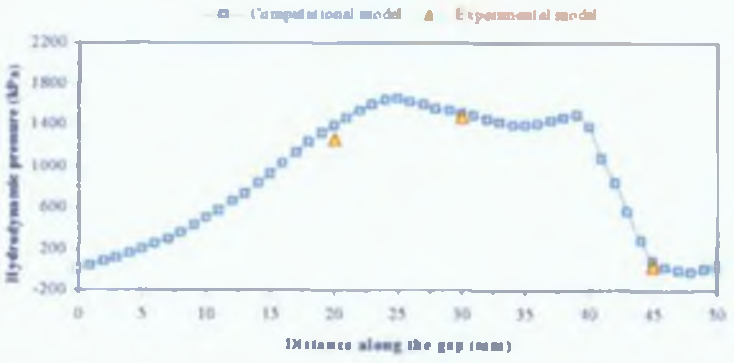

Figure A. 24: Pressure distribution profile for *Silicone-5* within tapered gap ratio of *(1.2/0.3) at 1.5 m.sec*$^{-1}$ shaft speed

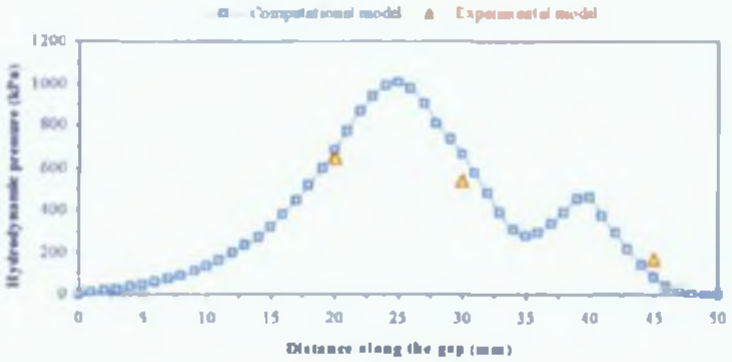

Figure A. 25: Pressure distribution profile for *Silicone-5* within tapered gap ratio of *(1.5/0.3) at 0.5 m.sec*$^{-1}$ shaft speed

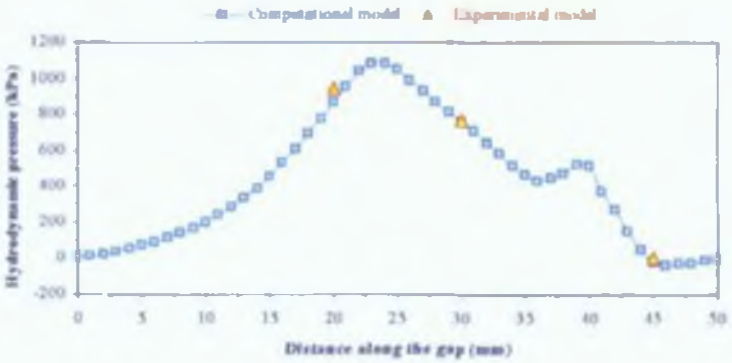

Figure A. 26: Pressure distribution profile for *Silicone-5* within tapered gap ratio of *(1.5/0.3) at 1.0 m.sec*$^{-1}$ shaft speed

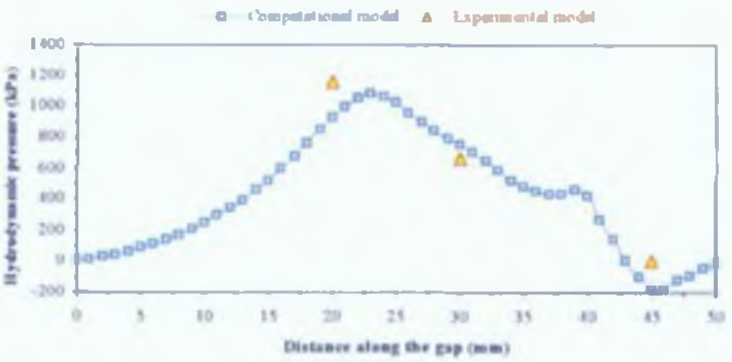

Figure A. 27: Pressure distribution profile for *Silicone-5* within tapered gap ratio of *(1.5/0.3) at 1.5 m.sec*$^{-1}$ shaft speed

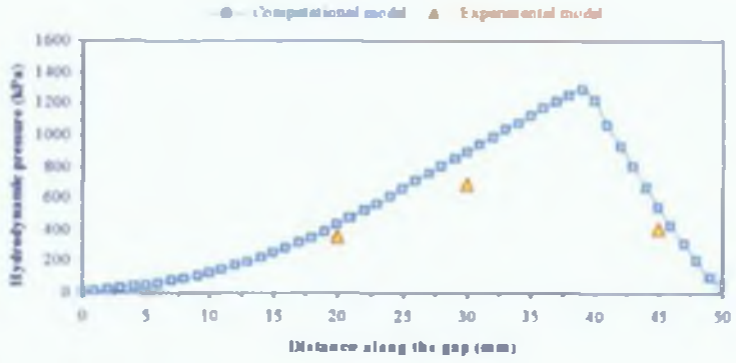

Figure A. 28: Pressure distribution profile for *Silicone-5* within tapered gap ratio of *(1.5/0.5) at 0.5 m.sec*$^{-1}$ shaft speed

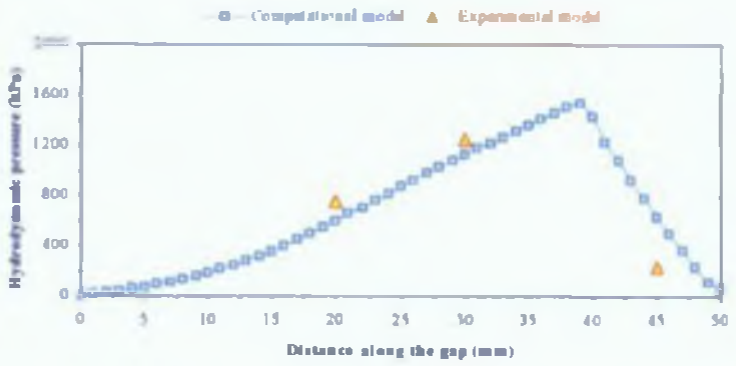

Figure A. 29: Pressure distribution profile for *Silicone-5* within tapered gap ratio of *(1.5/0.5) at 1.0 m.sec*$^{-1}$ shaft speed

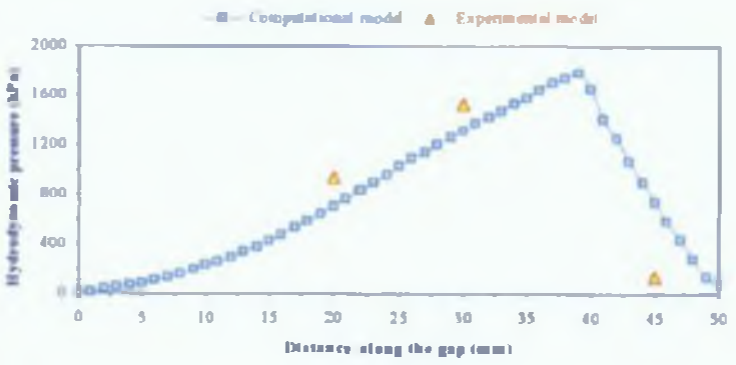

Figure A. 30: Pressure distribution profile for *Silicone-5* within tapered gap ratio of *(1.5/0.5) at 1.5 m.sec*$^{-1}$ shaft speed

Comparison between the Results of Computational and Experimental Models for Silicone-12.5

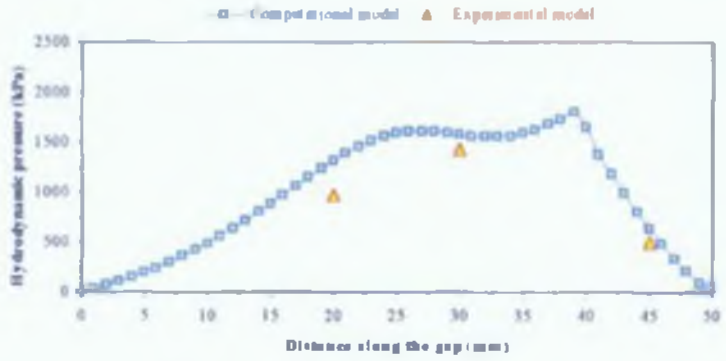

Figure A. 31: Pressure distribution profile for *Silicone-12.5* within tapered gap ratio of *(0.9/0.3) at 0.5 m.sec^{-1}* shaft speed

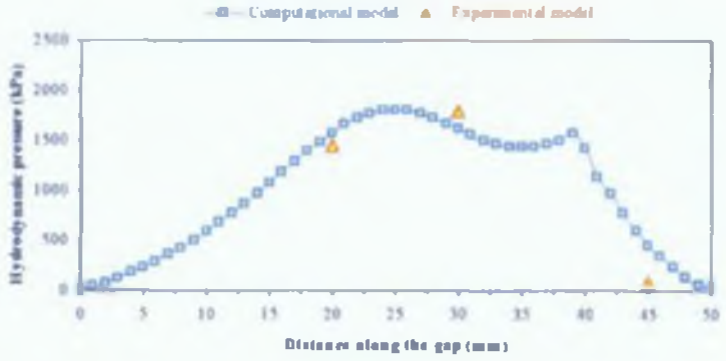

Figure A. 32: Pressure distribution profile for *Silicone-12.5* within tapered gap ratio of *(0.9/0.3) at 1.0 m.sec^{-1}* shaft speed

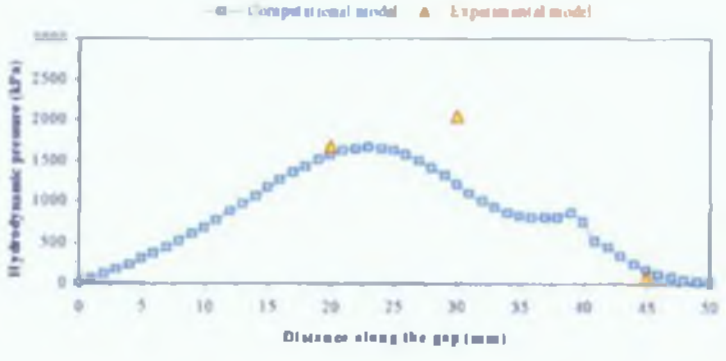

Figure A. 33: Pressure distribution profile for *Silicone-12.5* within tapered gap ratio of *(0.9/0.3) at 1.5 m.sec^{-1}* shaft speed

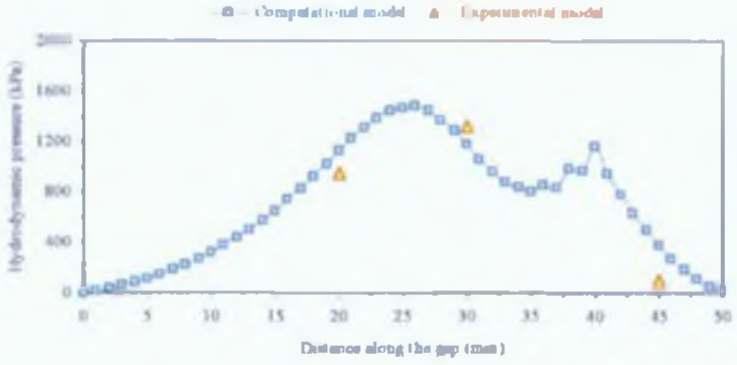

Figure A. 34: Pressure distribution profile for *Silicone-12.5* within tapered gap ratio of *(1.2/0.3) at 0.5 $m.sec^{-1}$* shaft speed

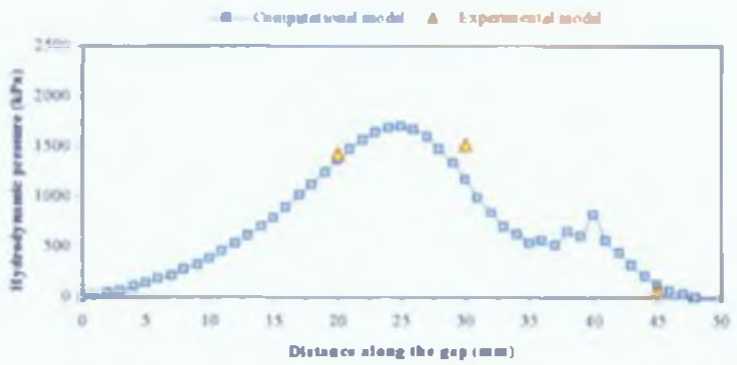

Figure A. 35: Pressure distribution profile for *Silicone-12.5* within tapered gap ratio of *(1.2/0.3) at 1.0 $m.sec^{-1}$* shaft speed

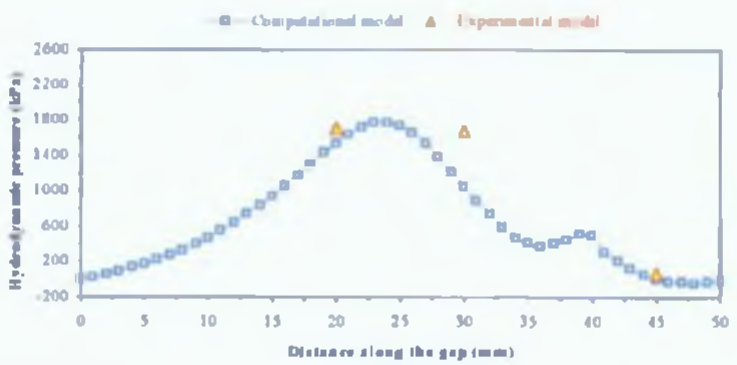

Figure A. 36: Pressure distribution profile for *Silicone-12.5* within tapered gap ratio of *(1.2/0.3) at 1.5m.sec^{-1}* shaft speed

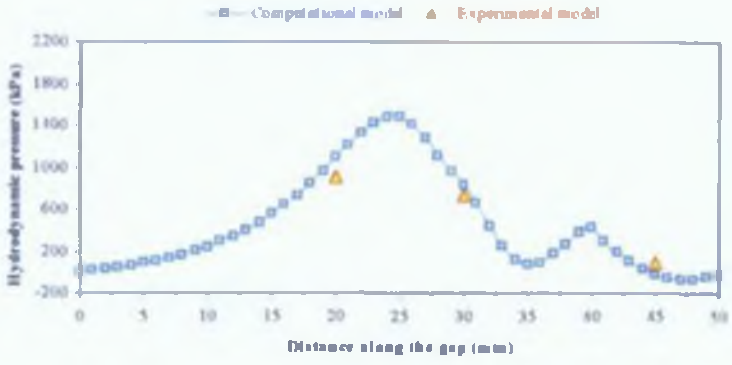

Figure A. 37: Pressure distribution profile for *Silicone-12.5* within tapered gap ratio of *(1.5/0.3) at 0.5m.sec^{-1}* shaft speed

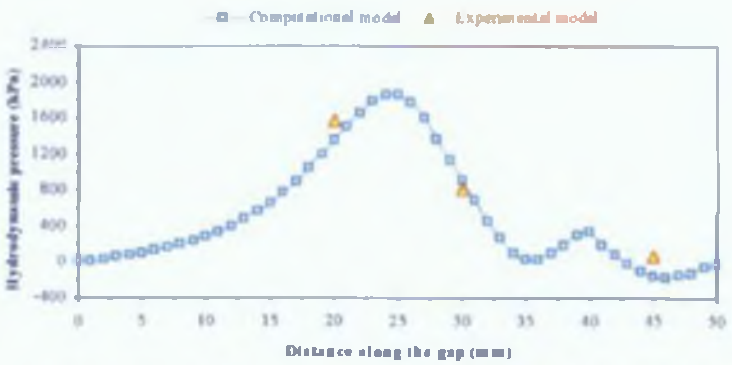

Figure A. 38: Pressure distribution profile for *Silicone-12.5* within tapered gap ratio of *(1.5/0.3) at 1.0 m.sec^{-1}* shaft speed

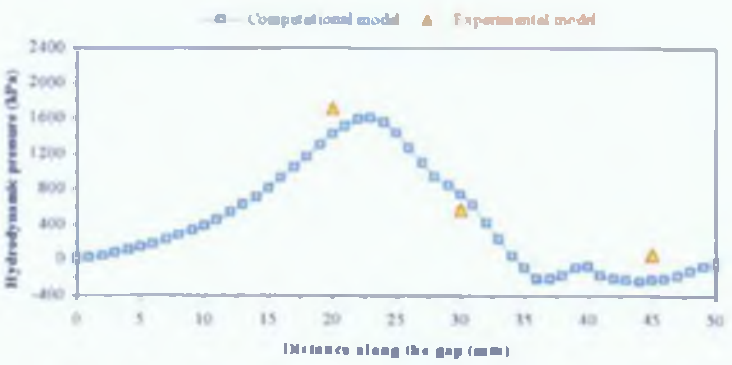

Figure A. 39: Pressure distribution profile for *Silicone-12.5* within tapered gap ratio of *(1.5/0.3) at 1.5 m.sec^{-1}* shaft speed

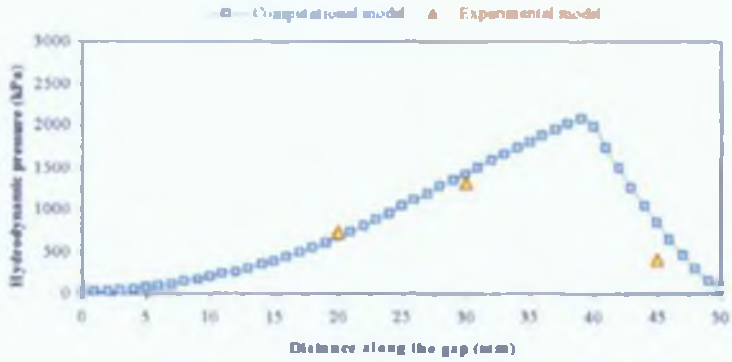

Figure A. 40: Pressure distribution profile for *Silicone-12.5* within tapered gap ratio of *(1.5/0.5) at 0.5 m.sec*$^{-1}$ shaft speed

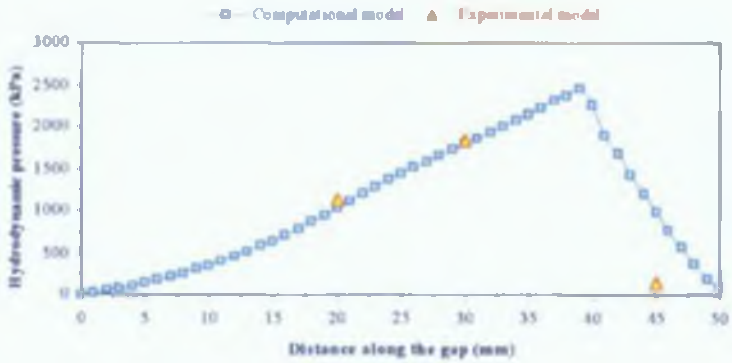

Figure A. 41: Pressure distribution profile for *Silicone-12.5* within tapered gap ratio of *(1.5/0.5) at 1.0 m.sec*$^{-1}$ shaft speed

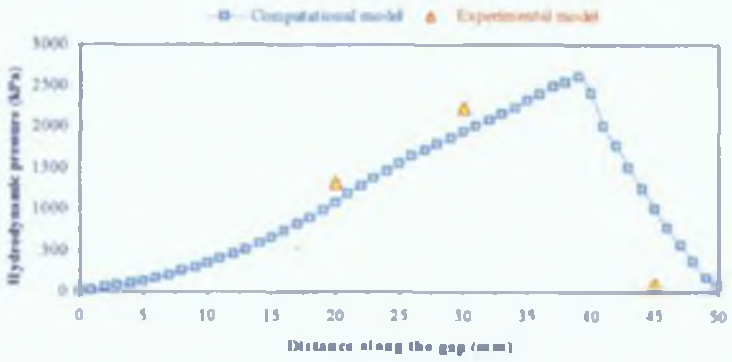

Figure A. 42: Pressure distribution profile for *Silicone-12.5* within tapered gap ratio of *(1.5/0.5) at 1.5 m.sec*$^{-1}$ shaft speed

Comparison between the Computational pressure profiles at various shaft speeds

Glycerine pressure profiles:

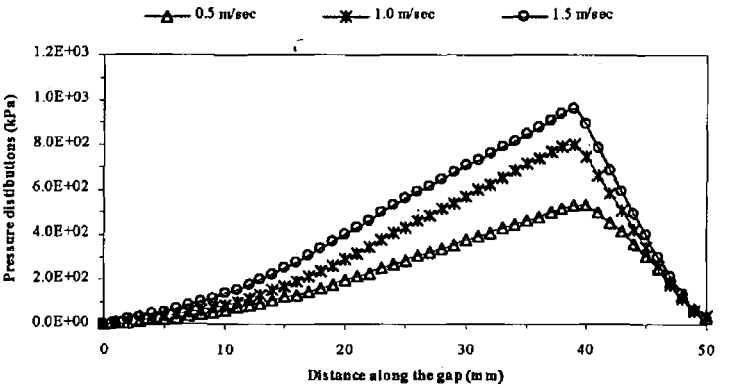

Figure A. 43: Pressure distribution profiles for *Glycerine* within *(0.9/0.3) gap ratio* at various shaft speeds

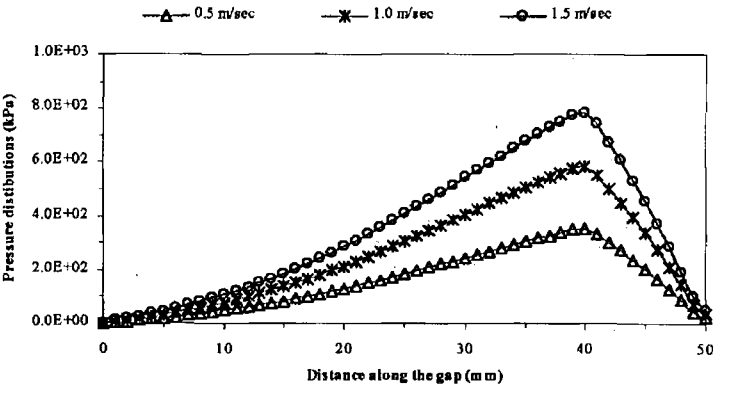

Figure A. 44: Pressure distribution profiles for *Glycerine* within *(1.0/0.5) gap ratio* at various shaft speeds

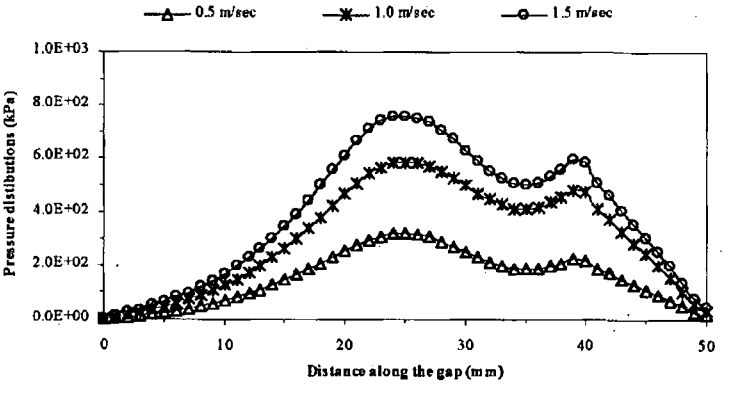

Figure A. 45: Pressure distribution profiles for *Glycerine* within *(1.2/0.3) gap ratio* at various shaft speeds

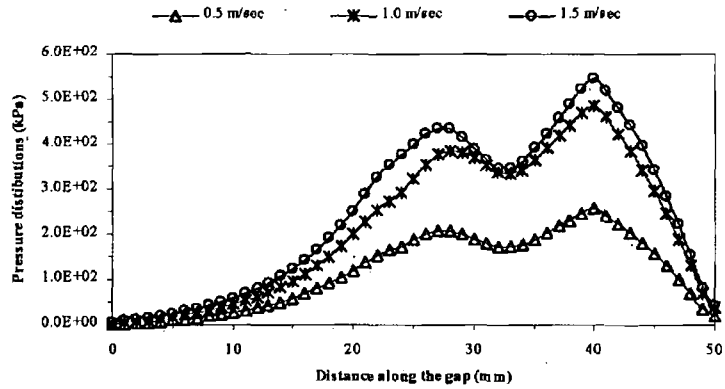

Figure A. 46: Pressure distribution profiles for *Glycerine* within *(1.5/0.3) gap ratio* at various shaft speeds

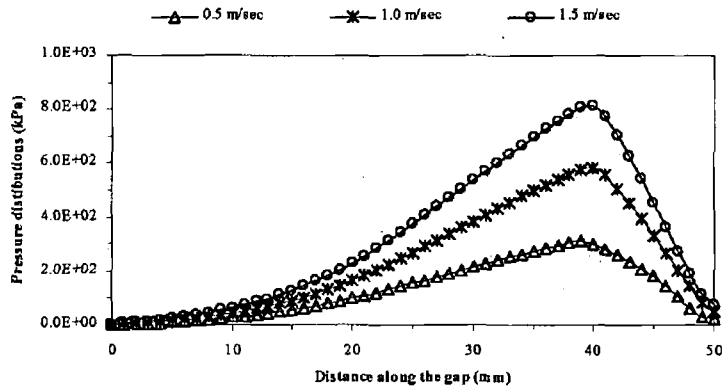

Figure A. 47: Pressure distribution profiles for *Glycerine* within *(1.5/0.5) gap ratio* at various shaft speeds

Silicone-5 pressure profiles:

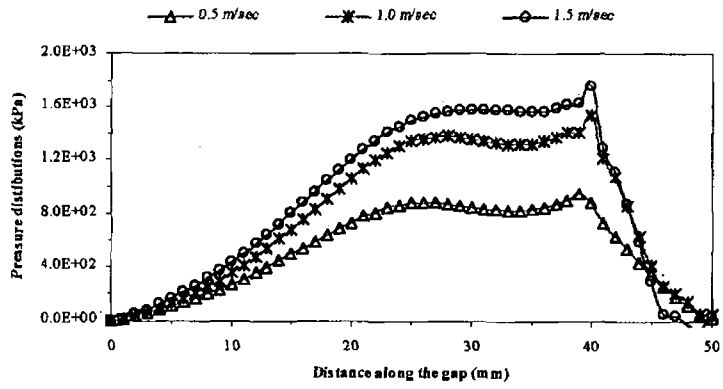

Figure A. 48: Pressure distribution profiles for *Silicone-5* within *(0.9/0.3) gap ratio* at various shaft speeds

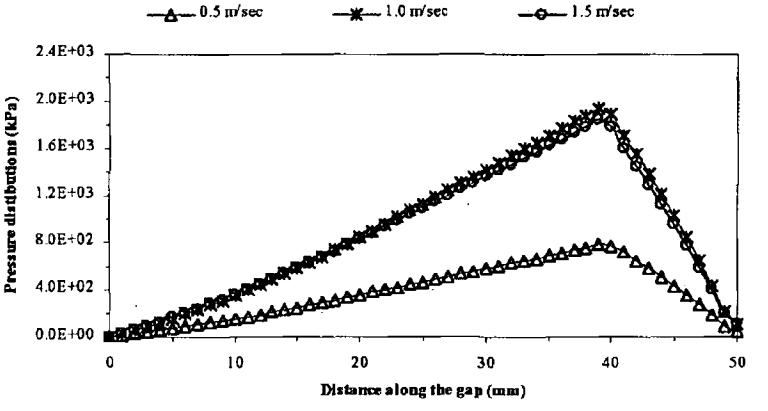

Figure A. 49: Pressure distribution profiles for *Silicone-5* within *(1.0/0.5) gap ratio* at various shaft speeds

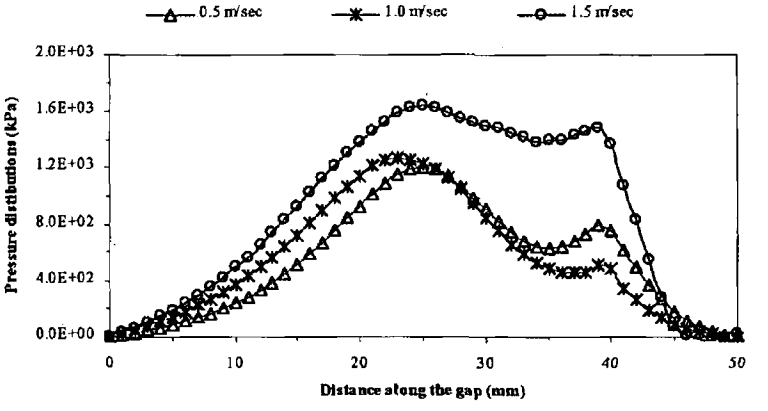

Figure A. 50: Pressure distribution profiles for *Silicone-5* within *(1.2/0.3) gap ratio* at various shaft speeds

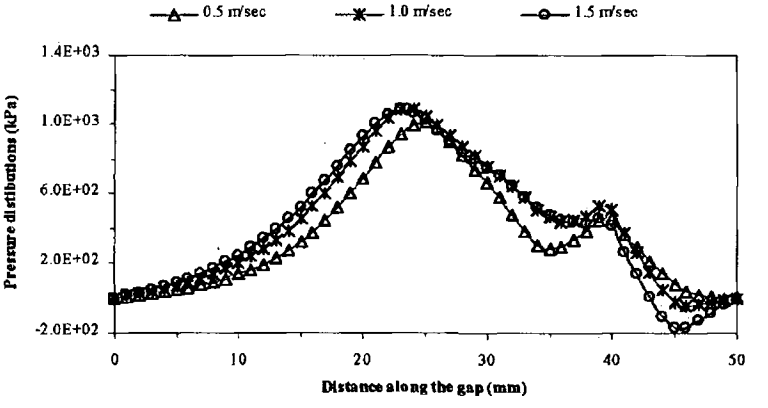

Figure A. 51: Pressure distribution profiles for *Silicone-5* within *(1.5/0.3) gap ratio* at various shaft speeds

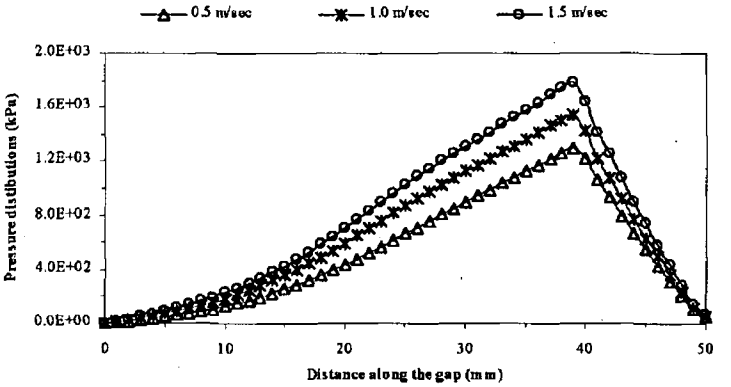

Figure A. 52: Pressure distribution profiles for *Silicone-5* within *(1.5/0.5) gap ratio* at various shaft speeds

Silicone-5 pressure profiles:

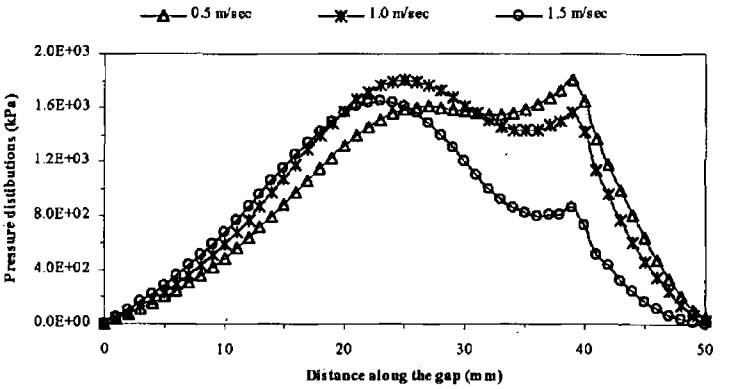

Figure A. 53: Pressure distribution profiles for *Silicone-12.5* within *(0.9/0.3) gap ratio* at various shaft speeds

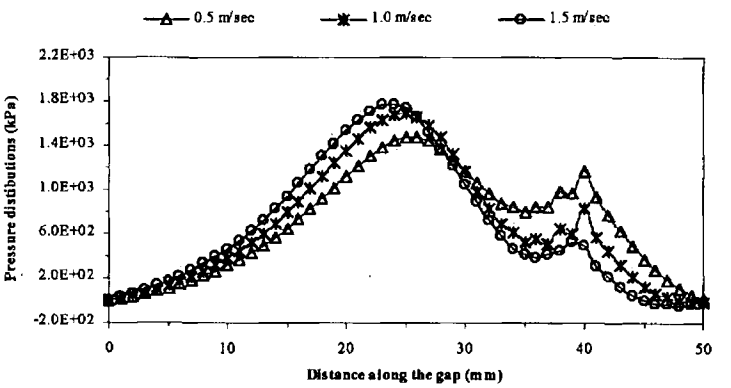

Figure A. 54: Pressure distribution profiles for *Silicone-12.5* within *(1.2/0.3) gap ratio* at various shaft speeds

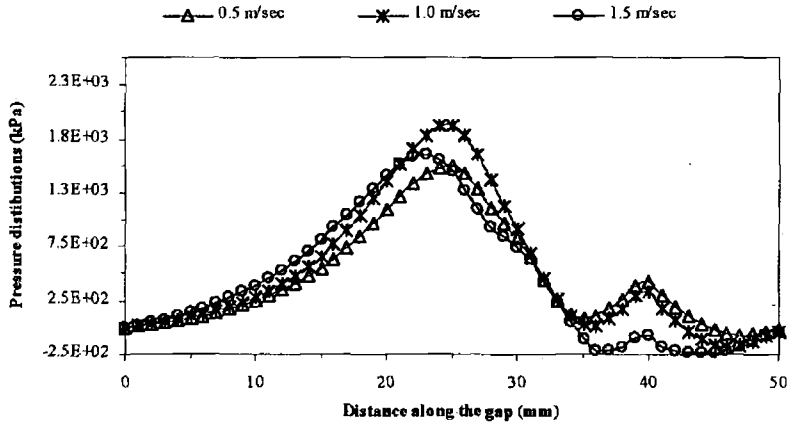

Figure A. 55: Pressure distribution profiles for *Silicone-12.5* within *(1.5/0.3) gap ratio* at various shaft speeds

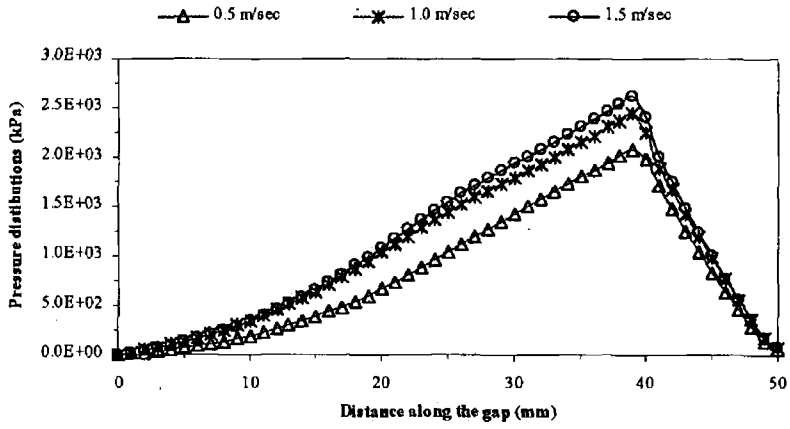

Figure A. 56: Pressure distribution profiles for *Silicone-12.5* within *(1.5/0.3) gap ratio* at various shaft speeds

Appendix-B

Publications

- A. Imhamed and M.S.J. Hashmi, "Pressure Distribution within a New Shaped Plasto-Hydrodynamic Pressure Unit" *the 3rd International Conference on Advanced Manufacturing Technology, ACTM proceeding*, Kuala Lumpur-Malaysia, 1070-1073, (May 2004)

- A. Imhamed and M. S. J. Hashmi, "Plasto-hydrodynamic pressure distribution using Silicone-5 within a combined tapered and stepped gap geometry Pressure Unit" *the 14th international conference on Flexible Automation& intelligent Manufacturing*, Toronto-Canada, 1018-1024, (July, 2004)